Development of a cost-effective terrain-adaptive prosthetic ankle

C Le Roux

orcid.org/ 0000-0002-0068-1390

Dissertation accepted in fulfilment of the requirements for the degree *Master of Engineering in Electrical and Electronic Engineering* at the North-West University

Supervisor: Prof AJ Grobler

Co-supervisor: Dr A Sheri

Graduation: June 2025

Acknowledgements

Ms I. Truter, Prof A.J. Grobler, Prof A. Sheri, Mr I.J. Thomson, Mr J.P. van Deventer and Mr J.S. Malan

Abstract

Prosthetic ankles with the capacity of adapting to terrain and walking speed are found commercially, but are too expensive for the majority of South Africans to afford. This dissertation covers the development of a terrain-adaptive prosthetic ankle to improve accessibility to users and promote user safety. To achieve this, commercially available mechanical components were used to create a DC motor actuated linkage mechanism that interacts with the terrain using carbon foot blades, allowing for real-time terrain adaptation. Additional focus was placed on increasing the minimum toe clearance and stance phase stability to reduce the risk of falling and thereby prioritising user safety.

The system was tested on a test bench that was designed to emulate human walking biomechanics. It was found that the toe clearance was improved at the beginning of the swing phase by 6 mm, which corresponds to a more natural knee motion when compared to a commercial ESAR prosthetic foot at a level incline and 0.5 m/s walking speed. This demonstrates the system's potential for improving user mobility and safety in comparison to ESAR prosthetic feet. The system achieved significant cost reductions by utilising commercially available mechanical components, while maintaining comparable performance to state-of-the-art systems. Future work will focus on testing the prosthetic ankle on a real amputee, evaluating the durability and terrain-adaptiveness of the system in different environments.

Keywords: low-cost; prosthetic; robotics; terrain-adaptive

Contents

List of Figures

List of Tables

Table of abbreviations

IMU	Inertial measurement unit
ESAR	Energy Storage and Return
ROM	Range of Motion
MTC	Minimum toe clearance
EMG	Electromyography
MEMS	Micro Electro-Mechanical Sensors
BLDC	Brushless Direct-Current Motor
PCA	Principal component analysis
LDA	Linear discriminant analysis
PID	Proportional, integral, and derivative term controller
DC	Direct current
LLA	Lower limb amputation

Chapter 1

Introduction

1.1 Background

Prosthetic feet allow amputees to regain their lost mobility to a large extent, as prosthetic feet and ankles allow lower limb amputees to interface with the terrain effectively. Scientific advancements made in the field of prosthetics allow prosthetic ankles to output a net positive output power propelling the amputee forward, as will be further discussed in Section 2.4. Other prosthetic ankles that are commercially available allow for terrain adaptability, where the ankle parameters are changed when the user is traversing different terrains.

However, these commercial prosthetic ankles are rather expensive in comparison to the South African median income. The median monthly income in South Africa is R5 417 ($298.13) as of 2022 [1], meaning that a prosthetic designed for use in South Africa should be a low-cost solution to enable accessibility to life changing technology. For instance, the Propriofoot from Össur is around $34 000 (R617 780), using an exchange rate of R18.17 per USD throughout the paper. Therefore, it can be seen that such a prosthetic foot may be far outside the reach of the average South African.

terrain-adaptive ankles allow the amputee higher mobility on different surfaces and when encountering different obstacles. Examples of these obstacles include inclined surfaces, curbs and stairs, as these are the most commonly encountered obstacles that can be expected by an amputee in an urban environment. As will be further discussed in Section 2.3, there are two important factors during the gait cycle that should be considered when traversing any obstacle, namely stability during the stance phase and toe clearance during the swing phase. If the prosthetic allows for good stance phase stability during the stance phase and provides sufficient toe clearance during the swing phase the amputee should be safe while traversing the obstacle, barring mechanical failure of the other mechanical components that make up a prosthetic leg.

Although amputees are capable of ambulation with energy storage and return (ESAR) prosthetic feet, as will be discussed in detail in Section 2.3, there exist some risks of falling using these prostheses. Therefore, the prosthetic ankle that will be designed in this paper will also focus on minimising the risks involved with using prosthesis from the user's perspective.

There are approximately 30 million people worldwide living with limb loss [2], where causes of amputation can vary widely. In the UK, amputees are typically older, with the most common causes of amputations being arterial disease or complications from diabetes [2]. The second most common cause of lower limb amputation is mechanical trauma, which is also the leading cause of upper limb amputation [2]. In South Africa, however, 2400 lower limb amputations were performed in 2016, in KwaZulu-Natal [3], this was explained by the high number of road accidents in the area. In addition to the high number of lower limb amputations happening in South Africa due to road accidents, amputees living in rural areas waited around one year for their prosthesis to be fitted [3].

1.1.1 Amputee mobility level and prosthetic requirements

Amputees undergo amputation for different reasons, and individual differences in the human population means that not all amputees are at the same fitness level when it comes to rehabilitation. Therefore, different prostheses are made to fit the various activity levels that amputees may require. These mobility levels are commonly referred to as K-levels, and the definitions by Balk et al. are laid out in Table 1.1 below [4].

Table 1.1: K mobility level definitions

K Level	Description
K1 : Indoor Walker	Assisted by the prosthetic, the amputee is capable of walking at a fixed cadence on level surfaces
K2 : Restricted outdoor walker	Amputee can walk limited distances at slow walking speeds, as well as navigate limited obstacles
K3 : Unrestricted outdoor walker	Amputee can traverse most environmental obstacles and are able to walk at varying speeds
K4 : Outdoor walker with high requirements	Amputee can move without restrictions, capable of fulfilling the needs of a child or active adult.

These mobility level definitions largely depend on the physical capabilities of the amputee and help them select the right prosthetic from a catalogue based on their needs. Indoor walkers that do not need a prosthesis for long range ambulation will for example use a K1 rated prosthesis, as a higher rated prosthesis would be unnecessary.

A prosthetic ankle that would be capable of adapting to terrain and walking speed would be a K3 or K4 prosthetic, as this prosthetic would support the user's active lifestyle. Therefore, the requirements of the prosthetic to limit the risks of falling would also be important, as these individuals would also encounter more risky situations in comparison to others who would not encounter as many obstacles.

terrain-adaptiveness is important, as amputees may develop overuse injuries from compensatory movements due to muscle loss in the amputated limb [5], [6]. This means that a prosthetic device limiting the compensatory mechanisms implemented by amputees will be preferable, as this may help reduce long term overuse injury and reduce the risk of falling. Section 2.3 will cover the falling risks as well as the compensatory mechanisms employed by amputees in more detail.

1.1.2 Benefits of terrain-adaptive ankles

As an amputee loses mobility due to the loss of muscles in the amputated leg, the amputee loses some of the muscles the amputee would normally use to modify his or her kinematic gait pattern as a function of the activity being performed [7]. Therefore, to assist the amputees in performing activities other than walking on a level surface, a terrain-adaptive prosthetic is needed. Without an adaptive prosthetic, the amputee would make use of compensatory movements to allow the amputee to traverse the terrain.

A simple scenario will be described to give the reader context of a situation where a terrain-adaptive prosthetic ankle would assist the amputee, the effect of toe clearance and stability are discussed in detail in Section 2.3. In the case of ascending an inclined surface, the amputee must create a toe path with the prosthetic foot, such that the prosthetic foot can be placed in front of the amputee in order to take the next step. Figure 1.1 displays a representation of an amputee traversing a ramp.

When traversing an obstacle such as a ramp with a prosthetic as displayed in Figure 1.1, two important factors come into play. First, the toe path of the prosthetic, which may impede the toe clearance if the prosthetic has a fixed ankle and does not move like a natural ankle. This causes amputees to use compensatory movements, such as lifting in the hip, to achieve the required clearance [6]. In the case where the amputee is unable to achieve toe clearance on an obstacle, the amputee may fall due to the centre of mass being outside the base of support, which is commonly classified as tripping [8]. Therefore, if the prosthetic ankle does not actively create toe clearance, the toe clearance must be created with compensatory movements from the amputee.

Secondly, specifically for inclined surfaces, the prosthetic must support the user's weight during the stance phase (see Section 2.2). If the prosthetic is unable to conform to the inclined surface as a natural ankle would, the friction between the surface and the pros-

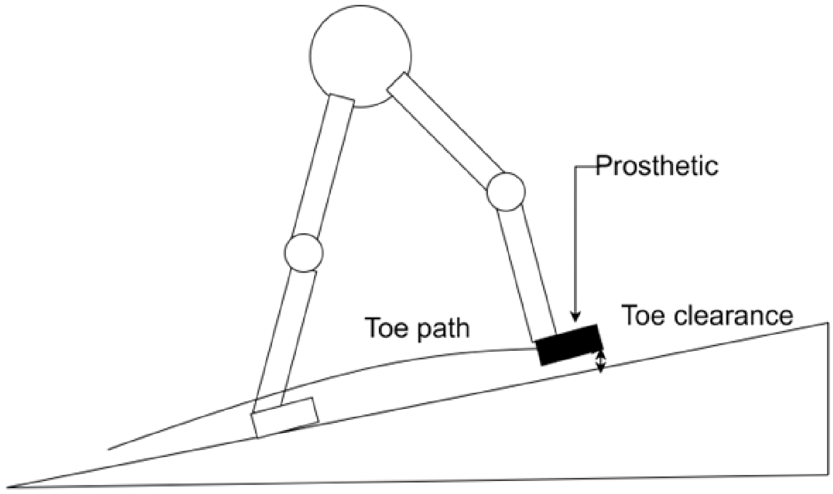

Figure 1.1: Toe path and toe clearance on a ramp

thetic is decreased. This is because the contact surface will be less if less of the prosthetic is in contact with the surface. This can also contribute to increasing the risk of slipping and falling (see Section 2.3).

Therefore, to minimise the risk of falling of the amputee over obstacles such as ramps and stairs, terrain-adaptive ankles are needed to ensure a safer user experience. This subsection was a brief discussion of why terrain-adaptive prosthesis are advantageous, however this discussion will be revisited in depth in Section 2.3.

1.2 Problem Statement

The median income in South Africa is vastly below the price of a life changing prosthetic device. Since the majority of lower limb amputations (LLA) in South Africa result from mechanical trauma [3], many of the amputees have the potential to gain mobility, if they were able to acquire such a device. This is because the amputee may still be in relative health despite the loss of limb and may therefore be classified as a higher K-level amputee, in comparison to an individual that undergoes amputation due to illness, such as diabetes. Therefore, the design of such a device to be cost-effective could ease the process of the amputees acquiring such a device, as the device would be less expensive. This may enable the private procurement or the procurement through an institution to happen more efficiently. A cost-effective, terrain-adaptive prosthetic ankle would therefore firstly help the procurement of a device capable of allowing a user to regain former mobility and secondly, such a device could help decrease the safety hazards experienced by amputees, while using ESAR prosthetic feet.

1.3 Objectives

The primary objective is to develop and validate a cost-effective terrain-adaptive prosthetic ankle. To this end, objectives are defined as a roadmap to this goal and are given in the list below.

1. Develop a system architecture that allows the conceptual system design to achieve terrain classification, increased toe clearance and stance phase stability by control of the system parameters.
2. Create a detailed mechanical design of a prosthetic ankle system, such that the prosthetic ankle system can withstand the dynamic loads it would experience from usage.
3. Detail design of an electronic system, consisting of sensors and a processing unit, as well as an output system to drive the mechanical parameters.
4. Design and implement a terrain-adaptive control system to enable the ankle system to classify and adapt to terrain and drive the mechanical parameters.
5. Manufacturing of a working prototype implementing the mechanical, electrical and controller designs.
6. Validate the functionality of the prosthetic ankle system using the test bench at a system level and validating each individual subsystem at a subsystem level to ensure that the system will function as designed.
7. Evaluate the system's performance in the validation step. This will allow for reflection on the design choices and to determine whether the designed requirements have been met.

1.4 Research Methodology

This study presents a structured research methodology, where the prosthetic ankle system is systematically designed. Starting at a literature review to provide an overview of literature in the relevant fields and determine the requirements for the prosthetic ankle system. The system is then designed combining a mechanical system validated by finite element analysis (FEA), power electronics and sensor systems and a hierarchical control system for terrain classification and system-level control.

1.5 Chapter Outline

This dissertation is structured in a logical progression from concept to completion and is outlined within the chapters as described in the list below.

1. **Chapter 2** - Chapter 2 explores relevant literature surrounding prosthetic ankles and discusses solutions to similar problems. The literature review covers relevant biomechanical topics surrounding the development of a prosthetic ankle, the mechanical design of prosthetic ankles that aim to achieve a similar goal, as well as terrain classification and sensor systems associated with prosthesis.

2. **Chapter 3** - Chapter 3 covers the system level design of the prosthetic ankle and follows the literature overview, as subsystem archetypes will be chosen based on their strengths and weaknesses discussed in Chapter 2. This chapter will also serve as a roadmap for further detail design as the subsystem types will be chosen, in order to address the problem statement outlined in Section 1.2.

3. **Chapter 4** - Chapter 4 is the detail design chapter and expands on the system level design done in Chapter 3. The mechanical, electronic, and control subsystems are designed in detail in this chapter.

4. **Chapter 5** - Chapter 5 focusses on the implementation and validation of the detail design of the system. This is done to draw conclusions on the design choices and determine whether the objectives have been met and how well the system solves the problem outlined in Section 1.2. The system is validated on subsystem level, where each subsystem is tested to determine whether the subsystem performs as expected. The system is also tested at a system level in comparison to an existing commercial solution, to evaluate key performance metrics.

5. **Chapter 6** - Chapter 6 summarises the findings in Chapter 5 and discusses the validity of the system in terms of the problem statement.

1.6 Conclusion

Due to the cost involved with commercial terrain-adaptive prosthetic ankles and the benefits terrain-adaptive ankles provide to amputees, it is important to design an accessible alternative with comparable functionality to commercial terrain-adaptive prosthetic ankles. This chapter outlines the objectives to achieve this goal and the dissertation structure. In the following chapters, the design process of such an ankle system will be followed in the hopes of providing a solution to the problem specified in Section 1.2.

Chapter 2

Literature Review

2.1 Introduction

Following the problem statement laid out in Section 1.2, a low-cost solution is needed for amputees in South Africa. Further design specifications include increasing toe clearance and stability for the amputee. Figure 2.1 shows the different prosthetic ankle modalities developed in pursuit of natural ankle-like performance. Conventional prosthetic feet were solid ankle feet using a cushioned heel to absorb the force of heel strike (see Section 2.2) and are typically rated for K1 amputees, as described in Table 1.1. ESR or ESAR prosthetic feet, which stands for "energy storage and return" and focus on storing energy in a flexible mechanical element to release back onto the terrain later in the gait cycle. "Bionic feet" refers to microprocessor-controlled prosthetic feet that either act to stabilise the amputee or propel the amputee forward using an electric motor.

This chapter will discuss the literature surrounding prosthetic ankles, the various electromechanical elements with relevance to the construction of prosthetic ankles and the control theory around solving the problems set out in the problem statement. As well as literature surrounding the gait cycle and the common problems faced by amputees.

Figure 2.1 outlines the different prosthetic ankle modalities commonly found in literature, which will be discussed later in this chapter in greater detail. This is done in an effort to understand the different prosthetic ankle modalities to eventually choose one to use as a reference to design a new prosthetic ankle from.

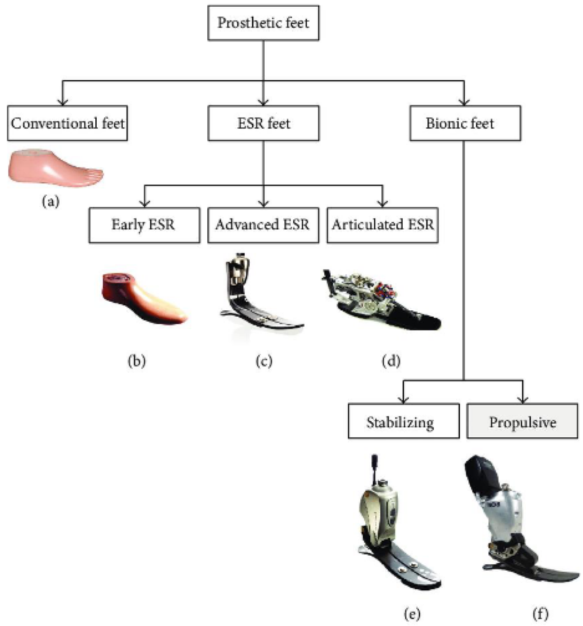

Figure 2.1: Prosthetic ankle modalities [9]

2.2 Gait cycle

The gait cycle is the cyclical motion of the leg during walking, which begins and ends with two successive strikes of the heel on the surface being traversed [10]. The gait cycle should be understood for clarification on the operation of the prosthetic ankle that will be designed in the coming chapters.

The gait cycle can be consists of two different states: the swing phase and the stance phase [11]. The stance phase of the gait cycle is defined as the portion of the gait cycle, where the leg is being loaded by the body, while the swing phase is defined as the portion of the cycle where the leg is unloaded and moved through space to take the next step [10]. Where the stance phase can make up approximately 60% of the gait cycle duration [11].

Figure 2.2 below, as adapted from [11] describes the gait cycle with reference to a single leg. The stance phase can be further divided into two different sections, single support, where the body is supported by one leg and double support, where the body is supported by both legs [11].

It can be further ascertained that the gait cycle can be divided into 8 basic subdivisions, in this case labelled from 0-7. Although each individual has a unique and identifiable gait, Figure 2.2 describes the basic cycle that is common among all able-bodied humans [10]. Individuality in the gait cycle and duration exist depending on the cadence and individual limb length and limb length ratios of the individual [10].

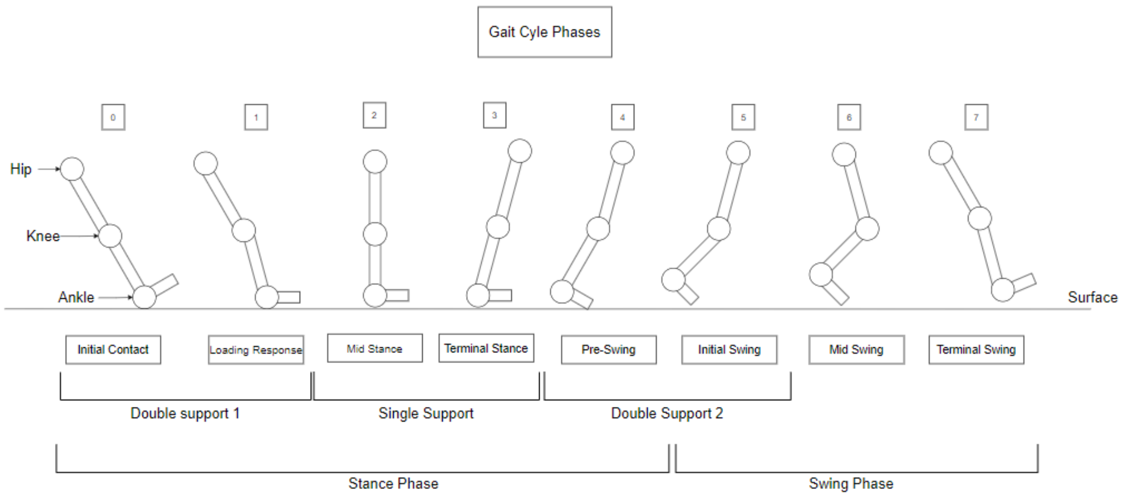

Figure 2.2: Labelled gait cycle

2.2.1 The role of the ankle in the gait cycle

Understanding the role of the ankle-foot complex in the gait cycle is essential for designing an effective prosthesis. The primary movement plane considered in this paper is the sagittal plane, as it is the main plane involved in normal forward walking on level terrain. The primary movements in the sagittal plane are plantar flexion and dorsiflexion, as shown in Figure 2.3 [12]. In the transverse plane, the ankle stabilizes through inversion and eversion, as shown in Figure 2.3 [12].

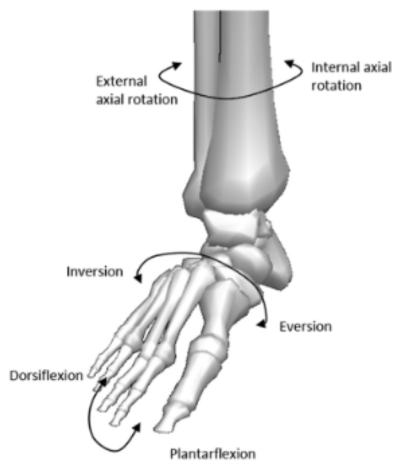

Figure 2.3: Ankle Foot Complex [12]

With ankle movements defined, the movement and work of the ankle can be further characterized. Figure 2.2 displays the different important phases of the gait cycle, these gait events will be used later in the terrain classification design in Section 3.4.2 to describe the system variables.

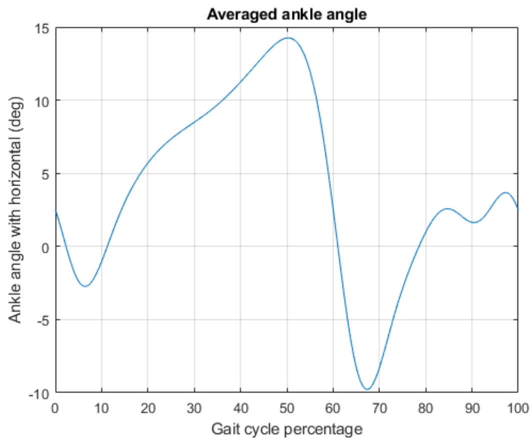

Figure 2.4: Ankle angle during gait cycle [13]

Figure 2.4 represents the average ankle movement (in degrees) of 10 healthy individuals, shown as a percentage of the gait cycle. The figure is processed from a dataset where 10 subjects walk on a treadmill at varying speeds and inclines as recorded by Embry et al. [13]. From Figure 2.4 the ankle angle is taken around the horizontal, meaning the positive ankle range represents dorsiflexion and negative angle range represents plantar flexion.

First to be considered is the movement made by the ankle during the gait cycle in the sagittal plane. At initial contact, the ankle starts in a dorsiflexed position, then during the loading response the heel is in contact with the surface and moves through controlled plantar flexion until the foot is flat on the surface as the ankle absorbs the heel strike force [12].

During mid-stance to terminal stance, the ankle dorsiflexes while the shank rotates forward, propelling the body forward. Then the ankle plantar flexes from terminal stance to pre-swing, this is where the most of the power is generated by the calf muscle around the ankle joint [12].

During the swing phase, the ankle undergoes dorsiflexion, this enables the toe to clear the surface being traversed which avoids tripping and stumbling [12].

Next, the mechanical impedance of the ankle will be discussed. The mechanical impedance can be described as the dynamic relationship between the joint position and the joint torque during the gait cycle [14]. It is generally described in terms of stiffness, damping, and inertia.

During the stance phase, the stiffness of the ankle was found to linearly increase from 0.35 - 6.42 Nm/rad per kilogram body weight, while it remains constant during the swing phase [14]. Damping changes less than ankle stiffness and ranges between 0.010 to 0.024 Nms/rad per kilogram of body weight [14]. The inertia was found to be relatively constant at 0.008 kgm^2 [14].

To fully characterize the ankle function during the gait cycle, the ankle speed, torque and power will be described. Figure 2.5, below is processed from data provided by [13] and shows ankle parameters of interest during the gait cycle.

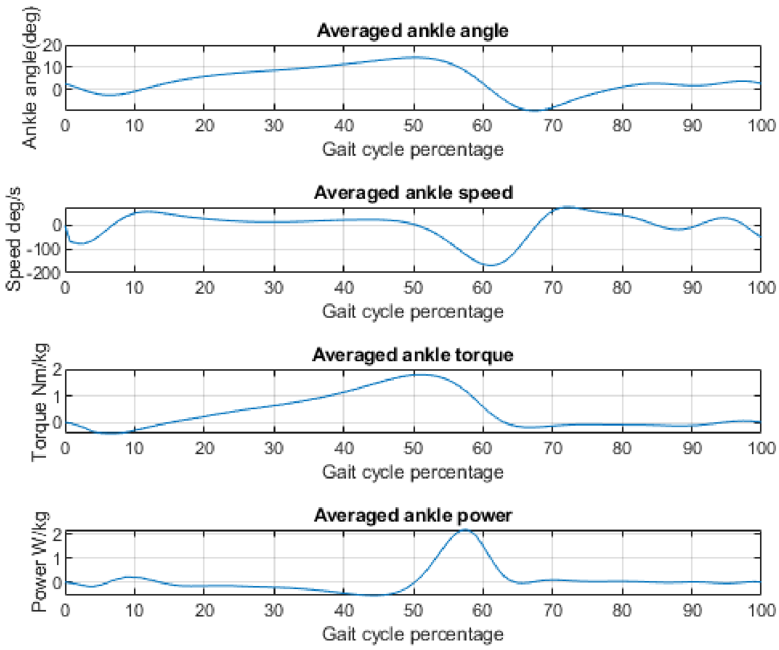

Figure 2.5: Ankle gait cycle parameters [13]

Therefore, it follows that the ankle joint in the sagittal plane can be characterised as a complex system that works to absorb force and propel the body forward, as well as preventing stumbling and tripping by dorsiflexion before the next heel strike.

2.3 Amputee safety and hazards involved with prosthetics

More than 50 % of lower limb amputees using prosthetics report falling at least once per year in a study performed by Kim et al. [8]. In this study, it was found that 57.6% of a sample of 66 trans-femoral and transtibial lower limb amputees reported falling at least once during the previous year, where most of the falls were caused by a disruption of the base of support of the amputee [8]. Figure 2.6 summarizes base of support falls as resulting from tripping, slipping, or inadequate base of support. These base of support types of falls can either be caused intrinsically, where the destabilizing force originates from the user or, extrinsically, where the force originates from the environment.

In a study performed by Chen et al., it was found that tripping over an obstacle is more likely when unwanted contact is made with the toe as opposed to any other part of the foot [15]. Similarly, it was found that humans commonly shorten their step length when traversing an obstacle, where the risk of tripping is high [15].

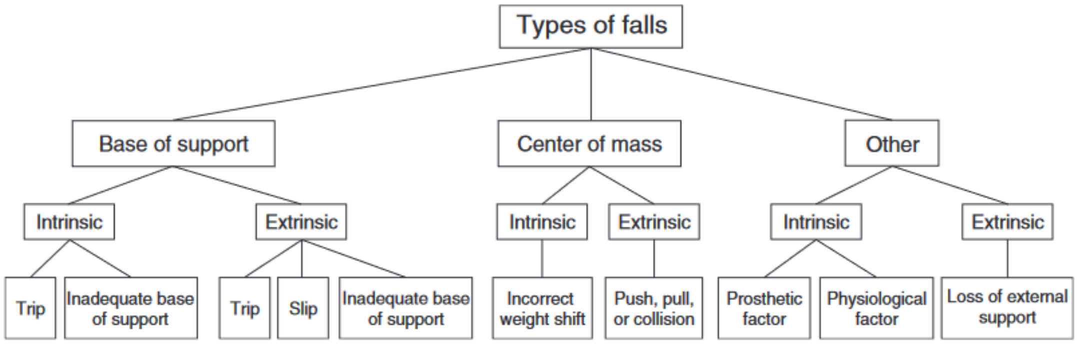

Figure 2.6: Types of falls [8]

Minimum toe clearance is defined as the minimum vertical distance between the foot and the ground, during the mid-swing portion of the gait cycle [16]. If the toe makes contact with the surface being traversed, the risk of falling is highest during mid-swing and decreases as the swing phase of the gait cycle continues [15]. This occurs because the individual's centre of mass is leaning forward, outside the base of support, if the toe makes contact with the surface at mid-swing [15]. While if the toe were to make contact with the surface later in the swing phase, the centre of mass is above the base of support, decreasing the risk of falling.

Now that it can be understood that tripping is a real and definitive hazard for unilateral amputees, it is important to discuss the different circumstances in which tripping may occur. Factors that may influence the minimum toe clearance of a prosthetic include the amputee's age, cognition and sensory conditions, such as poor visibility [15],[16]. As well as control of the toe clearance done by the prosthetic [16] and the type of terrain or obstacles on the terrain being traversed [8].

According to Kim et al. [8], another common extrinsic fall modality is slipping, as shown in Figure 2.6. Slipping was the most commonly reported fall modality in the study performed by [8], accounting for 26 %, followed by tripping 22 % and prosthetic factors also 22 %.

It is important to understand the potential causes of the most commonly reported fall modalities in order to properly design a prosthetic with the aim of preventing them. Concurrently, the most common activity being performed at the time of the falls was walking on level terrain, followed by walking on uneven terrain [8]. Uneven surfaces can lead to higher tripping probability, because the toe clearance can be decreased if the prosthetic ankle being used does not lift the toe to account for this [16]. Furthermore, inadequate base of support can be caused by prosthetic factors, such as a prosthetic breaking or being inadequately fastened to the prosthetic socket fittings [8]. Slipping can be described as a fall due to inadequate friction between the prosthetic and the surface being traversed. Figure 2.7 below is a summary of the fall modalities recorded and the prevalence of each.

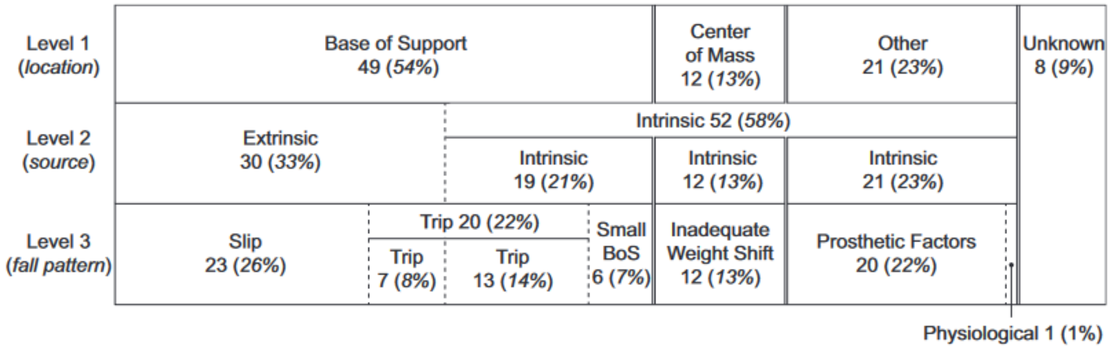

Figure 2.7: Causes and prevalence of falls [8]

Therefore, it can be reasonably deduced, that increasing the minimum toe clearance (MTC) during the mid swing portion of the gait cycle would be beneficial to an amputee. It can be similarly deduced that a flat foot placement during the stance phase would increase the friction between the prosthetic and the surface, which could potentially decrease the probability for slipping to occur. This is what current microprocessor controlled prosthetic ankles aim to achieve [16]. This will also be considered to form part of the high level design criteria for the prosthetic ankle to be designed.

Furthermore, according to a study performed by Sheehan and Gottschall, at similar inclinations, there exists an elevated probability of falling, when walking on slopes in comparison to walking on staircases [17]. This was done by measuring the probability of falling while walking on a 33° staircase and slope with a 25 m walkway. This study was performed on healthy non-amputated adults, the fall risk is only exaggerated in amputees as it was found that when walking on an uneven surface, the MTC measured on transtibial amputees was less on the prosthetic side than on the healthy side [18]. To illustrate the significance of this, it was found that an articulation microprocessor control hydraulic ankle was shown to have a lower tripping probability when walking on ramps than fixed ankle energy storage and return prosthetics [16].

As non-articulating energy storage and return ankles are unable to provide active dorsiflexion, amputees develop compensatory movements to allow for toe clearance when walking at elevated speeds [19] and inclinations [6]. Compensatory movements performed by other muscle groups can lead to overuse injury in lower limb amputees, as 59% of all lower limb amputees develop at least one musculoskeletal overuse injury within the first year of using prosthetics [5].

Therefore, detection of ramps or slopes to provide the necessary toe clearance is important to improve the safety of the amputee by decreasing the tripping probability. This will form part of the high level design deliverables. The MTC during the mid swing phase should also be improved, as this will decrease the risk of tripping from the toe snagging on the surface being traversed. The stability during the stance phase should also be improved, as this will decrease the probability of slipping due to minimal friction between the prosthetic and the surface.

2.4 Mechanical prosthetic ankle modalities

There have been many attempts in literature to approximate the functionality of the ankle in one way or another to provide a better functioning prosthetic ankle. This section will provide an overview of recent technologies in the field, starting with basic passive Energy storage and return (ESAR) prosthesis and moving to more advanced electro-mechanical technologies, as can be seen in Figure 2.1.

Refer to Figure 2.1 for a basic roadmap of the field. Other terminology that is relevant to understand is the terminology of passive, semi-active and active prosthesis. Passive prostheses are defined as prostheses that attempt to approximate the stiffness and damping of a natural ankle, as discussed in Section 2.2.1. Passive prostheses achieve this using a fixed cantilever blade spring with either a fixed or articulated ankle, as seen in Figure 2.8 (a) [20].

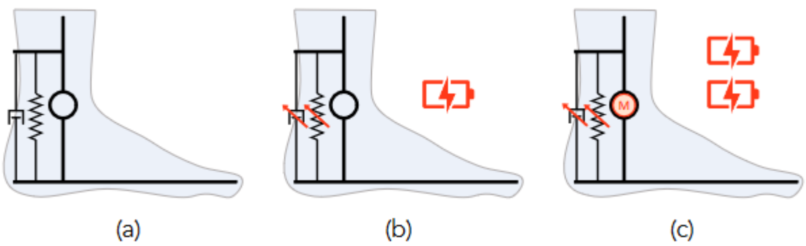

Figure 2.8: Prosthetic ankle technologies [20]

Semi-active prostheses are defined as microprocessor-controlled prostheses that can adjust their physical properties to aid the amputee in different situations [20]. A systematic representation of a semi-active prosthetic ankle can be seen in Figure 2.8 (b).

Active or powered prosthesis can be defined as prosthesis that uses an external motor to increase the power output of the prosthetic, this in turn leads to a higher power consumption of the prosthetic [20]. A representation of this can be seen in Figure 2.8 (c).

2.4.1 Passive prosthetic ankles

ESAR prostheses are robust, and because they do not require external power or a microcontroller, failure modes are limited to mechanical failures. The precursor to the ESAR prosthetic ankle is the solid ankle cushioned heel (SACH) prosthetic ankle as seen in Figure 2.1 (a), this prosthetic provides basic functionality by supporting the weight of an amputee and absorbing the force on heel strike with the heel [21]. The SACH prosthetic ankle does not provide any energy return and therefore, does not assist with propulsion during the gait cycle [21]. This translates to increased compensatory movement from the amputee and gait asymmetries, such as much greater activation of the hip muscles on the intact limb [6].

Energy storage and return prosthesis aim to increase propulsion of the amputee by storing energy during the mid-stance to terminal stance phase in the controlled dorsiflexion of the ankle and releasing this stored energy later in the gait cycle [21]. This allows for a more natural gait, as the range of motion (ROM) of the flexible carbon blade of the prosthetic foot, allows for greater dorsiflexion than the SACH prosthetic counterparts [22].

As discussed in Section 2.3, there exist issues with this type of passive prosthesis. Namely, tripping and slipping hazards and overuse injuries due to compensatory movements needed to make up for the lost muscle activation in the residual limb. However, there exist improvements on the conventional ESAR transtibial prosthetic, which include an articulated ankle joint that allows and even greater ROM and toe clearance [16].

One such hydraulic articulated prosthetic ankle, designed by Naseri et al., utilises a passive hydraulic dampener that is adjustable in both plantar flexion and dorsiflexion to assist with sloped walking. The effect of the hydraulic dampener design, in series with the carbon leaf spring foot blades, is that the dorsiflexion of the ankle is increased, causing a more natural gait. Figure 2.9 below shows the mechanical impedance model of the passive hydraulic ankle by Naseri et al. [23].

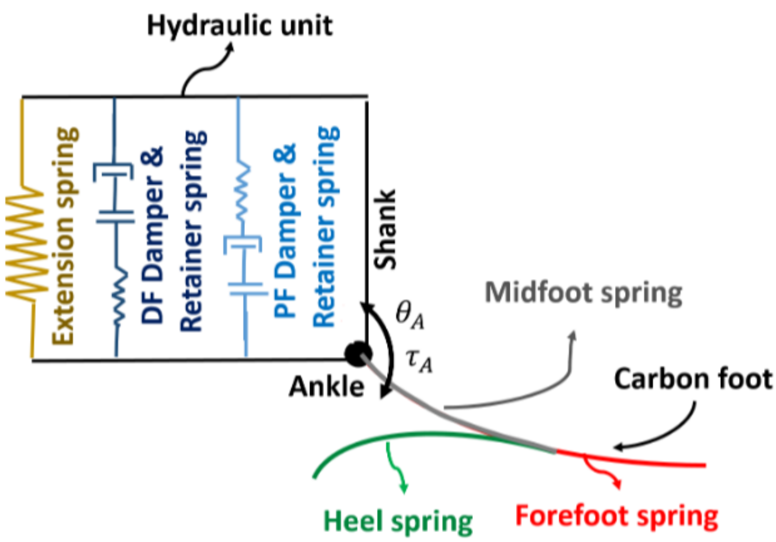

Figure 2.9: Passive hydraulic ankle mechanical impedance model [23]

To achieve such a hydraulic dampener, two separate mechanically adjustable flow valves were used. Each adjustable valve only adjusts the flow rate in one direction of flow and therefore, the damping coefficient in one direction of the dampener. This allows the prosthetic ankle to be adjusted separately for plantar flexion and dorsiflexion [23]. The hydraulic circuit used by Naseri et al. is shown in Figure 2.10 below.

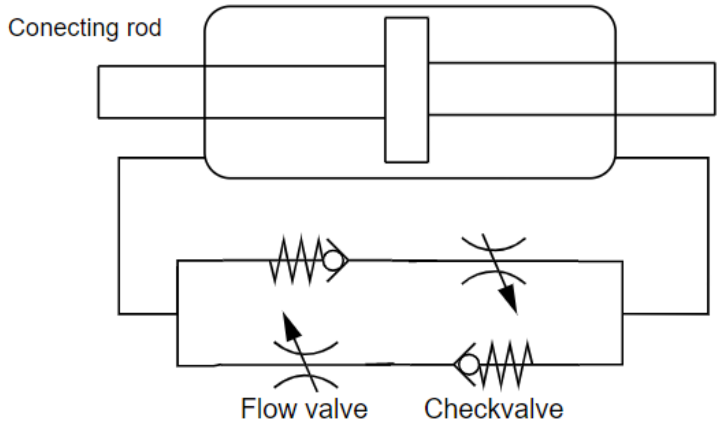

Figure 2.10: Hydraulic circuit

Passive articulating prosthetic ankles have the benefit of increased range of motion and toe clearance, which may lead to a reduction in the problems discussed in Section 2.3. These prosthetic ankles still have certain shortcomings in terms of adaptability to different terrain, as the ankle parameters do not adjust automatically and must be adjusted manually for the task at hand. This is reflected in the study performed by Riveras et al., where it was found that passive hydraulic ankles do in fact improve MTC and lower tripping probability, however less so than their microprocessor controlled counterparts [16].

2.4.2 Semi-active prosthetic ankles

Using microprocessors to control the parameters of a prosthetic has several performance benefits in terms of increased MTC and decreased tripping probability [16]. However, this does add a layer of complexity to the system which may lead to decreased robustness, as failure may occur on either the mechanical or control system level of the prosthetic.

One of the more common technologies used in prosthetic ankles are hydraulic variable dampeners, as reflected on the commercial market. One such example is a semi-active hydraulic dampening system for use in ankle prosthesis, consisting of a hydraulic cylinder with a hydraulic servo valve [24].

The hydraulic cylinder can be used in combination with the servo valves to alter the damping coefficient of the prosthetic ankle, which can be used to control the mechanical

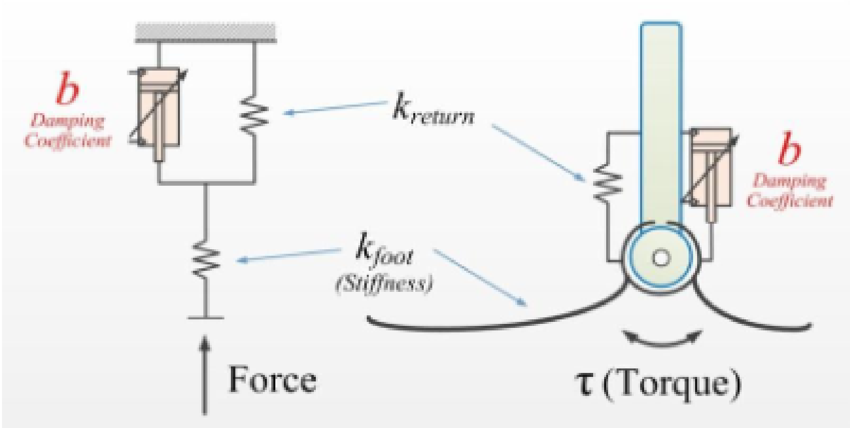

Figure 2.11: Semi-active hydraulic ankle [24]

impedance of the ankle to better approximate the response of the natural human ankle [24]. Such a hydraulic semi-active prosthetic has the potential advantage of being terrain-adaptive over the passive hydraulic prosthetic ankle, while using a small energy source, as the servo-valves are not very energy intensive. This system would be similar in principle to the system described in Figure 2.10, with the only difference being that the flow valves are controlled electro-mechanically.

Another semi-active prosthetic ankle modality in literature is a variable stiffness prosthetic foot that uses a movable fulcrum to adjust the support on a composite leaf string, resulting in a variable stiffness by Glanzer [25]. Figure 2.12 below shows the variable stiffness prosthetic foot, where the fulcrum and slide along which the fulcrum move are clearly visible [25]. Although the variable stiffness prosthetic foot utilizes an external motor to move the fulcrum, according to the definition of a semi-active prosthetic ankle discussed in Section 2.4, the variable stiffness prosthetic is a microprocessor controlled ankle prosthetic that controls the mechanical impedance based on user activity [25].

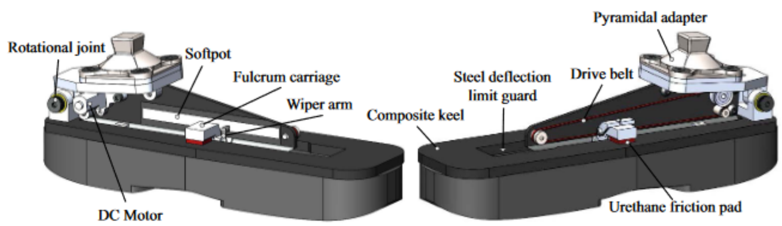

Figure 2.12: Variable stiffness prosthetic foot by Glanzer [25]

The variable stiffness foot achieves stiffness modulation in a compact and lightweight package [25]. However, the variable stiffness foot has a fixed stiffness range and must be adapted for each individual to suit their individual needs [25]. The variable stiffness foot also is designed to assist the user in the stance phase and has no mechanism to assist with increase in toe clearance.

Although toe clearance can be adequately achieved using a passive or semi-active hydraulic prosthetic ankle, only the semi-active hydraulic prosthetic ankle can adjust to walking speeds and different terrains. However, these hydraulic systems are expensive to manufacture due to the tolerances and materials required. Additionally, the hydraulic prosthetic ankles are reactionary, as the damping coefficients may be adapted by servo valves, however hydraulic prosthetics without an actuator rely on the reaction forces of the amputee transferring weight onto the prosthetic for the gait to be advanced. With an active system, an actuator is used to stabilize or output force and assist the user in the gait cycle. This allows the system to anticipate the step before it is taken, which has benefits that will be discussed in Section 2.4.3.

2.4.3 Active prosthetic ankles

Active prosthetic ankles can be classified as robotic or motorised prosthetic ankles; however, the goal of the implementation of the motorisation may differ. Prosthetic ankles are motorised to either achieve a net positive power output and assist the user in forward propulsion, or to achieve stability by adapting to terrains and increasing MTC.

First, the propulsive active prosthetic ankle will be discussed. Although propulsive active prosthetic ankles are not currently available commercially, many such examples can be found in literature. To understand the working principles and the mechanical actuation used, several examples will be discussed in some detail.

First, the active prosthetic ankle, designed by Caprini et al., will be discussed. The prosthetic, designed by Caprini et al., aims to output an actively controlled torque to assist the user in the gait cycle. This prosthetic is designed around a brushless motor connected to a harmonic reduction drive, the output of the motor and harmonic drive is then connected to passive foot blades [26]. The working principle can be seen in Figure 2.13 below.

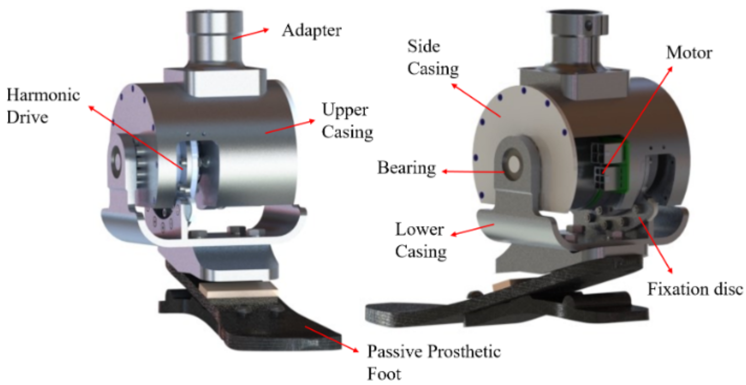

Figure 2.13: Active ankle by Caprini et al. [26]

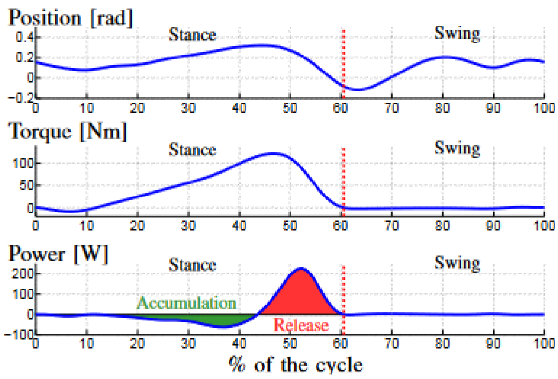

Figure 2.14: Energy storage and return in SEA prosthetics [27]

The active prosthetic ankle by Caprini et al., was able to output 200W with a peak torque of 1.02Nm/kg, with a total mass of 1.633 kg [26]. A simulation conducted by Caprini et al., on the prosthetic, showed that the ankle is capable of closely following the ankle angle during walking on a level surface at a cadence of 1 second per step. With the motor and drive system being able to output 85% of the required torque and 92% of the required ankle speed [26].

The design of the active prosthetic ankle, presented by Caprini et al., follows a topology where a motor is connected through a gearbox directly to the foot blades. This allows the system to be modular for amputees with different desired foot lengths. Another development in the field of active prosthetic ankles is the use of series elastic actuation (SEA), to decrease the peak power consumed by the motor [27]. The use of SEA in a lower limb prosthetic allows for the accumulation of work in the elastic element of the prosthetic during the controlled dorsiflexion of the stance phase, as can be seen in Figure 2.14.

Another active prosthetic, designed by Covens et al., uses a series clutched elastic actuator, which stores energy in an elastic element to decrease the peak motor power requirement. Covens et al., found that the electrical peak power was reduced by 17-21% by using this clutched elastic actuator [28]. Figure 2.15 below, shows the mechanical topology of the prosthetic ankle designed by Convens et al.[28].

The resettable overrunning clutch (RORC), as shown in Figure 2.15, allows the ankle joint to be locked such that the force is not transmitted to the ball screw [28]. This has the advantage of decreasing the electrical energy consumed by the motor for longer and higher loads [28].

SEA actuated ankle prosthesis can use many different mechanical drive train topologies to move energy into and out of the elastic element. Another such SEA prosthetic by Dong et al.[29] presents a geared five bar spring mechanism to load the spring for the prosthetic foot. The use of the geared five bar mechanism was found to be able to decrease the peak

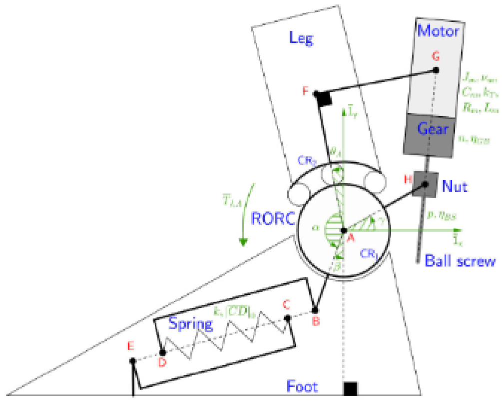

Figure 2.15: Convens et al., active prosthetic ankle [28]

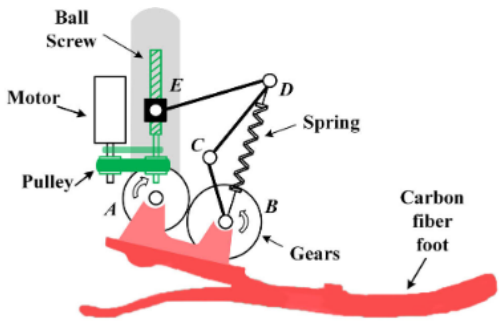

Figure 2.16: Five bar active ankle [29]

motor power by 35.3% [29]. Figure 2.16 shows the 5 bar topology, where the motor drives a lead screw and nut, which forms one arm of the geared five bar mechanism.

Au et al. presents a SEA actuated ankle prosthetic that aims to approximate the impedance of the natural ankle foot complex by varying the impedance during the stance phase [30]. This is achieved by the use of a unidirectional spring in parallel with a SEA consisting of a high power DC motor connected to an elastic element through a bevel gear transmission [31]. A high-level mechanical overview of the prosthetic ankle, designed by Au et al., is provided in Figure 2.17 below.

In summary, it can be surmised that most powered ankle-foot prosthesis in literature make use of a high power DC motor to transmit power through a transmission system to the surface to provide a net positive power output. However, it has been found that the use of a series elastic element can decrease the peak power output [27],[28],[29]. However, the peak power required by an ankle prosthesis aiming to provide a positive power output during the stance phase at a walking speed of 1 m/s is around 2.1 W/kg, as can be seen in Figure 2.5. If a hypothetical SEA ankle-foot prosthesis were able to decrease the peak power of the motor by 30% the motor required would still be substantially powerful. Therefore, supplying power to the motor becomes a limiting factor. This point can be demonstrated

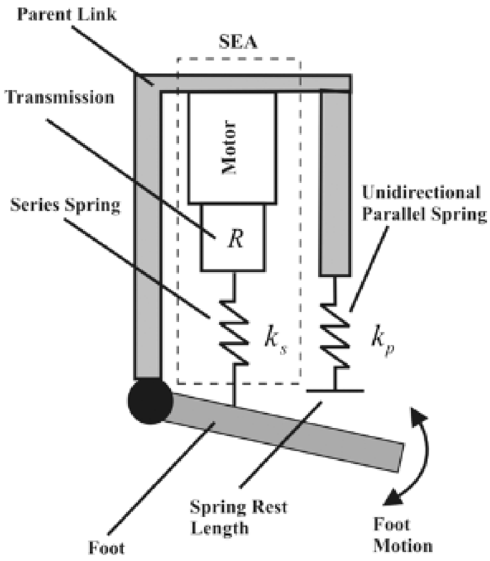

Figure 2.17: Powered ankle foot prosthesis [31]

by the use of a wearable power supply implemented to be able to power the prosthetic by Au et al.[31].

The next type of active ankle-foot prosthesis to be discussed are stabilizing prosthesis and aim to increase user MTC and ground contact. While these active prosthesis use actuation systems to move the physical parameters of the ankle, these actuation systems do not require much power, as these prosthetics only aim to move the ankle during the swing phase when no load is placed on the ankle.

One such example is a robotic four-bar mechanism, with an actuator that actuates a lead screw through a belt and pulley transmission system, by Chang et al. [32]. This prosthetic ankle utilises a flexible foot blade that acts as a passive prosthetic during the stance phase, which helps conserve energy [32]. Figure 2.18 below shows a diagram of the prosthetic ankle by Chang et al.

The prosthetic, designed by Chang et al., has a weight of 1.65 kg [32]. The weight of such an active prosthetic is a factor as it influences the socket suspension of the amputee [33]. Another active prosthetic that is aimed at minimizing the weight and size of the system is a robotic prosthetic ankle by Lenzi et al. [34]. Lenzi et al. utilized a cam based transmission to decrease the build height and weight of the prosthetic while being able to increase the MTC and decrease the risk of falling of the user [34]. The cam based mechanism is driven by a DC motor and lead screw, and the ankle module is connected to flexible carbon foot blades [34]. The ankle behaves passively in the stance phase due to the transmission mechanism being non-back driveable [34]. Figure 2.19 below shows the front and back views of the active ankle by Lenzi et al.

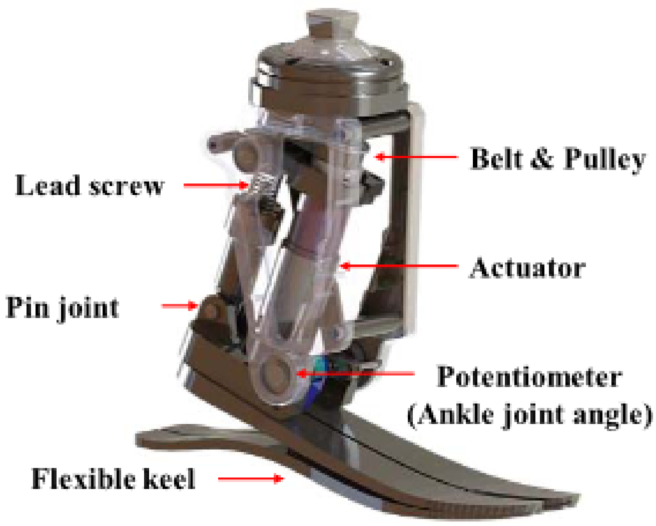

Figure 2.18: Robotic prosthetic ankle by Chang et al. [32]

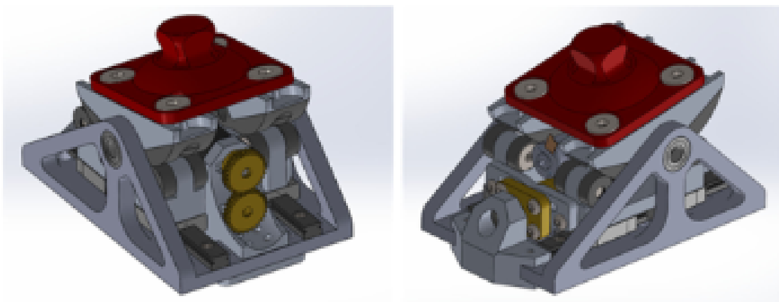

Figure 2.19: Non-back drivable cam based robotic ankle [34]

Commercially, powered prosthetic ankles are scarce, however there exists one powered prosthetic that has been greatly successful. Namely, the Propriofoot from Össur, which has shown to increase MTC, improve gait symmetry and reduce pressure on the residual limb [35], [36], [37]. The Propriofoot from Össur is therefore proven to be effective and aims to minimize the challenges faced by lower limb amputees described in Section 2.3. There are however, several shortcomings of the Priopriofoot, which makes it inaccessible to many amputees such as a high build height of 180 mm and a weight of 1.4 kg [33]. As well as a price of $20 000-$25 000 which translates to R363 400 - R454 250 [38]. Figure 2.20 below shows the Propriofoot as taken from the Össur catalogue.

Now that all the different mechanical prosthetic ankle topologies have been discussed, as per the problem outline, the ankle to be designed must be both low-cost and capable of adapting to different terrains. Therefore, the prosthetic ankle must be capable of detecting the terrain by the use of sensors, after which a control system is needed to convert the sensor data to usable output such that the ankle prosthetic is capable of adapting to different terrain. For this reason, sensors and sensing techniques typically used

Figure 2.20: Össur Propriofoot [39]

in prosthesis will be discussed as control architectures and detection systems commonly used in prosthetics.

2.5 Sensors and terrain measuring systems

Sensing methods for detecting different locomotion states, such as the terrain being traversed and walking speeds, are implemented in modern prostheses to help overcome some of the challenges discussed in Section 2.3. This section discusses different sensing techniques relevant to prostheses, with the aim of selecting an appropriate sensing strategy for detecting and adjusting to changes in terrain.

First, it is important to understand that sensing strategies for the use in prosthesis can be categorized as either proprioceptive or exteroceptive. Proprioceptive sensing techniques use sensors that can detect states of the prosthetic or of the residual limb in space, whereas exteroceptive sensing techniques use sensors capable of detecting the terrain being traversed directly. Quantifying the difference between the different sensing techniques can be done using the prediction time, which is defined as the time between the change in locomotion mode and the time when the change is detected [7].

Secondly, the sensor data is typically passed to some detection algorithm in order to convert abstract sensor data into a usable terrain estimation. Depending on the sensing modality, different detection algorithms will be required.

2.5.1 Proprioceptive sensors and detection systems

Proprioceptive sensors will be discussed first, as proprioceptive sensors are simpler in computational requirements and are not suitable for use in visually impaired users, as the proprioceptive sensing techniques rely on the exteroception of the user [7]. Typical sensors used in a proprioceptive sensing scheme include EMG or electromyographic sensors, capacitive sensors, strain gauges and IMUs or inertial measurement units [7].

EMG sensors detect the electrical signals sent to muscles to initiate contraction and can be used to detect the terrain based on observable trends in muscle activation when traversing different terrains [40]. Electrical signals from the muscle activation are readable around 100 ms before the movement is initiated [7].

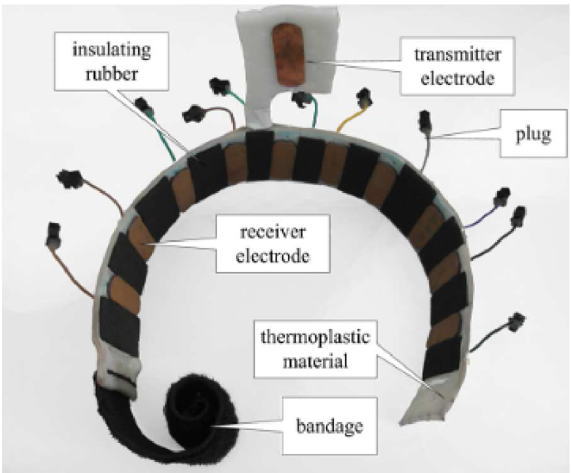

Figure 2.21: Example of capacitive sensor [41]

Mechanical sensors are sensors used to directly measure the mechanical configuration of the device or the user, examples are inertial measurement units (IMU) and load cells or other force measurement equipment. Inertial measurement units are typically made up of a combination of micro electromechanical sensors (MEMS), including some combination of accelerometer, gyroscope and barometers [42]. This allows the IMU to be used to accurately measure the position of the device in space. Load cells or other force measuring systems typically use strain gauges to detect a force under the yield stress point of the material it is applied to.

In practice, a single sensor reading may not be able to provide adequate information of the state of the device to infer the terrain, in the case of proprioceptive sensing techniques [7]. Therefore, sensor fusion techniques combine the information obtained from different sensors to more accurately estimate the terrain. In the review article by Al-dabbagh and Ali, sensor fusion between mechanical sensors and EMG sensors were found to be favorable with all instances having a terrain detection accuracy of above 95%, using various classification algorithms [7]. Others like Chang et al.have used sensor fusion between IMU and load cells to detect a multitude of different commonly faced terrains, such as ramps and slopes with an accuracy of 97.5%, using fuzzy logic [32].

Now that proprioceptive sensors have been discussed, different classification algorithms must be discussed as the sensor data by itself is not typically enough information to identify the terrain being traversed. Different classifiers and terrain identification systems used with proprioceptive sensor systems are linear discriminant analysis (LDA), quadratic discriminant analysis (QDA), support vector machine classifier (SVM) [7] and fuzzy logic classifiers [32],[43]. These detection systems all use one or more variables derived from sensor data of the physical state of the prosthesis or the user, such as measurements at different phases of the gait cycle [32].

The prediction capacity, or the time taken between the change in locomotion to the detection of the changing terrain of proprioceptive sensing systems are typically lower than exteroceptive sensing systems [7]. As the proprioceptive sensing systems must first be placed on the changed terrain where the user is expected to react, before the system can adjust to the change in terrain.

2.5.2 Exteroceptive sensors and detection systems

Exteroceptive sensing systems use sensors capable of detecting the terrain itself, allowing the system to anticipate terrain changes a few milliseconds in advance [7]. This results in a much higher prediction capacity, as the time between the terrain change and its detection is short. Proprioceptive sensors are unable to detect the change in terrain before the change occurs, and are therefore reactionary and have low prediction capacity.

Sensors involved in exteroceptive systems include some depth or ranging sensor, however since the sensor is mounted to a moving prosthetic, many systems incorporate an IMU. Ranging sensors will be discussed first and can be classified on whether the sensor emits a single or multiple beams. Ranging sensors include ultrasonic, laser, radar and light detection and ranging (LIDAR) sensors [7].

On a high level, all these sensors emit a signal, either light or sound, onto the surface being traversed and then use the reflected signal to determine the terrain being traversed. However, for the sensor to function properly, it is important for the sensor not be obstructed by the user while in operation. To that end, ranging sensors have been mounted on different areas of the body, such as the shank, waist or chest. Range sensors may use similar classification techniques as mentioned previously, such as SVMs [7].

Depth sensors are a low-cost, more compact alternative to range sensor systems [7]. Passive depth sensors utilize two full colour spectrum (RGB), cameras where the range is calculated by triangulation of matching pixels in both images [44]. Active depth sensors, however, calculate the phase shift between the transmitted and received light, using time-of-flight cameras (TOF) [45]. Active depth sensors can work in dimly lit environments, however may fail in some low contrast environments or in direct sunlight [7].

Similar to range sensor configurations, depth sensors may be mounted on the head, chest or leg of the user [7]. However, depth sensors require a much more in depth signal analysis, as classification algorithms can either utilize 2-dimensional or 3-dimensional imaging [7].

2.6 Controller architecture for prosthesis

Bipedal locomotion is inherently unstable, and active control of a prosthetic device may interfere with the user's walking intent if implemented incorrectly. Incorrect control of a prosthetic device may cause the user to be unstable, or fall in a worst case scenario, which may lead to injury.

A review by Tucker et al. suggests a hierarchical control architecture for control of prosthesis. Figure 2.22 below, shows the control architecture suggested by Tucker et al. Because both the user and the control architecture provide an output to a set of stimuli, it is recommended not to switch between two different output modes in a single step [46].

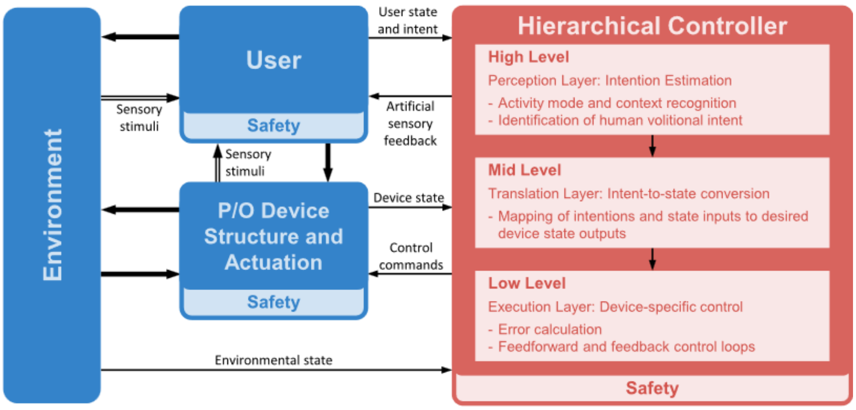

Figure 2.22: Control architecture [46]

The architecture outlined by Tucker et al. can accommodate any mechanical actuation or parameter configurations, as the physical outputs and sensor inputs can be selected based on design requirements. Section 2.5 discusses the different sensor configurations used in prosthesis and terrain estimation systems associated with them. The high-level control discussed by Tucker et al. is used to detect the user's intent, such as walking speed and terrain being traversed, and processes filtered sensor data containing information about the user's state and/or the environmental state as input [46].

The mid-level controller receives input from the high-level controller, which estimates parameters such as terrain and walking speed. Additionally, using sensor data on the device's state, the mid-level controller maps the difference between the desired and current device state and converts this into a physical output to pass to the low level controller [46].

The low-level controller then uses the physical reference inputs provided by the mid-level controller to physically control the output of the device. The low level controller is the physical control of the parameters of the device, depending on the mechanical design of the prosthetic itself [46].

2.7 Summary of literature review

This chapter reviews multiple prosthetic ankle systems with similar goals, with the goal of determining a prosthetic ankle architecture suited for this application. This architecture will be decided in the coming design chapters. The architecture will be chosen based on functionality and cost.

Important gait characteristics were explored, including the gait cycle and important characteristics that influence user safety, such as stance phase stability and swing phase toe clearance. In the coming design chapters, the prosthetic ankle will be designed to solve the problem outlined in the problem statement in Section 1.2. Focus will therefore be placed on developing a prosthetic ankle system that is capable of adapting to terrain, while being cost-effective. Focus will also be placed on designing for user safety, meaning increasing the toe clearance during the swing phase and increasing stance phase stability.

Chapter 3

System level design

3.1 Introduction

This chapter will discuss important high-level design choices made to provide a viable solution to the problem outlined in the problem statement of Section 1.2. A brief review is provided here for the readers' convenience. A prosthetic ankle is required with comparable functionality to commercial terrain-adaptive ankles; however, it must be cost-effective in an attempt to make high-functioning prostheses available to people in need. Therefore, following from the literature review provided in Chapter 2, a high-level design will be constructed to solve the problem, outlining important design choices such as the actuation and sensor topologies.

3.2 High level design requirements and considerations

At a basic level, given a set of inputs from the user and terrain, the prosthetic ankle must detect terrain or change in terrain and provide a physical output to improve the MTC and foot placement to provide a safer walking experience to a user at a low price. As the production price of a finalised product is typically much cheaper than the cost of prototyping, because of the time spent prototyping, the cost of the prosthetic ankle will only be calculated from the parts required to produce one unit.

The prosthetic ankle will not be designed with the goal of creating a net positive output power, as many of the prosthetic ankles in the literature discussed in Section 2.4.3. This is because of the high power requirements of such a prosthetic, which requires a significant power source. Due to the limitations on battery technology, it is currently infeasible to design a system for everyday use requiring a maximum output torque of 2 W/kg, as seen in Figure 2.5. This can be reduced by about 20-30 % using a SEA mechanism as discussed in Section 2.4.3. However, this is still a substantial peak power requiring a high torque motor, which leads to high current consumption, which will cause a short operational use time.

The high-level operation of the system may follow a scheme as presented in Figure 3.1 below. An input from the terrain and user is taken to identify and change the physical actuation of the prosthetic ankle. Since MTC and foot placement are of concern, controlled dorsiflexion and plantar flexion of the prosthetic ankle are needed to both lift the toe and place the foot firmly on the surface. The design scheme presented below in Figure 3.1 refers back to Section 2.5 for the control architecture.

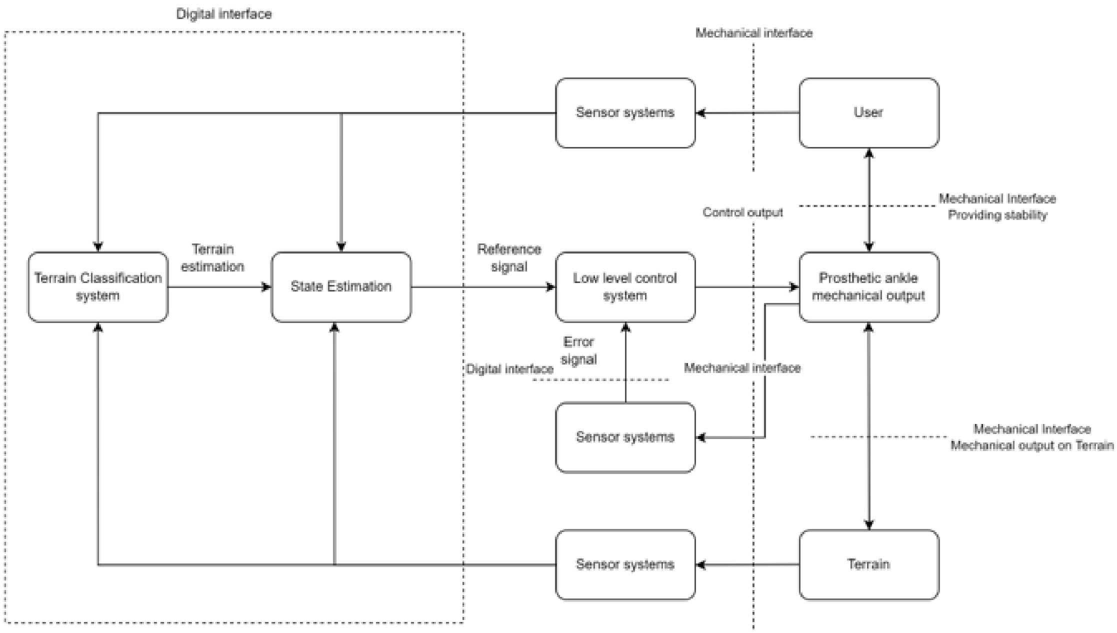

Figure 3.1: High level prosthetic ankle architecture

From the prosthetic ankle high-level system representation in Figure 3.1, it can be seen that the general control system architecture is derived from literature as discussed in Section 2.5. Further, some actuation or physical parameters must be implemented to be able to physically adapt to changes in terrain and provide a safe walking experience to a user. In the coming sections, it is important to derive an appropriate mechanical design to provide a solution to the problem set out in the problem statement in Section 1.2.

However, continuing from the problem statement in Section 1.2, it is important to make a set of requirements that the system must adhere to. As the main required output is increased MTC and better stance phase stability at different terrains, the speed and duration of the controlled dorsiflexion can be derived from the controlled dorsiflexion in the swing phase of a natural ankle. Further, the mechanical design parameters can be deduced from literature as well as data collected by Embry et al. [13]. The mechanical design parameters will be discussed further during the detail mechanical design process, outlined in Section 4.2.

By analysing the average ankle angle at a walking speed of 1 m/s, it is possible to analyse the behaviour of a natural ankle during the gait cycle, as recorded by Embry et al [13]. The gait phases can be found by analysing the average pressure plate data for the participants at the same walking speed and incline, as discussed in Section 2.5. Figure 3.2 below shows the ankle angle with marked gait phases, as described in Section 2.2.

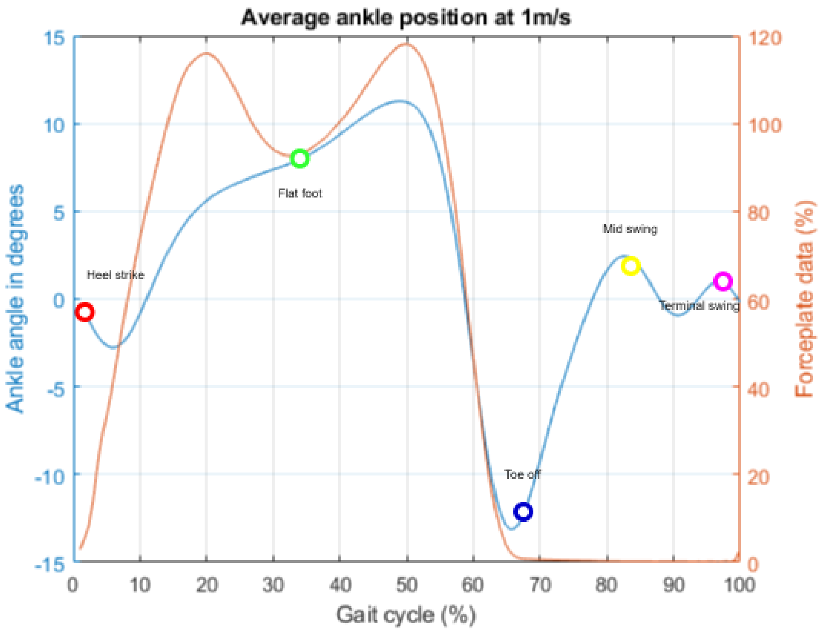

Figure 3.2: Ankle angle at gait phases

It can be seen from Figure 3.2 that the ankle angle at mid-swing is a mere 2.45°more than the terrain inclinations. This allows sufficient toe clearance to clear the terrain to take the next step. Which provides 6.41 mm of toe clearance, assuming an average distance between the ankle and toe to be 150 mm. Further analysis of the ankle angle between the toe-off event and mid-swing event allows an approximation of the average ankle speed as the gradient of a straight line drawn between the two points. Therefore, the average ankle speed in dorsiflexion can be approximated as 118.23 °/s at 1 m/s walking speed and an average step cadence of 1.186 s per step. The averaged cadence was calculated by taking the average step time for each participant in the trial conducted by Embry et al. [13].

Therefore, by analysing the characteristics of a natural ankle during the gait cycle, two important design requirements were found. The prosthetic ankle must be able to provide at least 5°of toe clearance over the terrain inclination at mid-swing and achieve this at a speed of 120°/s.

Further, the prosthetic ankle must be able to provide support for the user during the stance phase. During which, the prosthetic ankle will not aim to output a net positive power onto the terrain. The prosthetic ankle must be at least able to support the user during normal walking speed. Therefore, the prosthetic ankle must be mechanically stable and able to provide support for the user during the stance phase. The maximum torque experienced by a healthy ankle joint during the stance phase is about 1.5 Nm/kg of body weight [30], [13]. The prosthetic ankle will be designed for a maximum user weight of 90 kg, although many commercial solutions are designed around a 130 kg maximum user weight. As this is a prototype, an increased mechanical design constraint will mean more time in the development of the prosthetic ankle, and for this reason, 90 kg was chosen as an acceptable design requirement.

Therefore, in summary of the requirements, the prosthetic ankle must be mechanically stable for a user of up to 90 kg, must be able to detect terrain and increase the MTC and stance phase stability over a commercial ESAR prosthetic foot. In the coming sections, the system-level design of the prosthetic ankle will be done to answer some important design questions.

3.3 High level topology considerations

In this section, according to the requirements outlined previously, suitable actuator and sensor topologies will be chosen, keeping cost-effectiveness in mind. For the outlined requirements in Section 3.2, the actuation system must be able to provide toe clearance during the swing phase and mechanical stability during the stance phase. Referring to the solutions discussed in Section 2.4, two different actuation modalities are typically found in prosthetic ankles aiming to solve a similar problem. Namely, these actuation modalities are typically either semi-active hydraulic or electromechanical in nature. The different advantages of each will be discussed at length in the following sections.

Hydraulic spring damper systems, whether passive, can be configured to provide an increase in MTC by the addition of a return spring to return the unloaded foot to the maximum dorsiflexed position. However, this is not position-controllable without the addition of a pump to allow fine control of the ankle angle during the stance phase. Nevertheless, the addition of a pump increases design complexity, and since the pump would not be able to provide sufficient power to propel the user forward, it would be similar to an electromechanical system. Therefore, the only hydraulic system modality that could be used for this specific design criterion would be passive or semi-active hydraulic systems.

Hydraulic systems provide very good mechanical stability during the stance phase, as hydraulic systems allow for controllable loaded dorsiflexion, which can be made similar to the response of a natural ankle during the stance phase, as discussed in Section 2.4. Therefore, provided that the ankle would have a similar ROM as a natural ankle, a hydraulic actuator would be a suitable choice. One of the few drawbacks to the hydraulic actuation systems for prosthetic ankles are that they must be machined within tight tolerances, such that the fluid does not leak out of the cylinder or past the piston inside the cylinder itself. This means the cylinders are more expensive to manufacture in comparison to an electromechanical system. The mechanical impedance of such a hydraulic damping system must be variable for different user weights and different terrains, as the problem outline states. The modelling of the internal dynamics of such a hydraulic system is more involved than that of an electromechanical system, as the damping coefficient is nonlinear and depends on the velocity of the fluid through the adjustable flow valve. Passive hydraulic ankle systems also have the advantage of being more robust, as a passive hydraulic system is inherently waterproof. The addition of control valves and control circuitry can further be made waterproof with the right treatment, such as a resin coating.

In comparison to hydraulic prosthetic ankle systems, an electromechanical solution is cheaper to manufacture, as motors and other hardware can be sourced from a supplier. Rather than having to machine custom valves to fit a custom motor and position feedback system for fine control of the damping coefficient during the gait cycle. However, electromechanical solutions fall short in terms of robustness, as a motor may prove more difficult to waterproof if the motor is used to control the ankle position or other physical parameters. However, this is not impossible and can still be done by enclosing the motor housing and adding gaskets and tight tolerances to a gearbox that will connect the motor to the desired task to be performed. An electromechanical solution also allows for fine control more easily by virtue of the system being more linear in general, with minor linearisations needed. However, there are still parts that must be machined where tolerances are important, such as in the joints of the prosthetic ankle. Backlash in the joints is undesirable, as it decreases the resolution or the effectiveness of the control, because the system will behave in a mode which it was not designed to operate.

Therefore, to summarise the points made previously, a decision matrix is constructed to be able to make an unbiased decision on which mechanical design modality will be best suited for this application. The decision matrix is seen in Table 3.1, weighing the different strengths and weaknesses and assigning a weight out of ten points for each category. After summation of the points assigned to each category for both mechanical design modalities, an electromechanical system was decided to be the most suitable for this application.

Table 3.1: Decision matrix of mechanical design modalities

	Effectiveness	Robustness	Controllability	System mass	Cost-effectiveness	Total
Electromechanical	8	4	9	6	8	**35**
Hydraulic	8	6	6	8	5	**33**

Now that a suitable topology has been selected, system design is to be done to create a system outline, which can be used as a roadmap for the detail design process. The system design will be done in more detail in the sections to come, however the detail design will be covered in Chapter 4.

3.4 High level system design

Now that a basic high-level design decision has been made that determines the type of system and the design principles to be considered when designing such a system. System-level design can be done in order to determine the subsystems and what topology is best suited for each subsystem, such that the system as a whole may be a suitable solution to the problem outlined in Section 1.2.

The system outline as shown in Figure 3.1. From the outline as adapted from literature, it can be seen that there are three different required subsystems for the system to function as desired. Namely, a mechanical structure and movement mechanism, an electrical driver system and a sensor system to detect the user intent.

The mechanical subsystem has two different design requirements: firstly, mechanical stability during the stance phase, and secondly swing phase mechanical actuation during the swing phase. To achieve mechanical stability, as discussed in Section 3.2 the ankle must be able to withstand a maximum torque of 1.5 Nm/kg. Axially, the maximum force the ankle must withstand during heel strike is equal to 1.2$\times$ the user's body weight, as seen in Figure 3.2. As the ankle will be designed for a maximum user weight of 90 kg, the mechanism must be sturdy and capable of withstanding the maximum force profile. As well as being able to withstand these forces, the system should not actuate when the system is in swing phase. This is because, this could result in instability of the user, which could cause the user to fall.

The system should then remain either stationary or in a state which the user can control during the swing phase. Thus, the mechanism should be either non-back drivable or the motor should be used to create a breaking force during the swing phase. Such a braking force could be done with a regenerative braking system, or simply an electrical brake that dumps power into a resistor bank. Such a system could create a damping like effect, however, both of these systems require a larger motor which would increase the total mass of the system. A non-back drivable system could be made lightweight and cost-effective, such as some of the solutions discussed in Section 2.4. Therefore, while an electromechanical braking system to provide a controlled dorsiflexion may be an interesting idea, it does not fit the problem outline as well as a non-back driveable mechanical mechanism driven by a motor during the swing phase.

The electrical subsystem must then consist of a way of driving the motor that controls the mechanical subsystem, as well as providing a stable and safe power supply to protect the motor and other electronics. The motor driver system will depend on the type of motor chosen and will be designed to drive the motor accurately and with a maximum range of variability to allow for fine control. Since the chosen mechanical subsystem will entail a non-back drivable mechanism, the motor requirements drastically decrease, as the motor's only task is to drive the mechanical subsystem at a high speed during the swing phase. This will make sure the motor, the motor driver circuitry and the power regulation can have a small form factor. A small form factor makes the use of the device more accessible to amputees, as a smaller prosthetic ankle form factor means that it can be used with a variety of different prosthetic knees and amputees with different residual leg lengths.

The sensor subsystem must be used to detect the user's intent, as discussed in Section 2.5. Therefore, it must be decided whether the sensor system will be exteroceptive or proprioceptive. Exteroceptive systems allow for a higher prediction time, as these sensor systems can see and detect changes in terrain before the system experiences it. However, in contrast, proprioceptive sensor systems must first experience the change in terrain before it can react to the previous step. Therefore, in regard to function, exteroceptive sensors are definitively superior. However, all exteroceptive sensory systems require a "line of sight" between the sensor and the terrain. If this "line of sight" were to be obstructed by clothing or the other limb, for example, it would cause incorrect measurement of the terrain. Furthermore, many exteroceptive systems make use of an external wearable device, this may be cumbersome to a user as the simplicity of use for any assistive device is critical. Further, the complexity of exteroceptive sensors require a much more powerful processor than proprioceptive sensors. This is because, many exteroceptive systems, such as imaging technology systems store much more data as the image resolution is much more than the data resolution of an IMU for example. Therefore, a decision matrix is constructed to choose between proprioceptive and exteroceptive sensor systems as shown in Table 3.2 below.

Table 3.2: Sensor decision matrix

	Effectiveness	Robustness	Complexity	Cost-effectivene	Total
Proprioceptive	6	8	7	6	**27**
Exteroceptive	9	4	4	4	**21**

As seen in Table 3.2 proprioceptive sensors are better suited to this application than exteroceptive sensors, as the system is more computationally lightweight. This means that the system can be run with a microcontroller, as opposed to a single-board computer (SBC) as frequently seen in literature when using exteroceptive control. It is probably possible to run exteroceptive classification systems on a microcontroller if the system is optimised for computational efficiency; however, this would require more time and is unrealistic to finish within the two-year time frame.

Now that the high-level subsystems have been identified, the subsystems can be designed on a system level. This will be done in the following sections.

3.4.1 Mechanical subsystem system design

As previously discussed, the mechanical system most suited for this specific problem, is a non-back drivable mechanism, that allows for position control of the ankle, while being mechanically stable. This narrows the mechanical subsystem to fall into one of several different categorised solution.

One such solution is a cam-based transmission system as discussed in Section 2.4 as implemented by Lenzi et al [33]. Such a cam based transmission is interesting, because of the small form factor of the system. Such a system would provide a solution to the problem outlined in Section 1.2. However, as such a cam-based transmission essentially creates a rotation about the two surface contacts of the cam and follower. The smooth operation of such a system may then depend on several factors, such as lubrication of the cam and follower surfaces, and the fact that the surfaces of the cam and follower must remain smooth for proper operation. This means factors such as corrosion or deformation due to shock loads will cause such a system to function incorrectly. This means the material selection and hardness of the cam and follower is of critical importance in long-term operation. Therefore, it may be expensive to machine, as the parts may need to be hardened and must be made out of corrosion-resistant material. However, they may not need to be corrosion-resistant if lubricants are constantly applied.

Other systems aiming to achieve a similar outcome, utilise a worm gear transmission system. Such a transmission system uses the friction between the gear surfaces to create a non-back drivable mechanism. This however has the disadvantage that the mechanism is inherently inefficient, as the friction acts against the input motion as well. Another drawback of such a system is that the interaction between the large gear and the worm gear can get jammed with clothing or soil. This effect can be negated by covering the interacting gear faces. However, because of the range of motion being governed by the circumference of the circular gear that is interacted with, by the worm gear the circular gear must be quite large. However, this will cause the transmission system to be heavier. Additional considerations with such a system are that the gears will have to be custom-made, meaning the material consideration is important, as hardness and corrosion resistance are necessary to withstand shock loads. This will cause the machining to be more expensive, as the hardness and tolerances of the gear profile is important.

Lastly, other systems as discussed in Section 2.4, utilise a linkage system with one link being a ball or lead screw to shorten or lengthen that link, such as the system used by Yuan et al. [43]. As ball screws and nuts can be bought off the shelf and do not need to be custom machined, such a system can be manufactured cost-effectively. Such a system is also subject to jamming of the screw and nut interface. However, it would be less likely to jam from clothing, but would still jam from fine debris, such as soil. As the contact between the screw and nut distributes the force applied along a large surface, the system may be more resilient to shock loads than cam-based systems or worm gear systems. Additionally, in the event that damage were to occur to the mechanism, since the parts are commercially available, the part can simply be exchanged without needing to manufacture a new custom part.

Now that the different mechanical mechanisms have been discussed, a decision matrix is set up to choose the most appropriate solution to the problem. The decision matrix is shown in Table 3.3 below. All three systems are assumed to be equally effective and mechanical backlash is assumed to be equal. Further, the robustness, mass and cost-effectiveness of each system is weighted based on the discussion above.

Table 3.3: Mechanism decision matrix

	Effectiveness	Robustness	System mass	Cost-effectivene	Total
Cam-based system	8	6	9	6	**29**
Worm gear system	8	5	5	6	**24**
Linkage system	8	7	7	8	**30**

The most suitable mechanism for the task at hand is the linkage mechanism, as shown in Table 3.3, after analysing the characteristics of each mechanism. The specific design of the linkage mechanism, the number of links and the distance between the links will be designed in the detail design chapter.

3.4.2 Sensor subsystem system level design

The sensor subsystem is required to detect the user's intent during the gait cycle, as well as the terrain being traversed. Therefore, there are two important design objectives that must be handled by the sensor subsystem. Firstly, the sensor system must detect the state in which the device is being operated, if the user is using the device to provide stability and if the device is in the swing phase. This means the system needs a way of detecting a loading condition.

Additionally, the system needs a way of classifying terrain. This can be done by the methods discussed in Section 2.5, as it was decided to use proprioceptive sensors in Section 3.4, due to the cost-effective and robustness of such a system at the cost of performance. Therefore, the sensing technique chosen will impact the classification technique chosen and will determine whether data from literature can be used to build such a classification technique.

Referring back to the techniques outlined in Section 2.5, fuzzy logic or LDA was commonly used to classify or calculate the terrain when proprioceptive sensors are used. This means that the sensors chosen must indicate some statistical change in terrain, meaning that some variable must be measured that changes with terrain. Yuan et al used the shank angle measurement at different gait events as variables to classify between a range of different terrains and achieved an accuracy of 97%. This may prove to be an elegant solution as no external measurement system is needed, which decreases the usage complexity. However, such a system would need to be made resilient to measurement inaccuracies due to shock, which is a characteristic of angle measurements taken from an accelerometer. Angular data can also be taken by integrating the angular speed from a gyroscope, however this angular speed may have a steady state error. This creates a measurement drift when integrating the signal, because this error will be compounded by the integration. However, the shortcomings of both these angular data sensing techniques can be negated by combining the advantages of both the accelerometer and gyroscope angular sensing techniques. Sensor fusion allows for the calculation of an accurate angle measurement by combining the accelerometer and gyroscope sensor data, supplementing the shortcomings of one sensor with the strengths of the other sensor. As these effects are well understood and sensor fusion techniques are commonplace when orientation measurement is required, IMU packages containing both an accelerometer and gyroscope can be cost-effectively sourced commercially. Therefore, to summarise, the shank angle can be measured using a single sensor package, with more computational complexity required for the filtering and calculation of the sensor data.

Other systems make use of EMG sensors to measure the muscle activation of the residual limb to detect changes in walking modes. However, such a sensor modality requires electrodes to be stuck onto the residual limb. This may increase the usage complexity, if the user changes the position of the electrodes from usage to usage, the system may detect different muscle activation. Which would cause the system to incorrectly classify the terrain and possibly usage state. This may cause instability for the user, as the usage state must be reliably correctly classified, otherwise instability can be created in the stance phase. Other systems also use EMG sensors on the healthy leg to classify the terrain being traversed; however, additional wearable sensors are undesirable for this application, as the system complexity from the user's perspective should be kept low. In terms of computational complexity, the EMG sensor signals must first be amplified and then statistically analysed. As such a prosthetic ankle system can be used by both transtibial and transfemoral amputees, the muscles that should be measured should remain consistent between both groups. For this reason, the hamstring and quadriceps muscle activation should be measured. Therefore, a harness could be used to mount the electrodes to the muscles in question. In terms of cost effectiveness, EMG sensors are typically more expensive than IMU, as electrodes, signal amplification and a wiring harness would be required for such a system to function correctly. Capacitive sensors are in principle very similar to the EMG sensors, in terms of mounting complexity and cost.

Since the system will be tested on a test bench, if the system would use EMG sensors to classify gait events, user intents and terrain, such signals would need to be provided externally. This is considered to be suboptimal, as the data would need to be collected and the walking dynamics would need to be recreated by the test bench. Therefore, capacitive sensors and IMUs are a more suitable choice for this specific application. However, since capacitive sensor systems also need a harness to fasten the sensors to the test bench, capacitive sensor systems are less robust than IMUs. For this reason, as well as the fact that open source leg kinematics at different walking speeds and different terrains were found that can be used to model and classify the terrain according to the leg angle at different terrains. Such a dataset was not found for capacitive sensor systems and so IMU systems are most suited for this specific application.

However, IMU systems would not provide reliable gait phase estimation, as the leg angles during the gait cycle are cyclical. Therefore, another type of sensor measurement is needed. An obvious choice would be some type of ground reaction force (GRF) measurement, as such a sensor measurement would allow for detection of gait events as seen in Figure 3.2. To achieve this, an instrumented load cell can be constructed as done by Gabert and Lenzi [47]. However, such a solution, while elegant, makes use of a mechanical system designed specifically for the purpose of measuring the GRF. This makes it attractive as the modularity means it can be used with any prosthetic to measure the GRF, which would make it possible to change the prosthetic ankle prototype completely while keeping the GRF measurement unit. However, while elegant, such a system is still decently complex and the intricacy of such a system means that more time will be spent on the sensor system than is necessary. Another alternative would be to use a load-bearing mechanical structure and attach strain gauges to measure the force placed on the prosthetic. However, the mechanical part to be used to measure the force placed on the prosthetic must undergo a measurable strain when a force is placed upon the prosthetic. Therefore, the mechanical component would be best suited for this purpose would be a cantilever system. A mechanical cantilever that will be used in the prosthetic ankle that could be used for such a purpose is the carbon foot blades.

This can be done as the carbon blades are cantilever systems that are used to store energy during the stance phase, which means the blades undergo measurable and linear deflection. However, since the blade design is outside of the scope of the project, the blades are sourced from an existing prosthetic ankle. Therefore, the sourced carbon blades will play a role in designing the mechanical structure around the carbon blades. The strain gauges could then be placed on the carbon blades to measure the GRF during the gait cycle. Additionally, because the carbon blades sourced from an existing prosthetic ankle include a heel and a toe blade, the GRF of the heel blade and toe blade can be measured independently.

Therefore, in summary, the sensor subsystem design includes an IMU to measure the shank angle and strain gauges placed on the carbon blades to measure the GRF. This allows for two important different measurement metrics, the measurement of the orientation of the prosthetic in real time and the measurement of the force placed on the prosthetic ankle.

This allows for enough information of the interaction of the prosthetic and the terrain to both estimate the user's intent and classify the terrain being traversed.

3.4.3 Electrical subsystem system level design

The electrical system will consist of a power source, to supply power to the electrical motor and control electronics with power, motor driver system to control the motor speed within a large range of controllability and a power regulation and protection system for the motor driver and motor as well as the electronics. As well as power electronics there must be control electronics, such as a microcontroller to analyse and interpret the sensor signals and classify the terrain in real time, the communication protocols between the microcontroller and the sensor systems and the interface between the microcontroller and motor driver circuitry.

As discussed in Section 3.4.2, an IMU and strain gauge system is needed to properly estimate the gait events as well as classify the terrain. Therefore, the interface between the microcontroller and sensor systems depends on the specific components and integrated circuits chosen to perform these tasks.

The power supply to the prosthetic ankle system should be of high enough voltage to allow for a motor of sufficient power to actuate the mechanical system. As well as a high enough capacity to power the system for a significant amount of time. A sufficient operating duration is decided to be eight hours, as the time of use for an individual with a mostly sedentary occupation would not exceed eight hours during a typical day. Therefore, a power supply is needed to supply power to the prosthetic ankle for an eight-hour period, this requirement will serve as a design parameter in choosing the battery topology and specific battery to be best suited for this application.

The power regulation system will have two important roles, the first being to regulate the voltage to the rated voltage of the chosen motor, the second to prevent the motor from being damaged in the event of a rotor blockage. Additionally, the system should prevent potential damage to the battery due to an over discharge scenario, such a scenario could occur from a faulty connection, water bridging the circuitry or user error. However, if such an event were to occur, the battery must remain unharmed and should be able to return to normal operation once such a faulty scenario is removed.

The motor driver topology system will depend on the motor that will be used, as this will determine the specific design criteria. However, the motor will need to be capable of fine control of the motor, such that the system can be controlled accurately to achieve the needed MTC. However, the motor driver will receive input from the microcontroller at a high enough sampling frequency to achieve positional control of the ankle system. Additionally, the switching frequency of the motor is important, as the quieter the system can run, the more natural the system will seem to a user. Therefore, the switching frequency will be set outside the human audible range of ± 20kHz.

Therefore, the electrical subsystem outline with the different interaction interfaces is shown in Figure 3.3, as discussed previously in this section. Further design of the electrical subsystem will be done in Chapter 4.

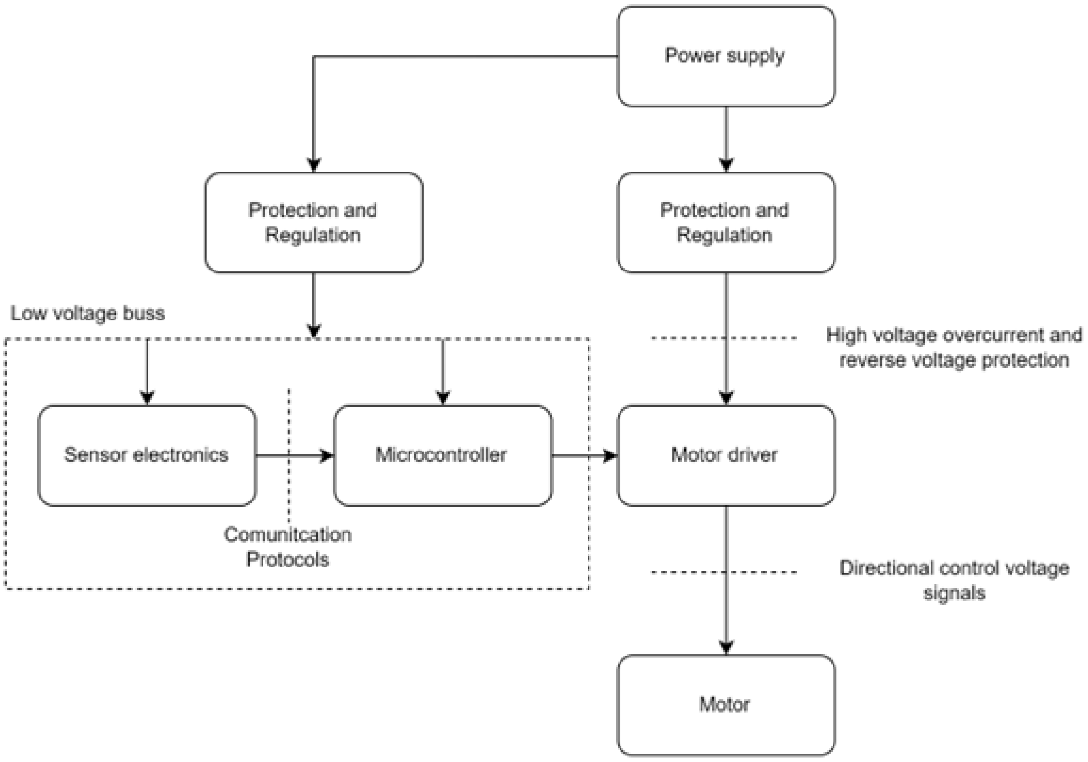

Figure 3.3: Electrical subsystem architecture

3.5 Summary of the system level design

In summary of the system-level design of the prosthetic ankle, after considering the design requirements, the mechanical, electrical, and sensor subsystems were outlined and appropriate topologies were chosen for each of these subsystems. For the mechanical subsystem, a non-back drivable linkage mechanism was chosen to be driven by a small motor and actuated by either a lead or ball screw. The electrical subsystem architecture was outlined that can be used as a for the detail design in Chapter 4. Lastly, the sensor subsystem was chosen to fit the specific needs of gait event detection and real-time parameter measurement for terrain classification. In the coming chapter, the detail design of the prosthetic ankle system will be done, using the design parameters and system design done in this chapter to realise a solution to the problem outlined in Section 1.2.

Chapter 4

Detail design and modelling

4.1 Introduction

This chapter will discuss the detail design process of the different subsystems as outlined in Chapter 3. Firstly, the mechanical subsystem design will be discussed, as the mechanical subsystem is needed in order to model the system and design a closed-loop control system. Secondly, the electrical subsystem will be designed along with the sensors subsystem, as the physical implementation of both of these subsystems are electronic, meaning the design of these subsystems will be done simultaneously. Finally, the closed loop control, finite state machine and real time terrain classification systems will be designed based on data found in literature, as the collection of data for terrain classification outside the scope of this project. This is because the time required to receive ethical clearance to record data from individuals walking on different terrains at different walking speeds may hinder the development of the project itself.

4.2 Mechanical subsystem detail design

As discussed in Section 3.4.1, a non-back drivable linkage mechanism actuated by a lead or ball screw is the most suited for this specific application. However, the linkage mechanism is only a part of the mechanical subsystem, as the mechanical subsystem consists of the actual carbon blades, to interface with the terrain, the linkage mechanism, to achieve an increased MTC and a transmission system to transform the motor output to a linkage motion output.

Figure 4.1 below shows the mechanical subsystem architecture. This outline is derived from the design requirements specified in Section 3.4.1. The mechanical subsystem needs to support the user in the stance phase, act as a moving mechanism during the swing phase, in order to increase the MTC of the user.

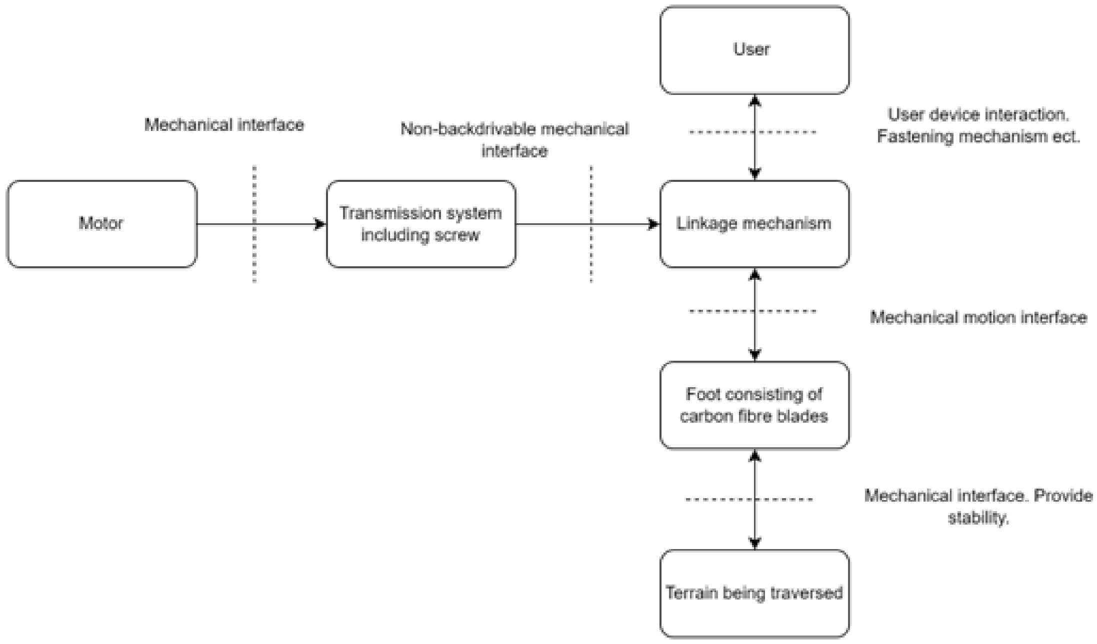

Figure 4.1: Mechanical subsystem architecture

From Figure 4.1 it can be seen that the mechanical design of the prosthetic ankle system depends on the interaction between the motor, transmission system and linkage system as well as the interaction between the terrain, the prosthetic foot and the user. From the user's perspective, even if the prosthetic ankle were incapable of actuation, in the event of a power failure, providing energy storage and return functionality to the user. This functionality is also required during the stance phase, when the prosthetic ankle will cease actuation to provide support for the user.

According to the design requirements outlined in Section 3.2, the mechanical structure of the prosthetic ankle must be able to withstand a maximum torque during operation of 1.5 Nm/kg for a 90 kg user. Therefore, the linkage mechanism will be made to withstand this force as the user will need to exert this force through the linkage mechanism. However, this does not mean that the transmission system will need to withstand such a force, as the screw and nut interface will be used to create the interface between the transmission and the linkage mechanism. This will create the non-back drivable effect, while being a load-bearing member in the system.

To design the mechanical subsystem, first the linkage mechanism will be designed, as the linkage mechanism governs the behaviour of the prosthetic ankle. The linkage system will be designed in concept and later the conceptual parameters will be filled in with detail designed elements.

4.2.1 Linkage mechanism conceptual design

As the linkage mechanism can be seen as the defining mechanical structure of the mechanical subsystem, the linkage mechanism will be designed first. This is done by considering the different linkage mechanisms using a lead or ball screw system available in literature and commercially. Most such prosthetic ankles make use of a four-bar mechanism, with the lead or ball screw acting as a bar in the mechanism; examples include the commercially available Propriofoot, as well as the prosthetic ankle designed by Yuan et al. [43], as discussed in Section 2.4.

The four-bar linkage system will be modelled with inspiration taken from the natural foot-ankle complex, where a tendon shortens and lengthens to induce motion in the ankle. This motion will be replicated with the screw and nut interface acting as the tendon, which shortens and lengthens to provide an output motion about a single ankle joint. This system was then modelled in Microsoft Office 365 Excel, creating a tool for the high-level design of the linkage system. Figure 4.2 shows the output of the model of the linkage system in the Cartesian plane. The x and y axes are the Cartesian coordinates of the ankle system in millimetres, with the ankle joint at the origin.

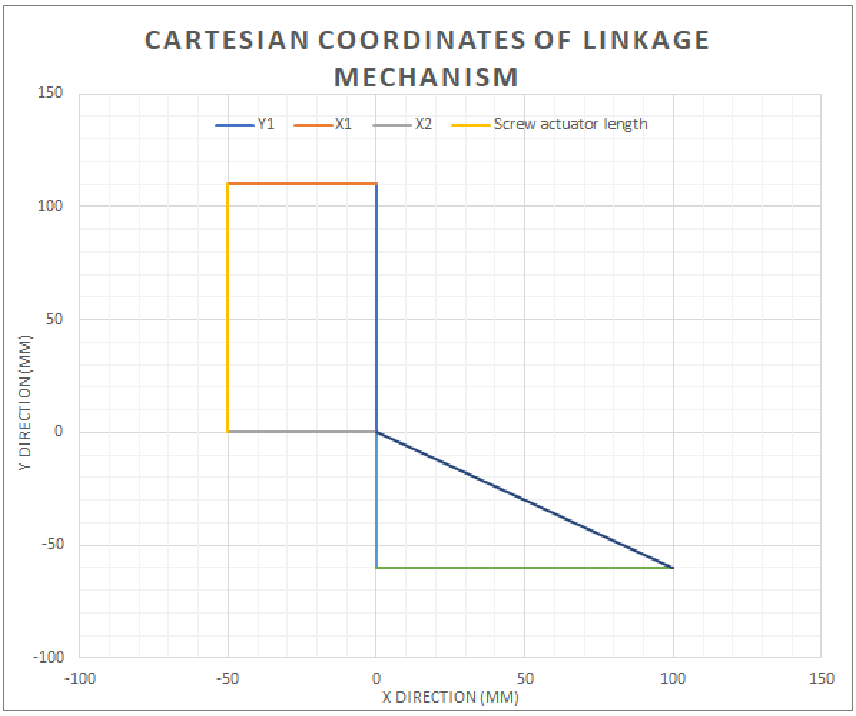

Figure 4.2: Linkage mechanism Cartesian model

This tool is built with the following assumptions: the ankle joint is kept about the origin, and the height of the linkage system from the attachment point to the ankle joint is set by Y1, as seen in Figure 4.2. Y1 should remain small, as a smaller build height of the overall prosthetic ankle is preferred. This is because, a smaller build height makes the prosthetic ankle accessible to a larger amount of amputees. The triangular structure beneath the four-bar mechanism represents the flexible foot blades. The maximum prosthetic ankle ROM is chosen as 40 degrees, with 20 degrees of dorsiflexion and 20 degrees of plantar flexion.

With the design requirements of the ROM and the load requirements, the model is constructed using basic trigonometry and allows for the varying each of the link lengths. The two basic design parameters that would influence the dynamics and load profile of the system are the build height, denoted by Y1 and the distance between the ankle joint and the screw actuator, denoted by X2. X1 denotes the top link of the four-bar mechanism and remains stationary during the entire range of motion. For symmetry, X1 and X2 are set equal to one another. As mentioned previously, the build height should be small in order to fit the widest range of amputees, therefore, 110 mm was selected as a suitable parameter for Y1. However, varying X1 would change not only the force on the screw, but also the linear speed necessary to achieve 100°/s. Figure 4.3 shows the effect of varying the parameter X1 of the dynamics of the system.

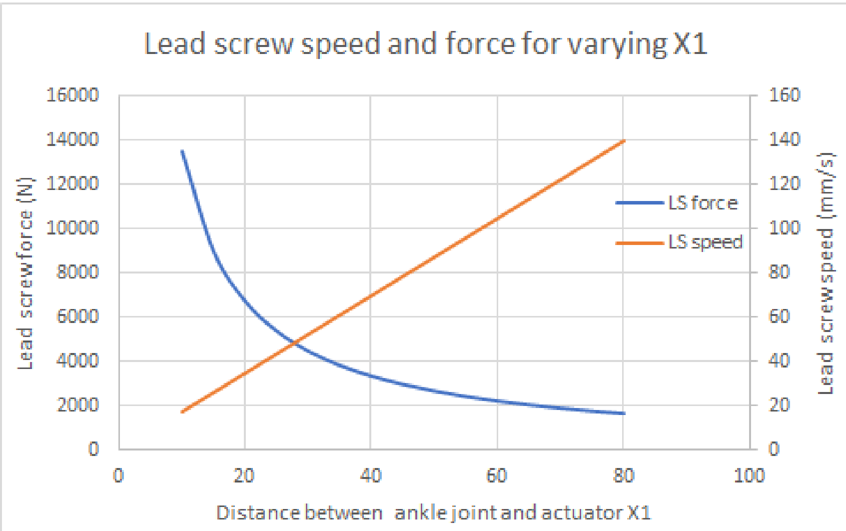

Figure 4.3: Lead screw speed and force, when varying X1

The parameter of X1 must be selected, such that the speed of the screw system must be realistic, to keep vibration to an acceptable limit as well as minimising the force on the lead screw. From Figure 4.3 it can be seen that the distance parameter X1 should be between 30 and 50 mm to minimise the force exerted on the screw component while keeping the required speed from the motor at an acceptable limit. A distance of 50 mm was chosen for X1, because of the fact that commercially available lead screws with a smaller diameter are more cost effective and therefore, a greater distance of X1 is favourable in this regard.

Now that the basic outline of the linkage mechanism is decided upon, the screw system must be conceptually designed. As cost-effectiveness is a key point of interest for this study, a lead screw system will be used. This comes at the cost of increased backlash between the lead screw and the nut and subsequently increased vibration. Due to the availability of 3D printers, 8 mm diameter 310 stainless steel lead screws have become readily available. The maximum stress experienced by the lead screw at every contact angle in the ROM of the system is calculated by substituting Equation 4.1 into Equation 4.2, assuming the maximum stress is experienced in tension and buckling does not need to be considered due to the length of the screw.

$$F_{LS} = \frac{\frac{\tau_{max}}{X_1 \cos(\theta)}}{\cos(\alpha)} \tag{4.1}$$

Where F_{LS} is the vertical component of the force experienced by the lead screw, θ is the contact angle, τ_{max} is the maximum torque experienced during the gait cycle and α is the angle of the lead screw to the horizontal. Next, the axial stress through the screw can be calculated using the following equation.

$$\sigma_{LS} = \frac{F_{LS}}{\pi \times \frac{D_m}{4}} \tag{4.2}$$

Where D_m is the mean diameter of the lead screw, and σ_{LS} is the maximum axial stress experienced by the lead screw. It is assumed that the lead screw will not experience a bending moment, as the lead screw is part of a linkage mechanism. Using the model shown in Figure 4.2 to calculate the lead screw position at every contact angle, the maximum stress experienced by the lead screw at every contact angle in the ROM of the ankle mechanism was calculated and is shown in Figure 4.4 below.

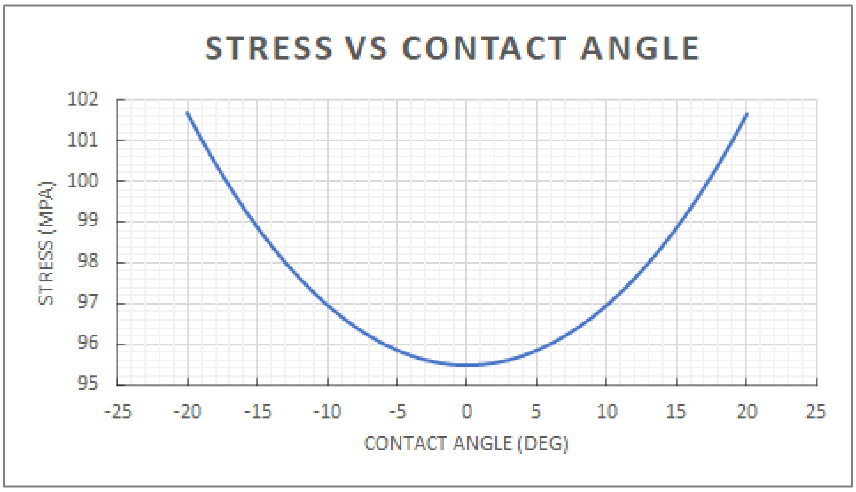

Figure 4.4: Lead screw stress vs contact angle

As the yield stress of 310 stainless steel is about 190 MPa, the maximum stress experienced by the lead screw with an outer diameter of 8 mm is well within the tolerable limit, with a safety factor of 1.86. The next step is to design the foot blade mounting system, such that the transmission system and motor requirements can be specified.

4.2.2 Foot blade mount design

The foot blades were taken from a broken Össur hydraulic ankle and repurposed for the design of this prosthetic ankle system. However, a mounting system is still required to fasten these carbon blades to the prosthetic ankle. The weight of this mounting system will contribute to the motor requirements, as the motor must be able to actuate under the load of the blade mounting system.

Therefore, the geometry of the blades is given, only the mounting must be designed. As the blade mounting must be connected to both the screw and the screw actuator the mounting must be able to fit two different pin joints. The geometry for mounting the blades was taken from the Össur hydraulic ankle; the material was chosen to be aluminium as it is lightweight and corrosion resistance. Figure 4.5 shows the foot blade mount design composing of three different aluminium parts, screwed together using M4 bolts, enabling the foot blade mount to be made out of 20 mm thick aluminium plate.

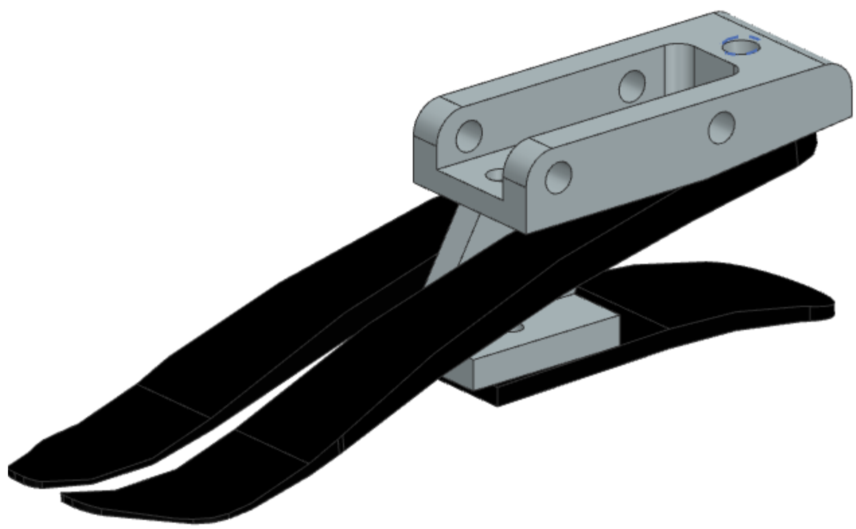

Figure 4.5: Foot blade mount design

Making sure the foot blade mounting system can withstand the force profile of the gait cycle, a finite element analysis (FEA) is done in Siemens NX version 1980. The mount point is constrained as it would be constrained in construction and loaded by the attachment of toe blade and heel blade. Figure 4.6 shows the results of the FEA on the blade mounting system, and it can be seen that the maximum stress in the blade mounting system is found to be 37.25 MPa, where the yield stress of Aluminium 1050 is 103 MPa. This gives a safety factor of 2.76, meaning the mounting system is safe to use for this application.

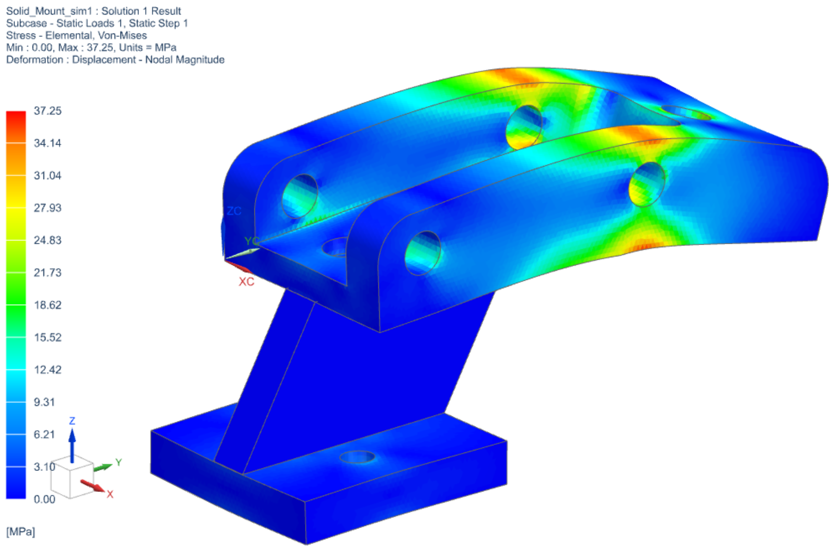

Figure 4.6: Blade mount FEA

Now that the foot blade mount system has been designed, the weight of the foot blade mount system is found to be 915 g. Next, the lead screw transmission system must be designed to conform with the design requirements and the linkage system parameters decided in Section 4.2.1.

4.2.3 Transmission subsystem design

As the lead screw forms part of the transmission system as well as the linkage mechanism, the lead pitch of the lead screw is therefore important, as it must be both non-back drivable and will influence the transmission system and motor requirements. The back drivability of the lead screw is dictated by the friction of the lead screw, as outlined in Equation 4.3 [48].

$$\pi f d_m > l \tag{4.3}$$

Where f is the friction coefficient between the lead screw and the lead nut, d_m is the mean diameter of the lead screw and l is the lead pitch of the screw. The mean diameter is set at 6 mm, and the friction coefficient between the nut and screw is set to be 0.4, meaning the maximum pitch for the lead screw to be non-back-drivable is set to be 7.53 mm. Therefore, the commercially available 2 mm pitch would be non-back drivable and suitable for this application.

The transmission system has the main function of transmitting motor power to the linkage mechanism. The motor power requirements will be specified while designing the transmission system. The required speed of the motor is also determined by the transmission system, based on the required speed of the linkage mechanism. The required linear speed of the lead screw extension and retraction is calculated using the model shown in Figure 4.2, this model is also used to calculate the maximum and minimum length of the lead screw as shown in Figure 4.7 below.

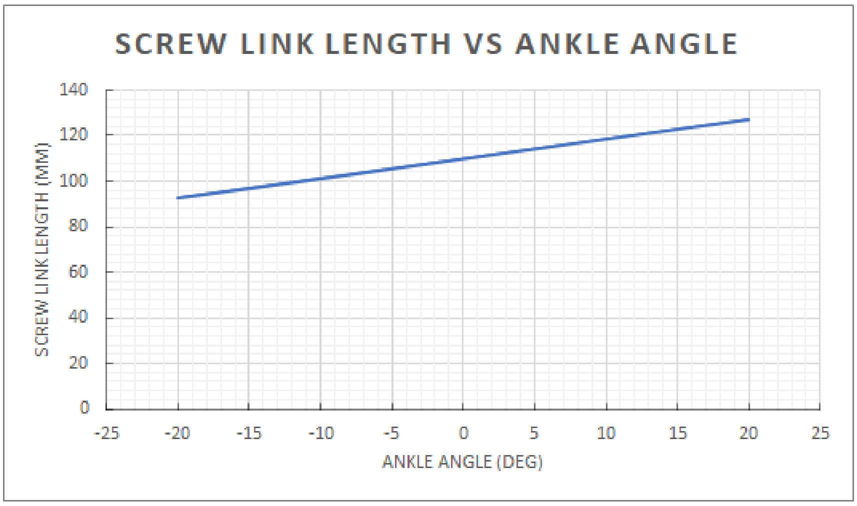

Figure 4.7: Screw link length vs ankle angle

Calculating the linear screw speed using the average slope of the line as shown in Figure 4.7 yields a maximum required linear screw speed of 86.14 mm/s. This can be achieved in a number of ways and the mechanical coupling between the motor and the lead screw can be done either geared or directly. However, a belt and pulley transmission system was decided to be the most suited for this application, because of the inherent vibration damping properties of a belt transmission system. Additionally, there is a relief on mechanical tolerance, as a timing belt and pulley system can run well even when improperly aligned. Additionally, such a belt and pulley transmission helps to keep the motor out of the line of force of the lead screw system, allowing a small motor to be fitted to the system safely. Since the lead screw pitch was chosen to be 2 mm, due to the cost-effectiveness and non-back drivability, the speed of the lead screw to achieve an ankle speed of $100°/s$ can be calculated to be 2584.2 rpm.

The maximum torque required to lift the blade mount system can be calculated using Equation 4.4 [48]. The force on the lead screw can be calculated using the weight of the foot blade mounting system. The torque required to drive the lead screw can be calculated as 24.88 mNm. Therefore, the power required from a motor to drive the lead screw at the required speed can be calculated as 6.73 W.

$$\tau_{max} = \frac{F_l \times d_m}{2}\left(\frac{\pi f d_m - l}{\pi d_m + f l}\right) \tag{4.4}$$

Therefore, the motor power required is 6.73 W, however the transmission system is chosen such that the selected motor can suitably drive the lead screw, within the safe operating range of the motor. Since motors generally have a higher torque ratings at higher voltage ratings and the higher the voltage required of the motor, the higher the voltage of the battery should be. Therefore, a higher voltage motor may increase the weight of the battery, due to the extra cells required to make this voltage. Therefore, a gear ratio of 2:1 was chosen to drive the lead screw, setting the motor requirements at 5168.4 rpm and 12.4413 mNm.

The transmission system is chosen to achieve a motor speed reduction of 2:1, the belt will be chosen from a manufacturer, while the timing pulleys will be designed and 3D printed. This is because the power transmitted through the timing belt and pulley system is only 6.73 W. The belt chosen was a 100 tooth timing belt with a pitch of 2 mm, this means that the belt circumference is 200 mm. Equations 4.5 and 4.6 are used to calculate the angle in which the belt is in contact with the pulley.

$$\theta_d = \pi - 2\sin(\frac{D-d}{2C}) \tag{4.5}$$

Where θ_d is the angle of contact between the small pulley and the belt, D is the diameter of the large pulley, d is the diameter of the small pulley and C is the centre distance between the two pulleys.

$$\theta_D = \pi + 2\sin(\frac{D-d}{2C}) \tag{4.6}$$

In this equation, θ_D is the angle of contact of the large pulley and the belt and the rest of the parameters are the same as previously mentioned. The centred distance between the two pulleys can be calculated by rearranging Equation 4.7 and substituting Equations 4.5 and 4.6 [48].

$$L = \sqrt{4C^2 - (D-d)^2} + \frac{1}{2}(D\theta_D + d\theta_d) \tag{4.7}$$

Rearranging Equation 4.7 yields Equation 4.8 as can be seen below.

$$C = \frac{(L - \frac{\pi(D+d)}{2}) + \sqrt{(L - \frac{\pi(D+d)^2}{2})^2 - 2(D-d)^2}}{4} \tag{4.8}$$

The belt was chosen with 100 teeth, Equations 4.5, 4.6 and 4.8 were used to calculate the centre distance between the two pulleys. The pulley teeth were chosen at 24 and 48 teeth, with a pitch of 2 mm. This means that the centre distance can be calculated from the pulley diameter as 63.54 mm. The choice of the amount of teeth for the pulleys was determined by two factors, the clearance between the two pulleys and the tension on the belt required to properly index with the small pulley. The fewer teeth on the small pulley, the more tension is required to properly index the teeth with the belt, however the larger the pulley becomes, the less clearance exists between the two pulleys. Therefore, the pulley sizes were chosen iteratively through experimentation.

To further design the system, a motor is needed to drive the transmission system. As the motor requirements are already set out, the motor topology must be decided upon to choose a specific motor. In order to reduce the overall system cost and complexity of the driver circuit, a brushed DC motor was chosen. However, the motor must be high quality to ensure a longer life of the motor. The Faulhaber 2237 motor with a rated voltage of 12V was chosen to be well suited for these reasons, as the motor is rated at 11W.

Figure 4.8 below shows the transmission system with the motor and pulleys, as designed to be a link in the four-bar linkage system. The parts being referred to in the following discussion can be seen in Figure 4.8. The lead screw is constrained, by using two thrust bearings and two radial bearings, inside the bearing housing. The bushings are made to fit tightly into the chassis, while the shaft can then fit within the bushing. The nut holder allows the lead screw to interface with the nut, while providing the necessary clearance to decrease the distance between the two shafts. The motor mounting plate is manufactured from laser-cut mild steel, with slots cut so that the bearing housing and lead screw system can be adjusted to apply proper tension on their belt. The lead nut is fixed to the nut holder using four M3 bolts; the stress experienced by the M3 bolts can be calculated as 146.412 MPa, while the bolts are 12.9 high-tensile-strength bolts, with a minimum yield stress of 1220 MPa. The design of the nut holder is constrained by the maximum and minimum length of the lead screw link, as seen in Figure 4.7.

Now that the linkage parameters, transmission parameters and motor requirements have been designed, the mechanical chassis of the prosthetic ankle should be designed. The chassis will function as a load-bearing mounting system for the linkage system and foot blade mount.

4.2.4 Chassis structure design

Now that the linkage mechanism parameters have been set, as well as the lead screw and transmission parameters. As the linkage mechanism must be able to fit the foot blade mounting system as well as the lead screw transmission system. Where the foot blade mounting system acts as one link in the linkage and the lead screw system acts as another link, this means it would be best to fit the lead screw and foot blade mounting system inside a larger chassis. The chassis was manufactured from laser-cut 3 mm hot-rolled AISI 1018 mild steel to achieve a strong, cost-effective chassis. The parameters for the distances

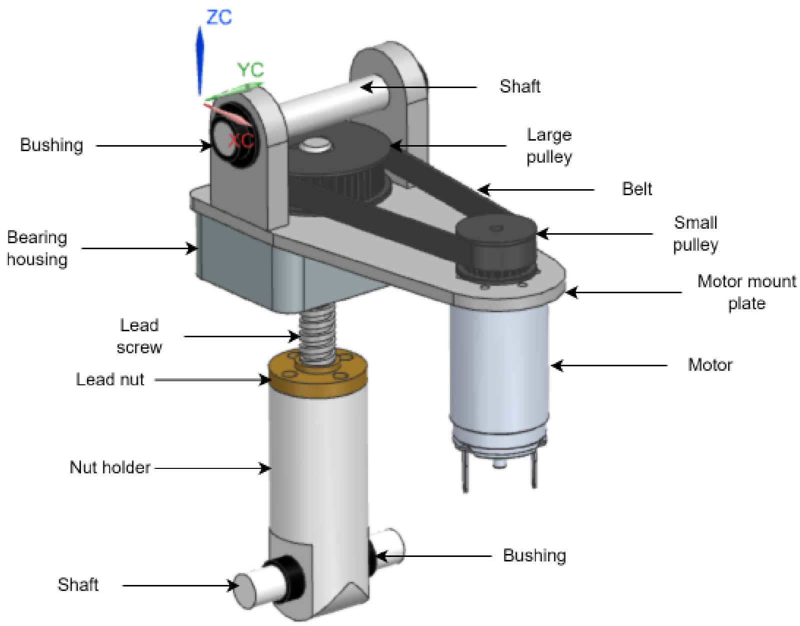

Figure 4.8: Belt and pulley transmission system

between the joints of the chassis are decided upon previously in Section 4.2.1.

The chassis was designed with focus on triangulation between the stationary joints to ensure a strong frame. A FEA was done on the chassis frame, with a mesh distance of 1 mm, and can be seen in Figure 4.9. As it can be seen from Figure 4.9, the maximum stress experienced by the frame is around 77.18 MPa, where the yield stress of mild steel being approximately 200 MPa, giving a safety factor 2.59.

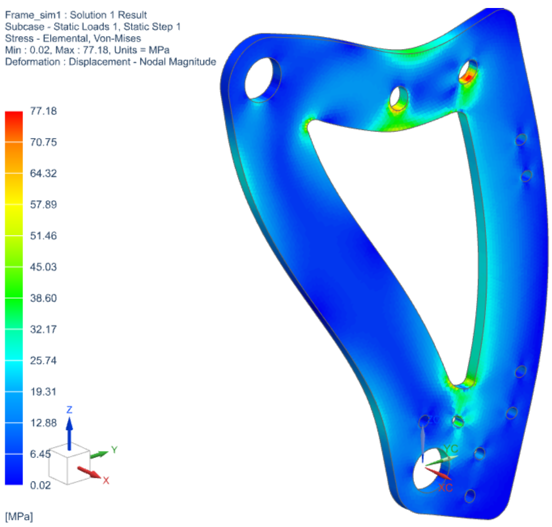

Figure 4.9: Finite element analysis done on the chassis frame

A way of mounting the ankle to a prosthetic leg is also needed, pyramid adapters are typically used to connect prosthetic ankles and feet to prosthetic legs. This allows the prosthetic ankle to be adjusted in the transverse and sagittal planes. This allows the prosthetic to be aligned properly for each individual using the prosthetic for their individual needs. Figure 4.10 below displays the final design for the pyramid adapter, manufactured out of AISI 310 stainless steel, mounted to the chassis through a laser-cut 3 mm mild steel mounting plate. The pyramid adapter is affixed to the mounting plate with four M3 bolts. The pyramid adapter is connected to the chassis, using four M5 bolts, meaning the M5 bolts will bear the load in a shear direction.

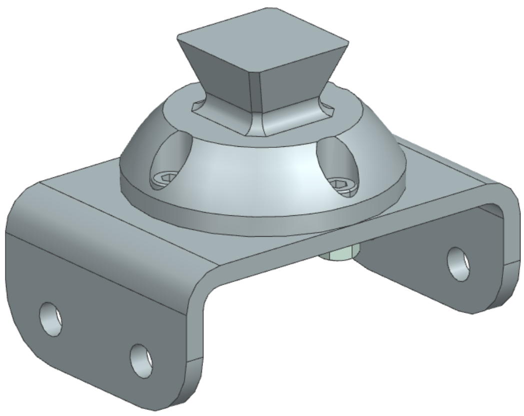

Figure 4.10: Pyramid adapter

Now that the linkage and chassis has been designed, the transmission system must be designed in detail. The ankle chassis with the pyramid mount and frame is shown in Figure 4.11, with the joint shafts being M8 bolts for cost-effectiveness. An additional front mount system designed to constrain the movement of triangular chassis members and to serve as a mount for the electronics that will be designed in the coming sections. Brass bushings are fitted into the laser-cut sheet metal fabricated chassis members, as the tolerance of the holes that are laser-cut is quite low. This allows the system to rotate with less friction around the shaft, while reducing the backlash around the joint. Bushings are more suitable than bearings in this case, as the linkage joints will never make a full rotation about the axis.

Now that the screw link was designed in detail, the total ankle system is shown in Figure 4.12 below. The mechanical system is designed with the design requirements in mind, that being the mechanical stability in the stance phase and the ability to increase the MTC during the swing phase. The mechanical system is stable during the stance phase, since the mechanical parts designed are all strong enough to bear the load placed on them. The MTC can be increased during the swing phase by driving the lead screw system, which is non-back drivable, meaning the lead screw transmission meets the design requirements. The overall system build height is 205 mm from the top of the pyramid adapter to the bottom of the blades.

Figure 4.11: Ankle chassis

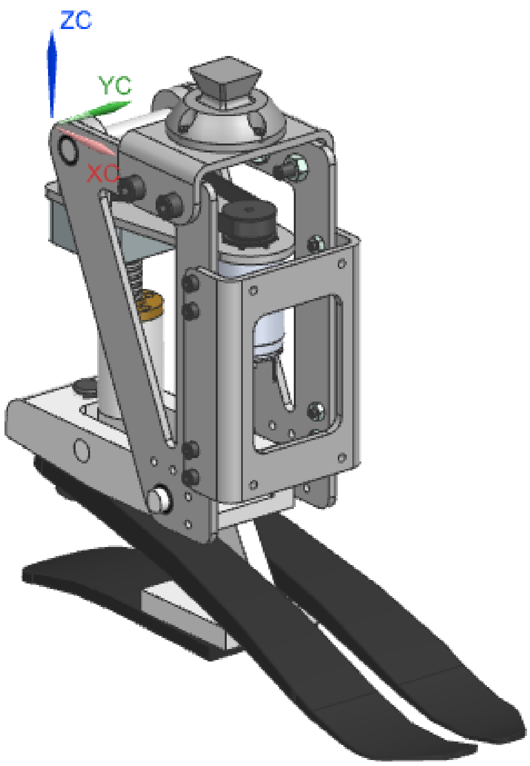

Figure 4.12: Ankle mechanical design

In the following sections, the electronic design of the system will be refined, adding sensors and an electronic driver system, such that the system is capable of proprioception. As well as designing a control system that will govern the system, making use of the proprioceptive sensors to drive the prosthetic ankle system, enabling it to detect terrain being traversed.

4.3 Electrical and electronic system design

The electrical and electronic system is designed to drive the motor with a high degree of speed or position control of the system, as well as regulate power and protect the electronic components. The sensor systems communicate data to a microcontroller, which would then use the data to classify the terrain and detecting the important gait events and drive the system to effectively increase the MTC.

The electrical and electronic system architecture outlined in Figure 3.3 can be refined as seen in Figure 4.13. This refinement in the system architecture is due to the decisions made in Section 3.4.2, such as the choice to use proprioceptive sensors, namely an IMU on the shank and strain gauges to measure force on the blades. However, another sensor is needed to measure the position of the system in order to provide feedback to be able to drive the system to a specified position. Examples from literature include either rotary encoders or potentiometers. Rotary encoders are available in two different topologies, which provide either absolute or relative positional feedback. While potentiometers are absolute by nature, however, require internal contact to vary the resistance of the potentiometer. While rotary encoders can be considered contactless since these encoders do not require internal contact to function, as the magnetic field of a magnet is measured using a Hall effect sensor. Therefore, the rotary encoder system will have a longer lifespan than a potentiometer system. For this reason, rotary encoders are more suitable to this problem than potentiometers. However, the rotary encoder chosen is a relative rotary encoder, as these encoders are more cost-effective than absolute encoders, this does mean that a limit switch is necessary to determine a reference point.

From Figure 4.13 it can be seen that the electrical and electronic system consists of the power regulation system, that must regulate and provide protection on two different voltage levels. The specific voltage levels depend on the components used in the motor driver and sensor subsystems. A motor driver subsystem must be designed to drive the chosen brushed DC motor with a rated voltage of 12V, at a high frequency to avoid additional noise from the motor inductive ringing. The motor driver must be capable of bidirectional control, due to the system requirements.

The low voltage level will be common for the sensor and microcontroller system, depending on the specific components used. The electronic circuit around the IMU depends on the specific recommended circuit, recommended in the datasheet. The rotary encoder circuit will similarly be determined by the datasheet. However, the circuit around the strain gauge system will depend on the voltage difference measured, generated by the deflection

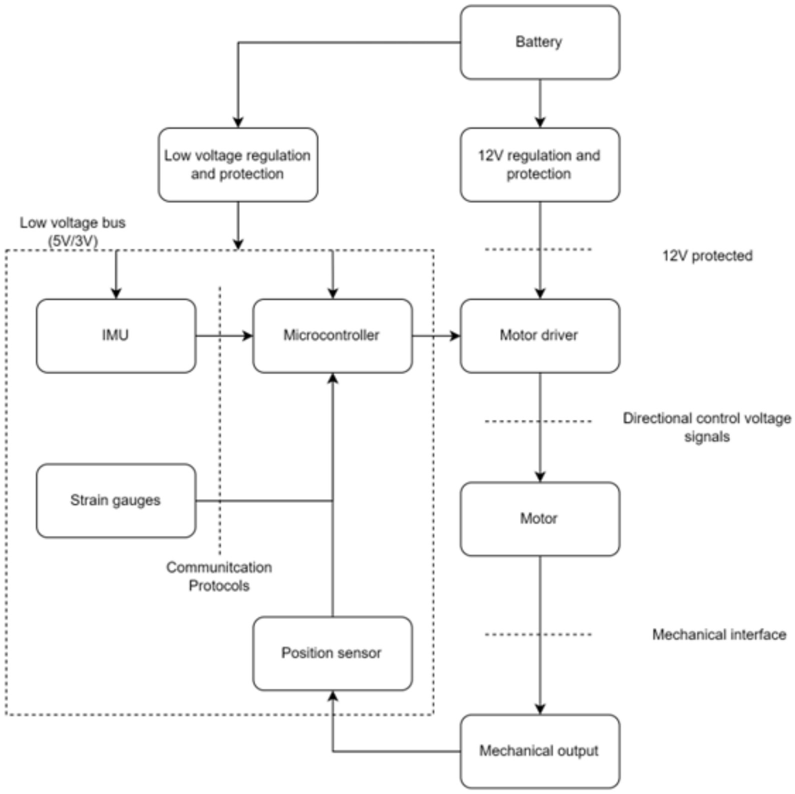

Figure 4.13: Refined electrical system architecture

of the blades. Therefore, the amplification and resolution that will be designed for depends on the blade deflection. To determine this, the strain gauges were first glued to the blade surfaces, and a know weight applied to deflect the blade. Then the change in resistance was measured using a high precision multimeter, this change in resistance was then used to simulate the voltage difference to be measured.

4.3.1 Power regulation subsystem design

However, the first subsystems to be designed that are essential for any level of functionality of the system are the voltage regulation subsystem and the motor driver subsystem. The voltage regulation system topology largely depends on the battery system chosen, as the motor voltage rating is 12V, the battery voltage will either need to be stepped up or down to ensure the motor runs at its rated voltage. The motor driver topology chosen is an H-bridge motor driver topology, as this allows the motor to be driven bidirectionally while allowing fine control of the average voltage across the motor.

Revisiting the motor chosen in Section 4.2, the motor topology was chosen due to the overall cost-effectiveness and simplicity of such a solution in comparison to brushless DC motors. This choice was made at the expense of performance, as the different techniques in driving the motors means that the average voltage across the brushed DC motor is controlled, while the frequency of the 3-phase sinusoidal voltage across the brushless DC motor is controlled in the case of a brushless motor. This allows a unique benefit, where even with a small control signal, the brushless motor will be able to apply full load torque, where the brushed DC motor will only be able to apply full-load torque when the control signal is high.

The motor chosen in Section 4.2 was the Faulhaber 12 V 2237, this motor was chosen due to the motor's relatively high efficiency of 70.8% and small form factor. The motor has an internal resistance of 3.92 Ω and the coil inductance is given as 150 μH. This gives a maximum inrush current of 3.06 A. Because the motor will not be running continuously in this application, rather rotating for short time periods to a specific position, the motor will start from a stationary position quite often. For this reason, the inrush current will be considered as the rated current for the power regulation and motor driver circuit requirements.

The battery system used was taken from a previous project and was 4 cell lithium-ion battery with a weight of 460 g. This places the nominal voltage of the battery at 14.8 V, while the voltage of the battery at full charge is 16.8 V, which is 1.4 times the motor's rated voltage. This should still operate safely, however the voltage regulator serves as a safety mechanism for the battery as well as allows the system to function with different batteries of higher voltage levels.

As the voltage of the battery is higher than the rated voltage of the motor, a step-down topology is needed. To achieve this efficiently, a buck converter voltage regulation topology was chosen, as a buck converter consists of few components is can also be constructed cost-effectively. Therefore, in order to design a voltage regulator circuit to comply to the requirements set out previously, a dedicated integrated circuit (IC) can be used to provide the switching waveforms based on the feedback voltage provided. Most such voltage regulator ICs utilise an internal reference voltage to generate a pulse width modulated (PWM) output square wave voltage. This can either be used to drive an external MOSFET or an internal MOSFET can be switched to create the output waveform, as can be seen in the simplified functional block diagram of such an IC in Figure 4.14. This topology is, however, not common amongst all buck regulator ICs and is also very simplified, as many buck regulator ICs take the inductor current into account as well. Figure 4.14 also neglects any safety features and is included for clarity on the working principle of such an IC.

An IC must therefore be chosen such that a stable voltage can be generated under load and must ideally allow for overcurrent protection and have a hand-solderable form factor, such that it may be assembled by hand. For this reason, the LM3485 from Texas instruments was selected for a suitable regulator IC for this application, as it features a hand-solderable

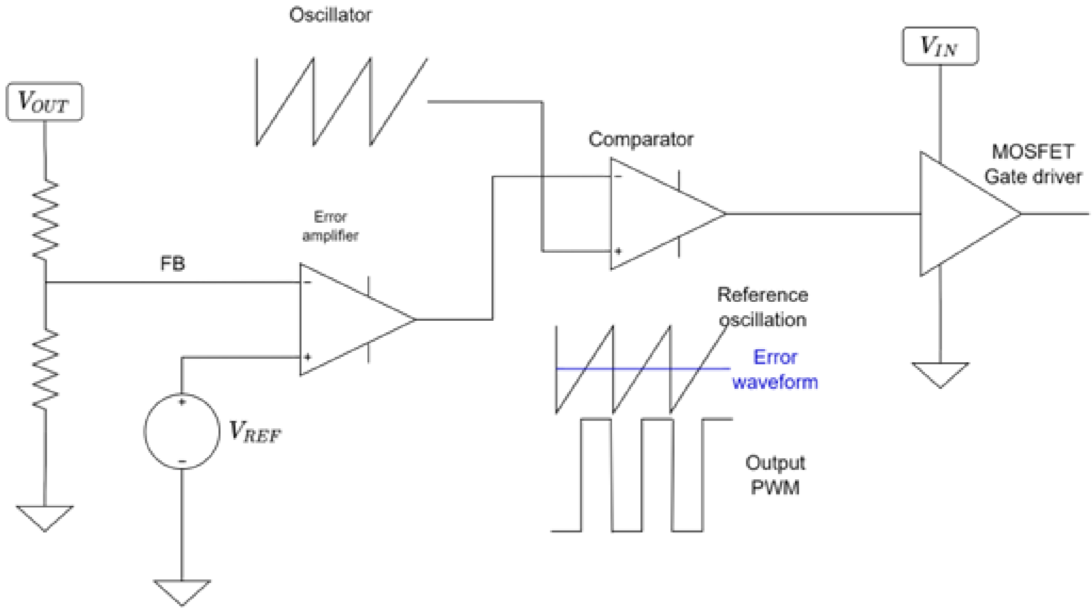

Figure 4.14: Simplified block diagram of buck regulator IC

package and overcurrent protection at a low cost.

According to the datasheet the output voltage can be calculated by Equation 4.9 below, where R_1 and R_2 are the resistors making up the feedback network, and the reference voltage is given as 1.242 V.

$$V_{OUT} = 1.242 \times \frac{(R_1 + R_2)}{R_2} \tag{4.9}$$

The frequency of operation of the buck regulator plays a crucial part in the design of the other passive components in the circuit, according to the datasheet the frequency of operation can be estimated by Equation 4.10. Where V_{HYST} refers to the peak to peak ripple voltage at the feedback pin of the IC, ESR is the parasitic series resistance of the output capacitor, α is a geometric factor and t_d is a propagation delay.

$$F = \frac{V_{OUT}}{V_{IN}} \times \frac{(V_{IN} - V_{OUT}) \times ESR}{(V_{HYST} \times \alpha \times L) + (V_{IN} \times t_d \times ESR)} \tag{4.10}$$

Where the required inductor can be calculated by Equation 4.11, as described by the datasheet. Where, V_D is the diode forward voltage, ΔI is the inductor ripple current, k is the duty cycle and f is the operating frequency.

$$L = \frac{V_{IN} - V_D - V_{OUT}}{\Delta I} \times \frac{k}{f} \tag{4.11}$$

The output capacitor can be calculated using Equation 4.12 as described in the power electronics textbook by Rashid [49]. Where, ΔV_c is the ripple voltage across the output capacitor and load and the other parameters are discussed previously.

$$\Delta V_c = \frac{V_{IN} D(1-D)}{8LCf^2} \tag{4.12}$$

Equations 4.9 through 4.12 are used to calculate the important circuit parameters. The operating frequency was chosen to be 100 kHz, as this is a frequency high enough to be outside the audible range and should be sufficient to achieve good control of the output voltage. The ripple voltage at the output was chosen to be 100 mV and the ripple current was chosen at 0.4 A. With these parameters, the required inductance was calculated using Equation 4.11 as 85.761 μH. The inductance was therefore chosen at 1.2×L as 100 μH to provide a safety factor. The capacitance required is calculated at 4.285 μF, however, the capacitance chosen was 100 μF, due to the decreased ripple voltage and higher capacitance to provide inrush current for the DC motor.

The circuit is simulated as can be seen in Figure 4.15, the circuit was simulated with a capacitive ESR of 35 $m\Omega$ and a simulated white noise of 100 mV. This is done to determine the transfer characteristics of the power converter as well as the ripple voltage and to check the current and voltages through the passive components.

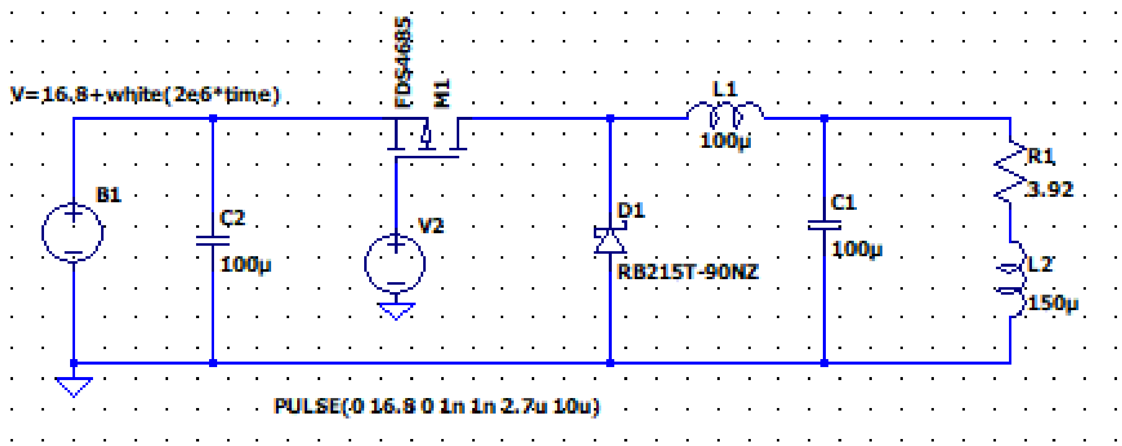

Figure 4.15: Power regulation simulation

Simulating the output voltage of the power regulator yields a output ripple of 16 mV about 12 V, due to the simulated white noise source. This is due to the filtering characteristics of the system, as can be seen from the fast Fourier transform (FFT) as can be seen in Figure 4.16. Figure 4.16 shows the output voltage FFT in blue and the input voltage FFT in green. It can be seen then from Figure 4.16, that the buck converter acts as a low pass filter, with added noise components as harmonics of the switching frequency.

The ripple voltage at the switching frequency of 100 kHz, was calculated and simulated

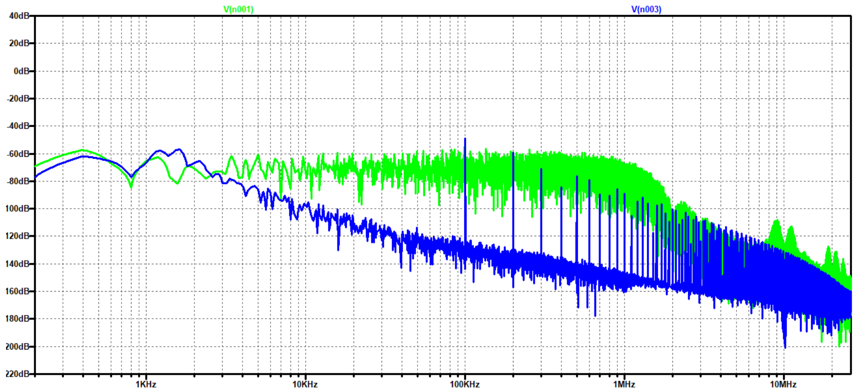

Figure 4.16: Power regulator FFT

to be around 4.12 mV. However, because the simulated source acts similar to a lab bench power supply and injects noise at different frequencies, the noise components at lower frequencies can pass through the filter created by the buck converter, creating an overall higher ripple voltage. When using a battery system however, the input voltage frequency is assumed to be purely DC, meaning no frequency components are expected when using a battery input, which should serve to decrease the output ripple voltage.

The other needed resistors were chosen to create the feedback network required to regulate the output voltage at 12 V while setting the overcurrent protection to 5 A, as the motor inrush current will never reach this. Therefore, if the circuit were to draw 5 A, a fault would exist. As the LM3485 IC is designed to drive a P-channel MOSFET, the NDT452AP was chosen as the threshold voltage was low enough to be driven by the LM3485. Additionally, the current rating of the NDT452AP is 5 A, which allows a safety factor of 1.63 for the MOSFET. The diode chosen was a RB215T-90NZ and was chosen due to the solderable form factor and the recovery time.

The power regulation circuit was then designed to be manufactured on a printed circuit board (PCB), as a the final system must have a small form factor to fit on the prosthetic ankle frame. To achieve this, the capacitor and inductors were chosen with the required passive parameters, as well as the ESR and ripple current ratings in the case of the capacitor. The ripple current required for the capacitor was found in simulation as 324 mA. Therefore, the capacitor and inductors can be chosen based on the requirements, the resistors and ceramic capacitors were chosen to have a package of 1206. Additionally, an LED was connected to the input to visually display that power is connected. An additional P-channel MOSFET is added to the input as reverse voltage protection, to protect both the power regulation and the electronics that will be connected later on. Therefore, due to the fact that the battery housing not being within the mechanical structure, the power regulation system will be separate from the motor driver and low-voltage electronics. Therefore, the PCB will be designed with a 2 layer board due to the relatively low complexity. Important design rules when designing a power regulation system are given in the datasheet and general PCB design practices, as these design rules are made to decrease the electromagnetic interference (EMI) and decrease the heating of the conductors. Therefore, EMI on the feedback line of the LM3485 should be minimised, as this will keep the operating frequency within the required range. Furthermore, this will decrease the ripple current on the output, as the error on the feedback pin of the LM3485 will create an error on the output of the power regulation system. To achieve this, two important techniques can be employed to minimise the EMI on the feedback line. Firstly, the feedback line should be kept away from high sources of alternating current, such as the inductor and output capacitor. Secondly, vias connecting to the ground plane are placed around the feedback line, such that the EMI around the feedback line can be sunk into the ground plane, as this acts as a capacitance between the source of EMI and the ground plane, without intersecting the feedback line. Another important design rule is the keep the distance between the MOSFET drain and the inductor input and the anode of the diode as short as possible, as this conductor carries a large alternating current. Another important design rule is to allow a large ground plane to be uninterrupted underneath the circuit, this allows a capacitance between the ground plane and the current carrying conductors, which helps to decrease the EMI between the components. By employing these design rules, the PCB was designed and is shown in Figure 4.17 below.

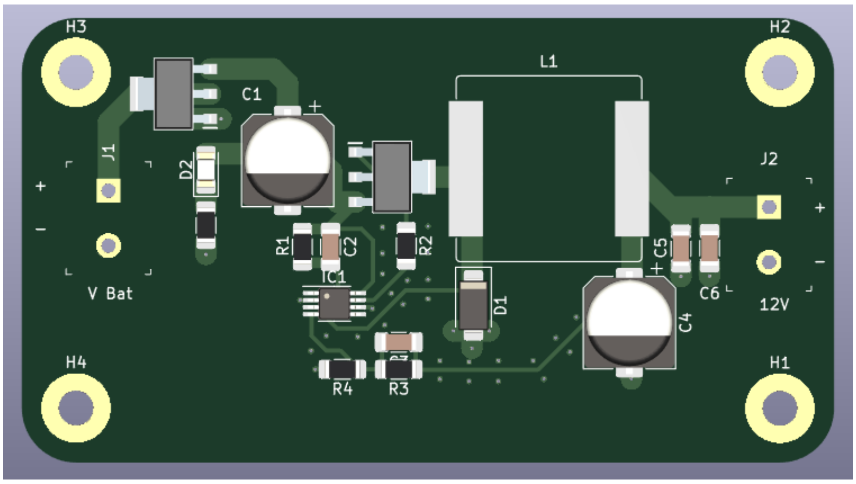

Figure 4.17: Final power regulator PCB

With the power regulation subsystem designed, the motor driver subsystem can be designed, according to Figure 4.13. The requirements for the motor driver subsystem are laid out using to the choice of motor and input power voltage level. Using these parameters, the motor driver system is designed in Section 4.3.2.

4.3.2 Motor driver subsystem design

Now the motor driver system can be designed, as the power regulation system has been designed. Therefore, as the motor was chosen as a permanent magnet brushed DC motor, the best driver topology for the specific motor is an H-bridge motor driver system. To achieve the fine control needed of the motor, two types of H-bridge systems exist, either consisting of two N-channel MOSFETs for the low-side switching and two P-channel MOSFETs for high-side switching, Or consisting of four N-channel MOSFETs for both high and low side switching. However, due to the on resistance of the P-channel MOSFETs typically being higher than the on time resistance of N-channel MOSFETs N-channel MOSFETs are preferred for this application. There exists IC that incorporate both MOSFETs and can be switched simply by applying an input signal depending on the internal driver configurations.

However, two important factors should be considered when designing the motor driver circuitry. First, the switching frequency of the system, which is set to be 20 kHz as per the requirements, and secondly, the ground isolation between the input signals and the high-voltage motor driver circuitry. Ground isolation is important, as it helps protect the low-voltage electronics, such as the microcontroller and sensor systems from the high-voltage motor driver circuitry. This is achieved by isolating the input signal, such that the motor back electromotive force (EMF), does not influence the low-voltage electronics. Secondly, such an H-bridge motor driver circuit can be driven either in a unipolar or bipolar method. Where driving the system in a unipolar manner only switches the high side MOSFET, while keeping the low side MOSFET switched on while driving the motor in one direction. To change the direction of the motor, the opposite high-side MOSFET must be driven while the low-side MOSFET is kept on. In comparison, bipolar driving of an H-bridge motor driver requires switching both the high and low-side MOSFETs by providing a PWM signal to both the high and low-side MOSFETs, instead of only providing this PWM signal to the high-side MOSFET. This causes an interesting phenomenon when driving an inductive load, as can be seen in Figure 4.18.

Figure 4.18 shows the return path of the current when switching an inductive load, as denoted by I_{RETURN}, in the off portion of the duty cycle applied to the motor driver. When an inductive load is driven by an H-bridge system in a unipolar methodology, the return path comes from the ground plane through, the low side return diode, through the inductor, through the low side MOSFET and back into the ground plane. As the ground plane is a conductor with minimal resistance, meaning no measurable voltage difference will exist between the low side diode anode and the low side MOSFET source. However, the ground plane does experience a large alternating current during the off portion of the duty cycle. This can cause noise to be propagated to low voltage electronics if they share the same ground plane. In bipolar H-bridge driving systems, during the off portion of the duty cycle, the inductor return current is fed back into the supply. Therefore, such a system must have enough input capacitance to be able to sink this return current in order not to damage the source, if the source may be sensitive to voltage being fed back into it. Additionally, bipolar H-bridge driving systems are more prone to noise over the load when switching, because two MOSFETs are being switched to create the waveform, with

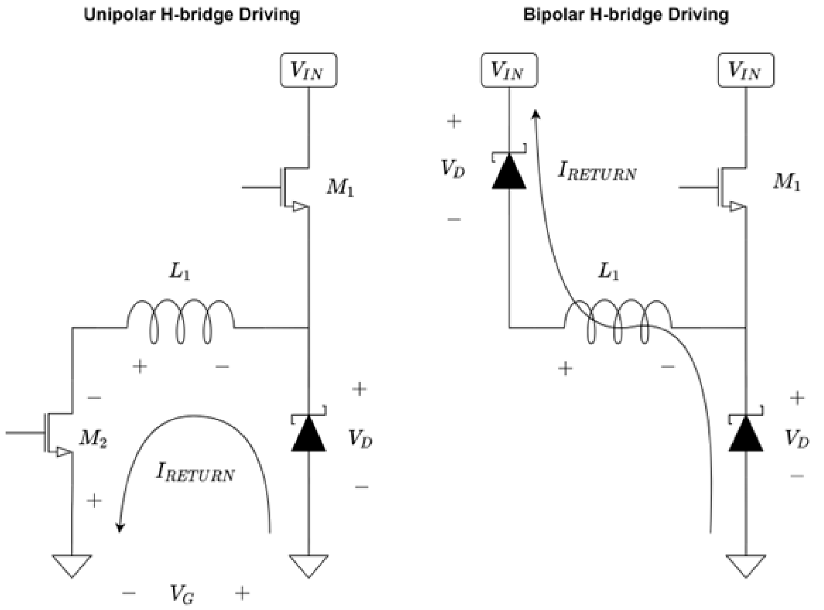

Figure 4.18: H-bridge driving methods

slightly different parasitic parameters. This can be mitigated by timing the switching of the MOSFETs, however this increases the complexity of the driver input signal required.

To mitigate the noise on the motor system, the motor will be driven with a unipolar H-bridge driving technique. However, to mitigate the potential noise on the low-voltage electronics, the ground of the motor driver system will be isolated from the low-voltage electronics. This will serve to drive the motor as effectively as possible, while protecting the low voltage electronic systems that will be mounted on the same PCB.

As mentioned previously, there exist integrated ICs that have the required MOSFETs internally. To use these ICs that have integrated MOSFETs the propagation delay between the input signal and output signal must be low enough to be able to switch at 20 kHz effectively without significant loss of duty cycle. Therefore, the propagation delay of such an IC is important, as the propagation delay will dictate the duty cycle of minimum and maximum duty cycle. This will dictate the amount of control over the motor, as the output duty cycle can be described by Equation 4.13 and will have a greater effect at higher frequencies. Where T_{ON} is the on time of the MOSFET, t_{ON} is the on time of the input signal, t_{DELAY} is the propagation delay of the IC and T_R is the rise time of the MOSFET, which depends on the gate to source capacitance and the current that the driver is able to source.

$$T_{ON} = t_{ON} - 2 \times t_{DELAY} - t_R \tag{4.13}$$

After investigating such integrated ICs, it was found that the typical propagation delay of these ICs were in the order to 10 - 100 μs. With such a high propagation delay, the maximum frequency to motor can be driven at will be decreased, as the rise time of the MOSFET is incorporated into the propagation delay in ICs with integrated switching MOSFETs. Therefore, the maximum switching frequency at which such an IC can be driven with a maximum duty cycle of 1 %, assuming a 1 μs propagation delay is therefore calculated as 9.54 kHz, which is insufficient according to the design requirements of the motor driver.

Therefore, to achieve the switching frequency with fine control of the motor, meaning a loss of duty cycle between the input signal and the output motor driving waveforms should be less than one percent. To achieve this, a MOSFET and driver system must be chosen such that the motor can be switched at the designed frequency of 20 kHz. The equivalent circuit of the MOSFET driver to the gate of the MOSFET is shown in Figure 4.19 below. It can be seen from Figure 4.19 that the value of R_1 should be chosen such that the inrush current to the gate of the MOSFET does not exceed the maximum driver current specified by the datasheet.

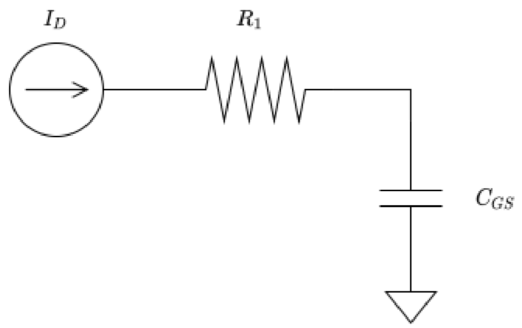

Figure 4.19: Motor driver to MOSFET gait equivalent circuit

Additionally, the type of MOSFET that will be used should be considered. Previously it was briefly mentioned that the N-channel MOSFET is preferable for this application, due to the fact that the R_{dson} or on resistance of the MOSFET is lower, leading to lower losses. However, the majority of the power losses when using MOSFETs for switching at high frequencies occurs during switching the MOSFET on rather than when the MOSFET is fully turned on. This is because, when switching the MOSFET on, as the gate charge rises from zero when applying a gate voltage, a current will flow through the MOSFET, while the drain to source voltage starts to decrease from a high to low value. This occurs whenever the MOSFET is switched on and off and therefore, at high frequencies, becomes the dominant power loss in the switching element.

Additionally, driving an N-channel MOSFET is more difficult in an H-bridge configuration, as when the N-channel MOSFET is used as a high-side switching element, the gate-to-source voltage may deplete when switching the MOSFET on. This can be seen in Figure 4.20, where it can be seen that when MOSFET M_1 is off and M_2 is on the source voltage at M_1 is V_{DS} of M_2. Then when a voltage is applied to the gate of M_1 which rises above the threshold voltage of M_1, the drain to source voltage of M_1 will decrease until the voltage at the source of M_1 is $V_{IN} - V_{DS}$. At this point the voltage applied to the gate of M_1 is equal or lower than the source voltage of M_1, which can cause it to turn off. This behaviour will then oscillate as long as the gate voltage is applied and the M_1 will not be in saturation allowing minimal current to flow to the motor. This can be counteracted by increasing the gate voltage of M_1 above the supply voltage V_{IN}. This will cause the gate-to-source voltage of M_1 to be positive, even when the source voltage at M_1 increases due to the MOSFET being switched.

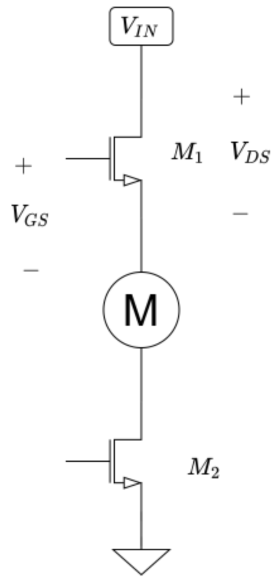

Figure 4.20: N Channel MOSFET H-bridge

However, due to the fact that the on resistance of a P-channel MOSFET being 2 to 3 times higher than an N-channel MOSFET and the fact that this system must be battery powered, optimising for efficiency will mean a longer battery life. For this reason, N channel MOSFETs are chosen to create the H-bridge.

To achieve this higher voltage, the MOSFET gate can be driven by a transformer coupled gate driver, or by a bootstrap gate driver. Both of these offer a suitable solution to the problem at hand, however transformer coupled gate drive systems require an additional transformer, which will increase the cost of the system significantly. Therefore, a bootstrap driver system was chosen. Bootstrap drivers utilise a capacitor as a voltage source to generate double the input voltage on the gate of the high-side MOSFET. This is done by connecting the bootstrap capacitor across the high side MOSFET M_1, the capacitor is charged while the high-side MOSFET M_1 is switched off through a bootstrap diode. The diode also prevents the bootstrap capacitor from discharging back into the source, which would deplete the bootstrap capacitor.

Therefore, after the MOSFET and driver topology has been chosen, the detail design of the driver circuit can be conducted. To do this, the MOSFETs will be chosen first, such that driver circuitry can be designed around it. The important parameters in the MOSFET are the voltage and current ratings and the gate capacitance, as well as the form factor. The MOSFET chosen for this application is the Si4816BDY, which features a dual MOSFET package configured in a half bridge, with an incorporated reverse biased Schottky diode across the low-side MOSFET. For this reason, as well as the other parameters being acceptable such as the low gate-to-source capacitance, this MOSFET was an ideal candidate for this application. To drive this MOSFET configuration, a bootstrap MOSFET driver is required, as discussed previously.

As the supply voltage is regulated to 12V, and the range in which the bootstrap driver can output current is typically up to 2A, a minimum value for R_1 is 6 Ω. However, due to the fact that the rise time calculated fully charge the gate capacitance was found to be less than the typical propagation delays of the bootstrap drivers, the propagation delays of the bootstrap drivers are deemed to be the deciding factor in the switching frequency. For this reason, a bootstrap driver with a low propagation delay and high driving current is required. A suitable choice was found to be the IRS2007 bootstrap driver IC, with a propagation delay of 160 ns and maximum driving current of 290 mA. R_1 was chosen at 50 Ω to limit the driving current at 240 mA and therefore the maximum switching frequency was calculated at 45.6 kHz with a 1% loss in duty cycle from input to output. The IRS2007 also provides shoot-through protection, which prevents creating a short circuit by accidentally switching the high and low side MOSFETs on in one half bridge.

To model the behaviour of the motor driver circuit, the system is simulated in LTSpice. However, to simulate the system, models of the physical components are needed to accurately represent the real system. As no models were found for the chosen IRS2007 bootstrap driver, for this reason an ideal model was constructed by referencing the functional block diagram in the datasheet. As the high and low side drivers function independently, two separate input to MOSFET driver circuits are needed. However, these circuits must be modelled to have the same propagation delay as given in the datasheet and was modelled using a decoupling capacitor and resistor network with a Schmitt trigger. Shoot through protection is modelled using a simple logic circuit. The output drivers were modelled using ideal switches in a push-pull configuration, however, the maximum output driver current is therefore not modelled as per the datasheet. The simulation model of the IRS2007 therefore, models the shoot through protection, and the propagation delay as accurately as possible according to the datasheet.

Using the model of the IRS2007 as developed in Figure 4.21, the motor driver circuit can be simulated, to determine system parameters before manufacturing the PCB. The circuit

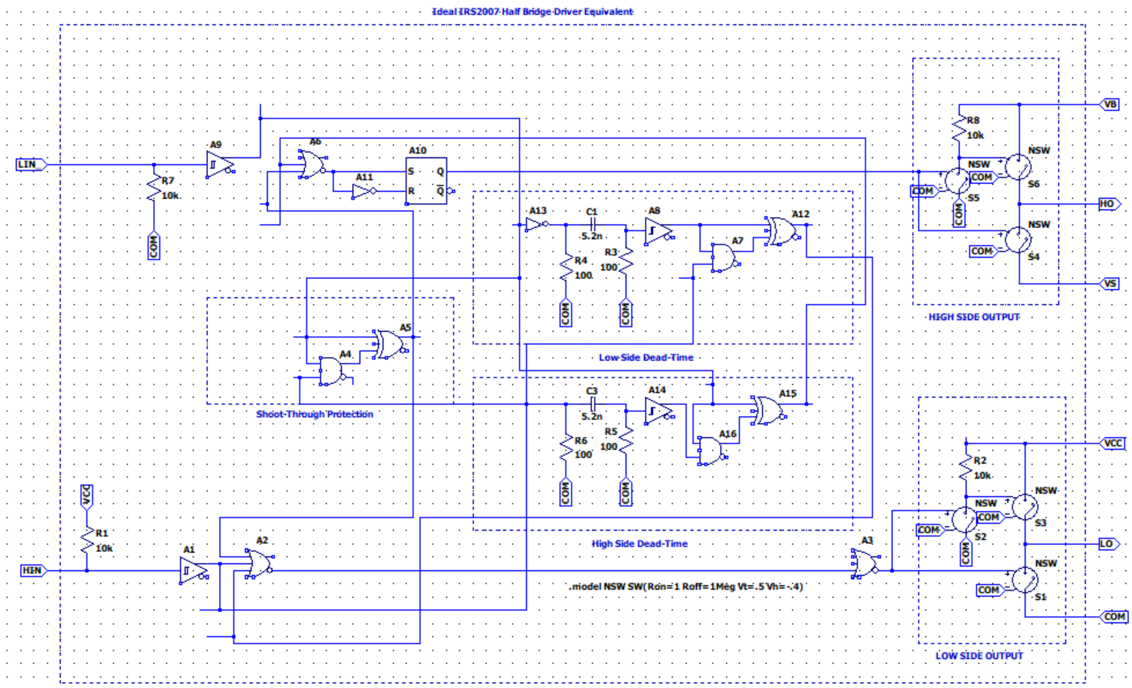

Figure 4.21: IRS2007 bootstrap driver model

set up in the simulation is shown in Figure 4.22. A bootstrap diode and capacitor were chosen iteratively, as a Schottky diode is needed charge the capacitor at the switching frequency and a large enough capacitor is needed not to be fully discharged into the gate of the MOSFET. However, if the bootstrap capacitor is too large, if will not be fully charged by the time it is required to drive the gate voltage. The motor is modelled as the load of the system, by using the motor's internal resistance, inductance and a voltage source that can be varied to simulate the motor back EMF.

Simulating the circuit when driving the circuit in a unipolar driving technique with a low back EMF, yields an output as can be seen in Figure 4.23 below. The top plot plane displays the motor voltage, the middle plot plane displays the current through the various circuit components and the bottom plot plane displays the high and low side MOSFET gate voltages. As can be seen from Figure 4.23, the high side gate voltage is effectively driven above the supply voltage of 12 V, using the bootstrap gate driver. The return path of the current discussed in Figure 4.18 is also observed, as when the high side MOSFET is switched off, the motor current can continue to flow through the bottom reverse biased diode through the low side MOSFET, which is kept on, as seen in Figure 4.23.

In contrast, driving the motor in a bipolar driver methodology yields the results that can be seen in Figure 4.24 below. As can be seen, switching the low-side MOSFET when driving the motor creates the return path as can be seen in Figure 4.18. When the low-side MOSFET is switched off, the motor current is then driven back into the supply through the body diode of the high-side MOSFET M1. However, as this is less

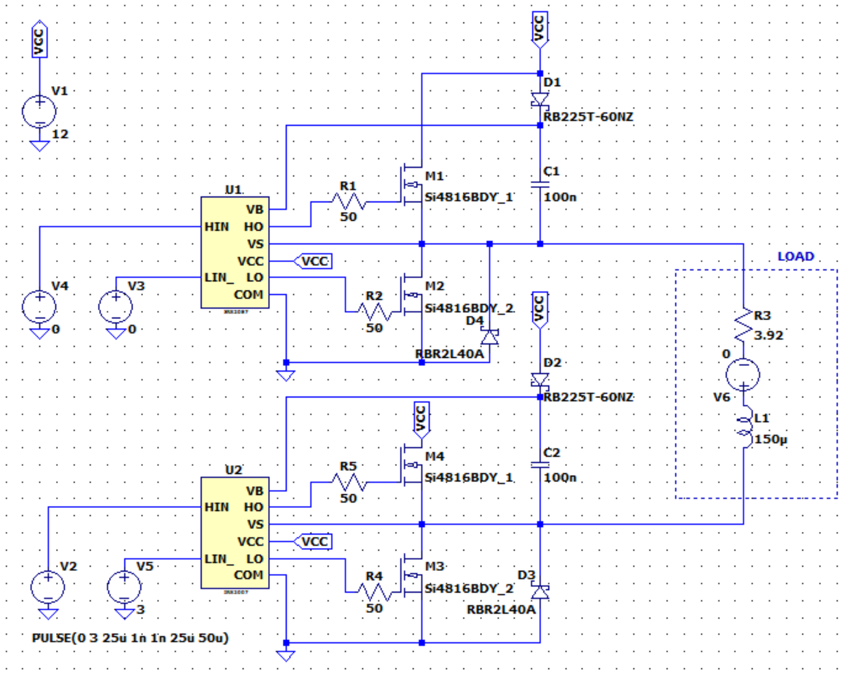

Figure 4.22: Motor driver circuit simulation

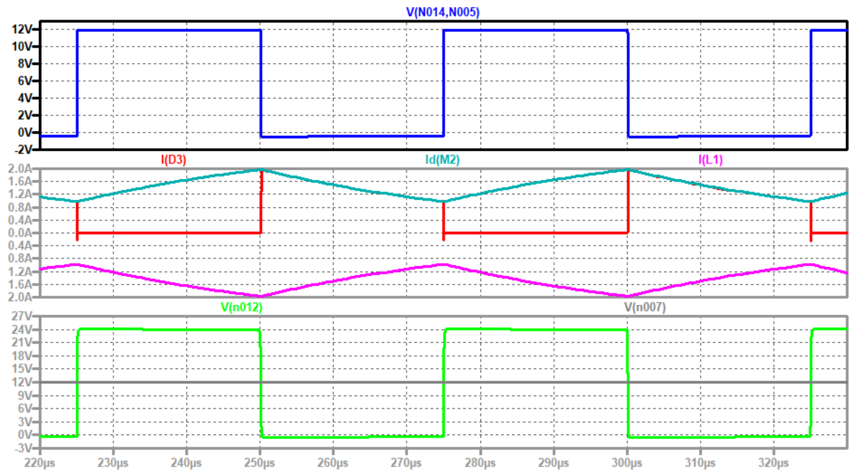

Figure 4.23: Unipolar motor driver simulation

effective at sinking the motor current when the high-side MOSFET is switched off, the motor current is then decreased to zero before the motor is inductively discharged. This creates an inductive ringing across the motor winding, which is fed back onto the gate of the high-side MOSFET.

When the motor is spinning freely under a minimal load, the back EMF will be a non-zero opposing force, to model this effect on the motor driving circuit, the voltage source V6 can be increased from zero to a voltage expected on the motor. This voltage can be determined by multiplying the motor back EMF constant supplied by the datasheet by the no-load speed. The results that can be observed are similar to the effects observed

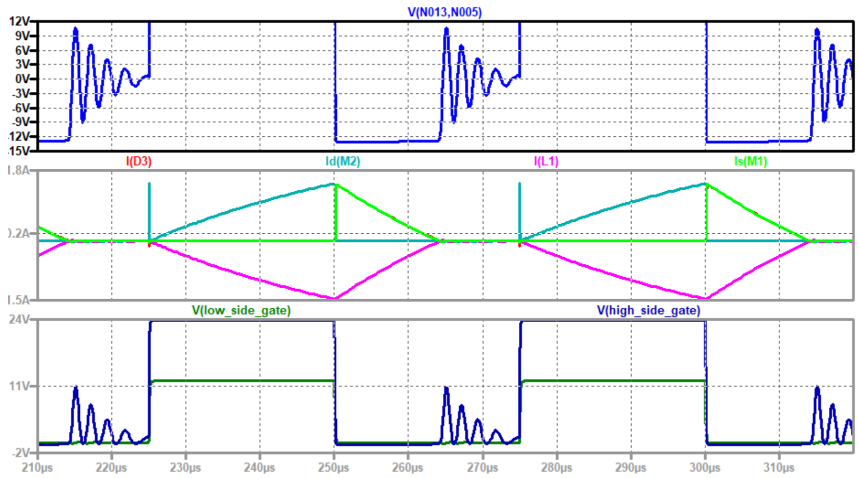

Figure 4.24: Bipolar motor driver simulation

in Figure 4.24, but are instead caused by the fact that the back EMF is fed back onto the gate voltage through the bootstrap driver, raising the high-side gate voltage, which lengthens the effective duty cycle over the motor. However, since the motor will always be connected to the load, this is decided to be negligible.

Therefore, in summary, both the power supply and motor driver systems have been designed. Now, the design of the low-voltage electronics, such as the microcontroller, IMU and strain gauge measurement system will be discussed in Section 4.3.3.

4.3.3 Microcontroller and sensor subsystem discussion

Unlike the other power electronics related subsystems, the low voltage electronics, including the microcontroller and sensor systems are only discussed in detail. This is due to the fact that the components were chosen based on technical specifications, and the PCB around these components is designed according to the datasheet as well as PCB design rules as discussed in Section 4.3.1.

For the microcontroller selection, a STM32F446 was chosen, as this microcontroller has a high clock frequency of 180 MHz, as well as a flash memory of 512 KB. This should be powerful enough to do the processing required of the incoming data, then classify the terrain based on the analysed data and drive the motor to a specific position.

The chosen IMU is the LSM6DSOTR, as this IMU can be communicated with, using either the inter-integrated circuit (I2C) protocol or serial peripheral interface (SPI) protocol. The LSM6DSOTR can be configured to send a wake-up signal if it experiences a movement after a period of being stationary, as well as can be configured to detect certain gestures. For these reasons, as well as the high resolution of the accelerometer and gyroscope, the LSM6DSOTR is a suitable IMU for this project. The additional features briefly mentioned previously may not be used in the current design, due to time constraints on the project. However, may prove useful if the project is further developed into a product.

To offset thermal drift present in passive resistive sensing elements, two strain gauges are mounted one on each side of the carbon blades, in the direction of maximum flexion. This allows the thermal drift of the resistors to offset each other, causing the Wheatstone bridge to remain balanced even after a long period of time. As both the toe blade and heel blade were measured, two Wheatstone bridges are created to measure the flexion of the blades independently. To achieve this, an amplifier system is needed to amplify the voltage measured in the Wheatstone bridge formed by the strain gauges and precision resistors. After experimenting with the change in resistance of a single strain gauge when applying a known load, an appropriate amplification system can be chosen. The voltage that can be expected when a load is applied to the blades was calculated to be in the order of microvolts. To achieve this amplification, a 24-bit analogue to digital converter (ADC) was determined to be acceptable for this application. The MCP3562 was chosen as it has two differential inputs, meaning it can measure both Wheatstone bridges. As it only supports SPI communication, only a single SPI bus is needed to communicate to both sensor systems.

Now that the design of the electrical system has been discussed, the final design is brought together to be manufactured on a PCB, as can be seen in Figure 4.25. The design rules of the power electronics board also applies to this PCB, with emphasis placed on the ground and reference voltage plane continuity and track distance.

In summary, the electrical system consisting of a power regulation board and a control board was designed. With the motor driver and sensors added to the control board, as well as galvanic isolation between the 3 V and 12 V systems. This was achieved using an isolated step-down integrated power supply and opto-isolators to ensure the safe operation of the low-voltage components. Additionally, an output connection was designed for a Bluetooth module to allow for remote data logging, however due to time constraints, this was never used. In Section 4.4 the terrain classification system and control system of the prosthetic ankle will be designed.

4.4 Controller and terrain classifier design

This section consists of two main subsections, mathematical modelling and control system design for the position controller and data driver terrain classification. To derive the system model, the system dynamics are considered, including the permanent magnet brushed DC motor equivalent circuit and the mechanical system dynamics. The motor back EMF is factored into the differential motor dynamics, and thus the motor dynamics are described using Equation 4.14. Where K_B is the back EMF constant of the motor and

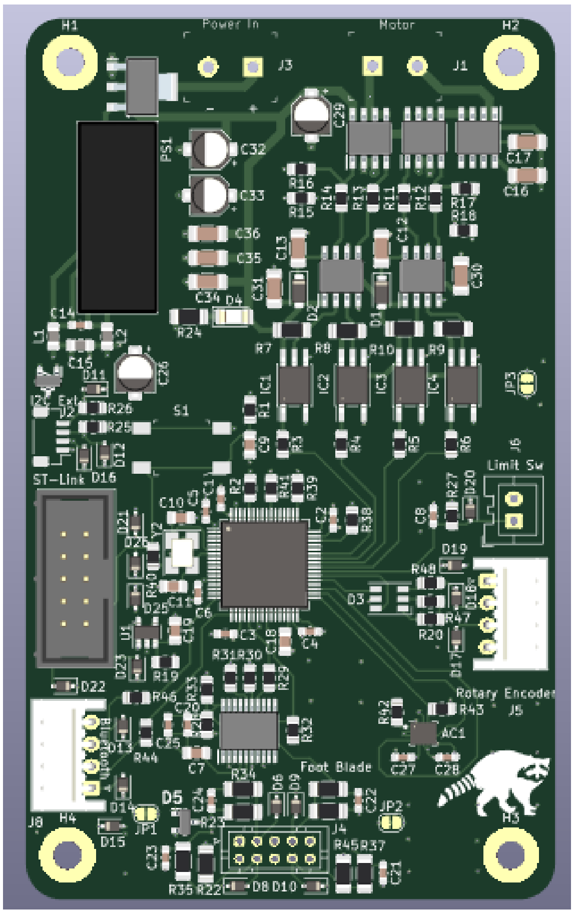

Figure 4.25: Motor driver and low voltage electronics

ω_M is the speed of the motor.

$$V_{in} = L_a \frac{dI_a}{dt} + I_a R_a + K_B \omega_M \tag{4.14}$$

Now the system dynamics must be discussed, such that the input voltage to output position transfer function and system dynamics can be derived. To define the mechanical behaviour of the mechanical system, the axis of rotation of the lead screw is considered, as the load from the foot blades can be considered as acting on this axis. Therefore, using Newton's second law, the torque about the axis of rotation of the lead screw can be written as shown in Equation 4.15. Where, the torque applied on the lead screw by the motor can be calculated by the back EMF constant and the current to the motor, as well as the estimated belt drive efficiency. Where β is the linearised friction constant, J is the inertia of the rotating elements about the lead screw axis of rotation and ω_{LS} is the rotational speed about the lead screw rotational axis.

$$2I_a K_B \eta_B - \beta \omega_{LS} - J \frac{d\omega_{LS}}{dt} = 0 \tag{4.15}$$

The relationship between the ankle rotational speed about the ankle joint and the speed of the lead screw can be calculated when considering the length of the lead screw link and the length of the foot blade mount to be two intersecting circles. Using trigonometric identities after transposing the coordinates of these circles onto a new axis, the length of the lead screw relates to the ankle angle by Equation 4.16. Where r is the distance between the top mounting position of the lead screw link and the ankle joint, d is the distance between the foot blade mount linkage joints, LS is the length of the lead screw link, ψ is the angle between the vertical Cartesian axis and the new axis that the coordinates are transposed, which is -65.556deg and θ_a is the ankle angle.

$$\theta_a = \arccos\left(\frac{(\frac{r^2-d^2+LS}{2r})\cos(\psi) + \sqrt{LS^2 - (\frac{r^2-d^2+LS^2}{2r^2})\sin(\psi) - d}}{d}\right) \tag{4.16}$$

The ankle angle can be approximated by considering the lead screw link to be vertical through all ankle angles. The ankle angle can therefore be approximated using the arc length theorem. Additionally, the ankle angle can be approximated by linearisation using the Taylor polynomial of Equation 4.16. However, as the lead screw remains close to vertical through the operational ROM of the ankle system, therefore, arc length theorem is a simpler expression that yields appropriate results. This allows the angular speed of the ankle about the ankle joint to be described by the linear speed of the lead screw link by derivation of the arc length theorem. Therefore, by rewriting Equations 4.14 and 4.15, as well as utilising the arc length theorem, a state space matrix of all the states of the system can be constructed and can be seen in Equation 4.17 below.

$$\begin{bmatrix} \dot{I_a} \\ \dot{\omega_{LS}} \\ \dot{\theta_a} \end{bmatrix} = \begin{bmatrix} -\frac{R_a}{L_a} & \frac{K_B}{2\times L_a} & 0 \\ \frac{2K_T\eta_M}{J_T} & -\frac{B_T}{J_T} & 0 \\ 0 & \frac{l}{2\pi d} & 0 \end{bmatrix} \begin{bmatrix} I_a \\ \omega_{LS} \\ \theta_a \end{bmatrix} + \begin{bmatrix} \frac{1}{L_a} \\ 0 \\ 0 \end{bmatrix} V_{IN} \tag{4.17}$$

Using the state-space matrix, a signal flow diagram of the system can be constructed, as can be seen in Figure 4.26.

From the state space model, using an estimated sampling frequency of 1 kHz, the transfer function can be calculated as follows, assuming a zero-order hold data-capturing technique.

$$G(Z) = \frac{0.0002031Z^2 + 0.000239Z + 8.597e-7}{Z^3 - 1.992Z^2 + 0.9919Z - 1.432e-10} \tag{4.18}$$

The PID controller to control for the ankle position can be designed by improving the phase margin at a chosen frequency such that the system adheres to the rule outlined in Equation 4.19 below. Where ω_{w1} is the chosen frequency, D is the controller function, G is the plant function and ϕ_m is the phase margin.

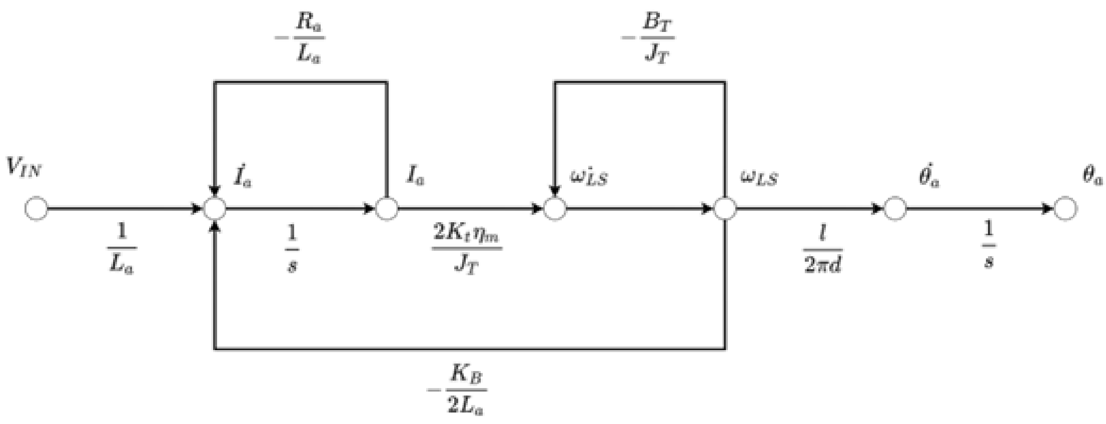

Figure 4.26: Signal flow diagram

$$D(j\omega_{w1})G(j\omega_{w1}) = 1\underline{/(-180\,\text{deg} + \phi_m)} \tag{4.19}$$

To achieve a phase margin of 55deg, at 20.3107 rad/s, the following parameters for the PID position controller were chosen. Kp was calculated at 0.72, the ratio of Ki/Kd was calculated and Ki and Kd were chosen at 0.06064 and 0.001516 respectively. The filtering constant was chosen at 100, such that the derivative gain becomes less sensitive to potential high frequency noise. Figure 4.27 below shows the step response of the mathematical model with the designed PID controller, assuming a sampling frequency of 1 kHz.

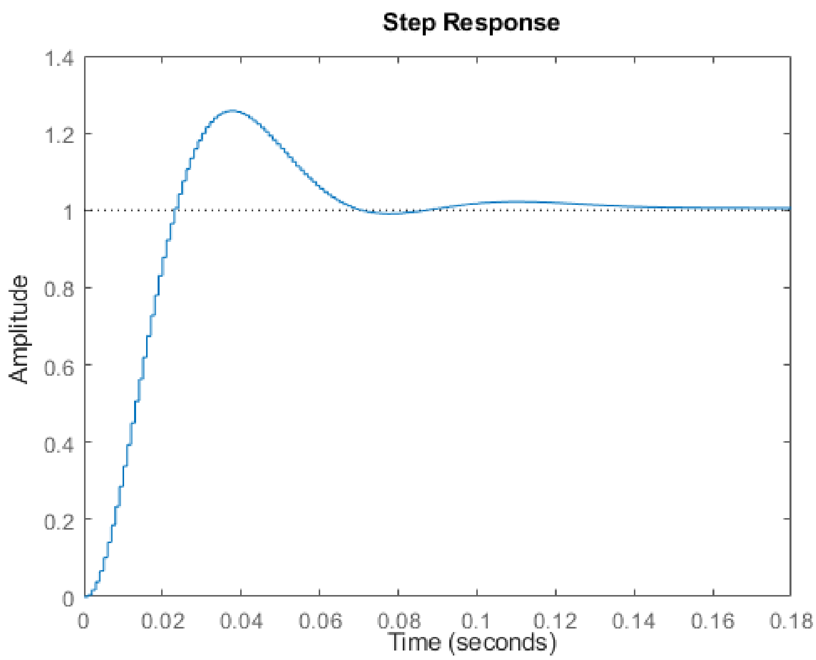

Figure 4.27: Step response from designed PID controller

Now that the mathematical model of the system is constructed, and the low-level controller has been designed, the high-level terrain classification should be designed. The state estimation is done as discussed in Section 3.4.2, using the strain gauges to detect the gait events as can be seen in Figure 3.2. The goal of the terrain classification system is to determine the terrain being traversed in real-time on an embedded system, using the proprioceptive sensor scheme designed in Section 3.4.2.

This can be done a number of ways, however the data used to design this system consists of 10 subjects traversing different terrain inclinations at different speeds for 1 minute. Meaning that for each experiment for each individual, there are ± 60 data points per experiment. Further, the test bench that the system was designed to be tested on is designed to allow the prosthetic to "walk" at different preset inclinations.

Based on the data available and the implementation of the terrain classification system, the examples found in literature were discussed in Section 2.5. Section 2.5 discusses classification algorithms rather than prediction algorithms for deciding the terrain being traversed, as most applications are aimed at deciding between stair ascent and level ground walking. Additionally, if the system were scaled up to include different terrains, such as stair climbing in the future, a classification system must be used as the terrain will then no longer be feasible to predict. However, for this application classification techniques will be used as it fits the criteria of the current problem and can be scaled to fit a possible future problem.

The terrain classification is done using both fuzzy logic and LDA, where the results, as well as the computational complexity, are compared to determine the most suitable terrain classification system for this application. Firstly, the fuzzy logic terrain classification system will be designed. Fuzzy logic allows a human to enter a range of acceptable inputs for each of the input variables to be mapped to one or more output variables. This can be achieved using data or can be done using knowledge of the system. In this case, there are two input variables, consisting of the shank angle measurement at two different gait phases, and one output variable, namely the terrain inclination in degrees. The relationship between the input variables and the output variable is based on the data trends observed for the data dispersion of AB10; however, it can be fully customised because of the nature of fuzzy logic.

Fuzzy logic systems are then also outputted as a control surface, which maps the input variables to the terrain output variable over the specified input range. The input ranges are found using shank angle data of healthy individuals as recorded by Embry et al. [13]. After analysing the data, two variables were chosen to detect the terrain: the shank angle at the flat-foot event and the shank angle at the toe-off event. Figure 4.28 below shows the distribution of the chosen variables, flat-foot shank angle in degrees (FF) or toe-off shank angles in degrees(TO). This is shown over a range of inclinations being traversed from a decline of 10° shown in blue to an incline of 10° shown in green, where the walking speed during the trial was kept at 1 m/s. Therefore, the legend of Figure 4.28 follows the format of s x i/d y, where x refers to the walking speed and i/d refers to whether the terrain angle y is measured as an incline or decline. AB01 to AB09 is shown in Figure 4.28, as ten individual data dispersions do not fit well onto an image.

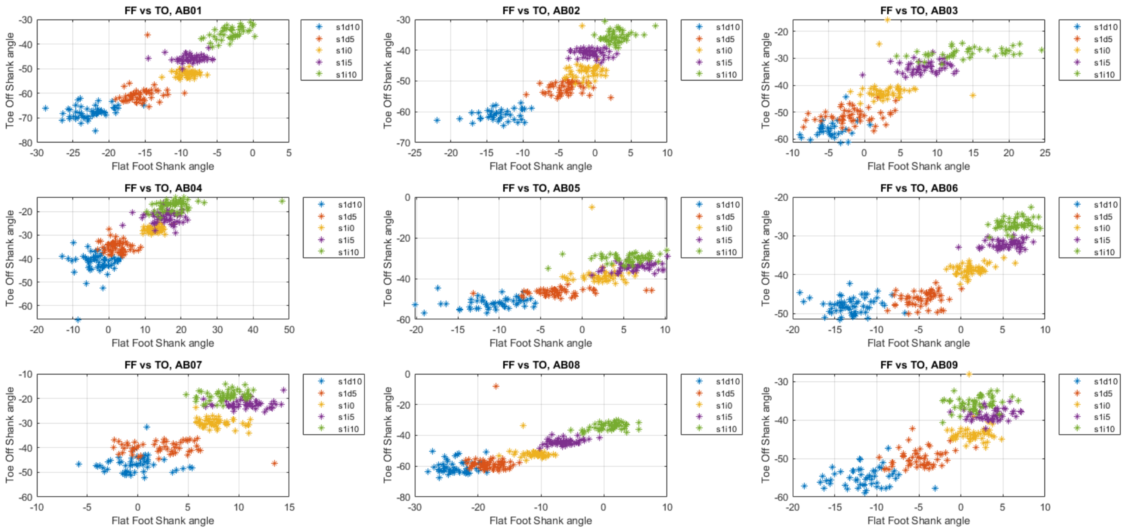

Figure 4.28: Data distribution of different pilots

From Figure 4.28, it can be seen that the distribution of variables for each individual follows a similar trend. However, the ranges of each of the variables vary widely between individuals. For this reason, the fuzzy logic classifier using the shank angle at different gait events will be designed for a single individual. Figure 4.29 below shows the fuzzy logic terrain classification surface when considering AB10, the tenth individual in the data collection set. AB10 was considered as this participant had a good dispersion of data, similar to AB09, AB01 or AB04. A different control surface would need to be generated for each individual due to the natural differences in walking mechanics as a result of varying limb lengths.

The accuracy of the fuzzy logic classifier can be determined by measuring how accurately this classifier is able to detect the terrain based on the shank angle variables. The classification accuracy is evaluated by two different standards, how accurately the classification system is able to estimate the terrain with a margin of ±2°, denoted as the angle estimation in Figure 4.30 and how accurately the classifier can detect whether the terrain is an incline, decline of level surface, denoted as the basic estimation in Figure 4.30. It can be seen in Figure 4.30 that the angle estimation accuracy is low at a terrain inclination of -7.5° and +10°, this is because the input variable can exceed the specified variable range set in the fuzzy logic classification system. This can happen if the specific relationship between the input variables and the output variables does not cover the specific group range exclusively. This happened here because the input variables were incorrectly estimated

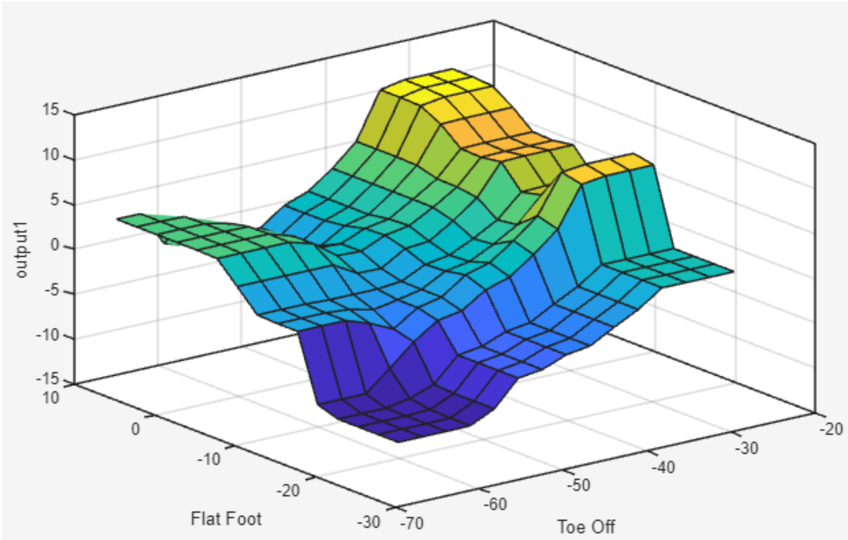

Figure 4.29: Fuzzy logic classification surface

at -10±1° in the case of the input variables of the -7.5° terrain inclination experiment. However, the fuzzy logic classification system is capable of providing an accurate basic estimation of the terrain throughout the entire range. This is simply the basic information of terrain level, meaning classifying the terrain as an incline, level surface or decline.

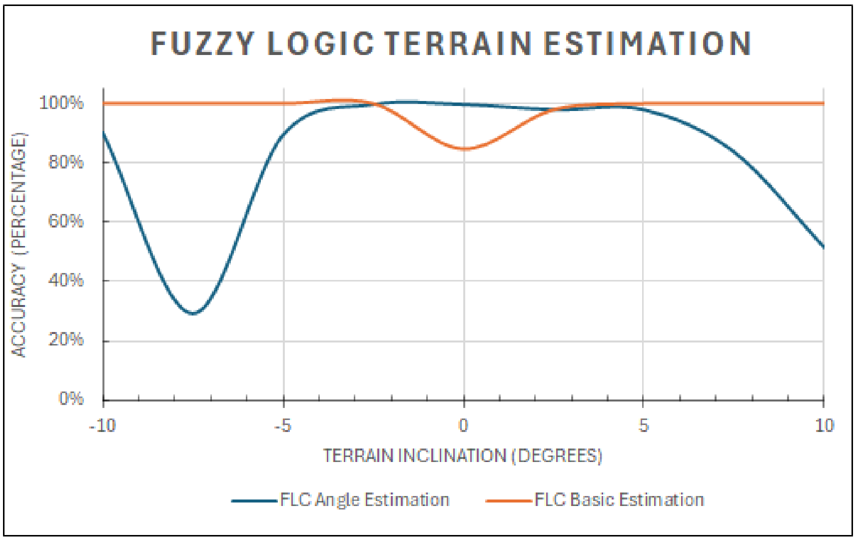

Figure 4.30: fuzzy logic classifier accuracy

In comparison to fuzzy logic, LDA can be mathematically computed to increase the separation between the classes by reducing the dimensionality of the dataset. This allows the system to be transposed onto a one-dimensional range that will enable maximum separation between the data collected at different terrains. The same individual was used to create the LDA classifier, such that the fuzzy logic classifier can be compared to the LDA classifier.

LDA is computed by first calculating the d-dimensional mean vectors of the different classes in the dataset. This vector is the vector of the means of each variable in a class and is represented by a $n \times m$ matrix, where n represents the classes, in this case, the different trials conducted at varying terrain inclinations, and m represents the variables, meaning the shank angle at the flat-foot and toe-off events. Then the scatter matrix between the classes must be computed. The within-class scatter matrix can be calculated by Equation 4.20 below, where $\mathbf{m}_i$ is the mean vector for each class or inclination. Additionally, $\mathbf{x}$ refers to the variable vector.

$$\mathbf{S}_w = \sum_{i=1}^{c} \sum_{\mathbf{x} \in Di}^{n} (\mathbf{x} - \mathbf{m}_i)(\mathbf{x} - \mathbf{m}_i)^T \tag{4.20}$$

The between-class scatter matrix can be calculated using Equation 4.21, where N_i is the sample size of the respective classes and $\mathbf{x}$ is the overall mean vector of the class. Additionally, c refers to the number of classes within the dataset. In this case c refers to the amount of different terrain inclinations that data was recorded for AB10.

$$\mathbf{S}_B = \sum_{i=1}^{c} N_i(\mathbf{m}_i - \mathbf{m})(\mathbf{m}_i - \mathbf{m})^T \tag{4.21}$$

The dataset can then be transformed along a new axis given by the eigenvector with the largest corresponding eigenvalue from the multiplication of $\mathbf{S}_w^{-1}\mathbf{S}_B$. The transformation of data along both eigenvectors is shown in Figure 4.31 below. From Figure 4.31 it can be seen that the separation of the classes is maximised along eigenvector 2 with the largest corresponding eigenvalue. The legend in Figure 4.31 follows the convention laid out previously in Figure 4.28, where s1i2x5 means that the experiment was conducted at 1 m/s and at an incline of 2.5° with the horizontal. Figure 4.31 does not include the data dispersion for 7.5° and -7.5°, as this would be difficult to see on the data dispersion. However, the LDA classifier was built including these datasets.

Similar to the fuzzy logic classifier, the LDA classifier is evaluated based on the estimation accuracy of the angle of the terrain within a ±2° margin, denoted as the angle estimation in Figure 4.32 and classification of the terrain, denoted as the basic estimation in Figure 4.32. Analysing the classification accuracy of the LDA, as shown in Figure 4.32, it can be seen that the classification done using LDA is more stable across the range of trials than the fuzzy logic classifier, although having a lower peak accuracy. For this reason, the LDA classifier is preferred, as the higher stability across the range of inclinations to be more robust in comparison. Comparing the average classification accuracy between the LDA classifier and the fuzzy logic classifier, it was found that the fuzzy logic classifier had a higher average classification accuracy across the entire input range of 82.42%, where the LDA classifier had a classification accuracy of 80.60%. While the basic classification

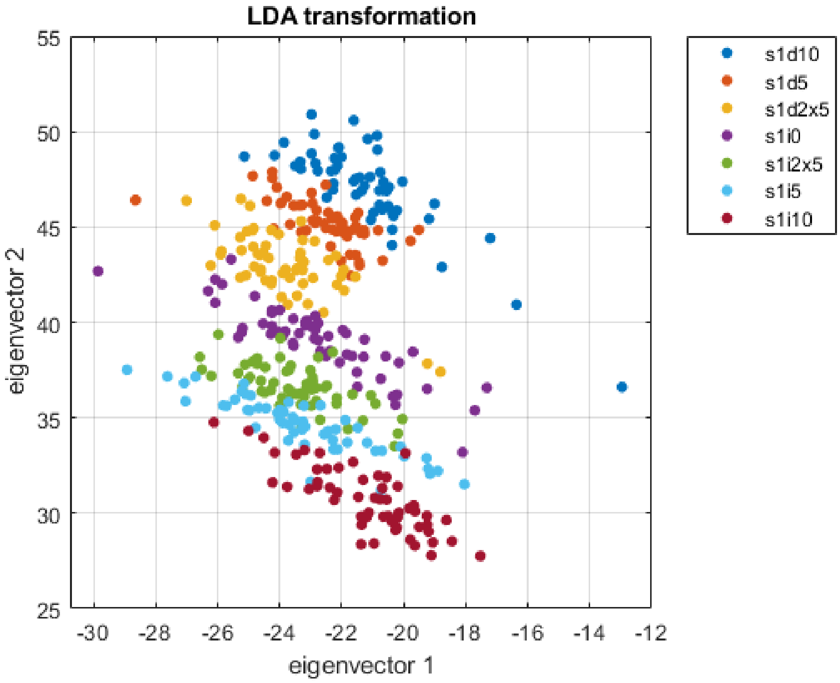

Figure 4.31: LDA transformation along eigenvectors

accuracy also favours the fuzzy logic classifier with an average classification accuracy of 98.11% across the entire range, where the LDA classifier had a classification accuracy of 97.09%.

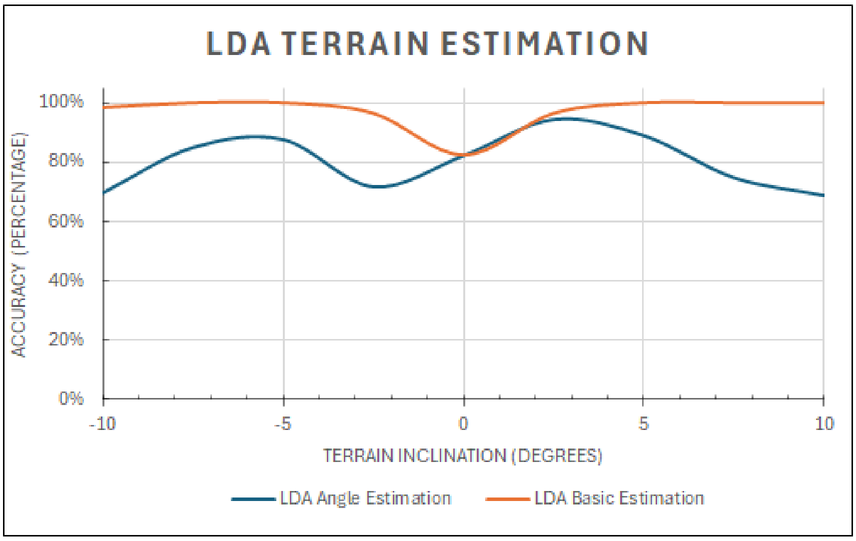

Figure 4.32: LDA classification accuracy

Additionally, in comparison to the method of implementation of the fuzzy logic classifier which can be exported as a lookup matrix, the LDA can simply be computed in real time once the classifier is built. This is done by multiplying the measured variables with the chosen eigenvector and then deciding the terrain inclination based on decision boundaries or linear projection.

4.5 Summary of detail design outcomes

In summary of the detail design done in this chapter, a mechanical system was designed, along with an electrical system to actuate the mechanical system and measure important physical parameters. Additionally, a control system was designed based on the control systems in literature as well as the sensor systems chosen. The system was designed to meet the functional design requirements, and design choices were made to meet these design requirements. Figure 4.33 below displays the fully constructed and manufactured prosthetic ankle system as designed in this chapter.

In the coming chapter, the design will be implemented and tested, such that the system design can be verified, and a final conclusion can be drawn on the feasibility of the system.

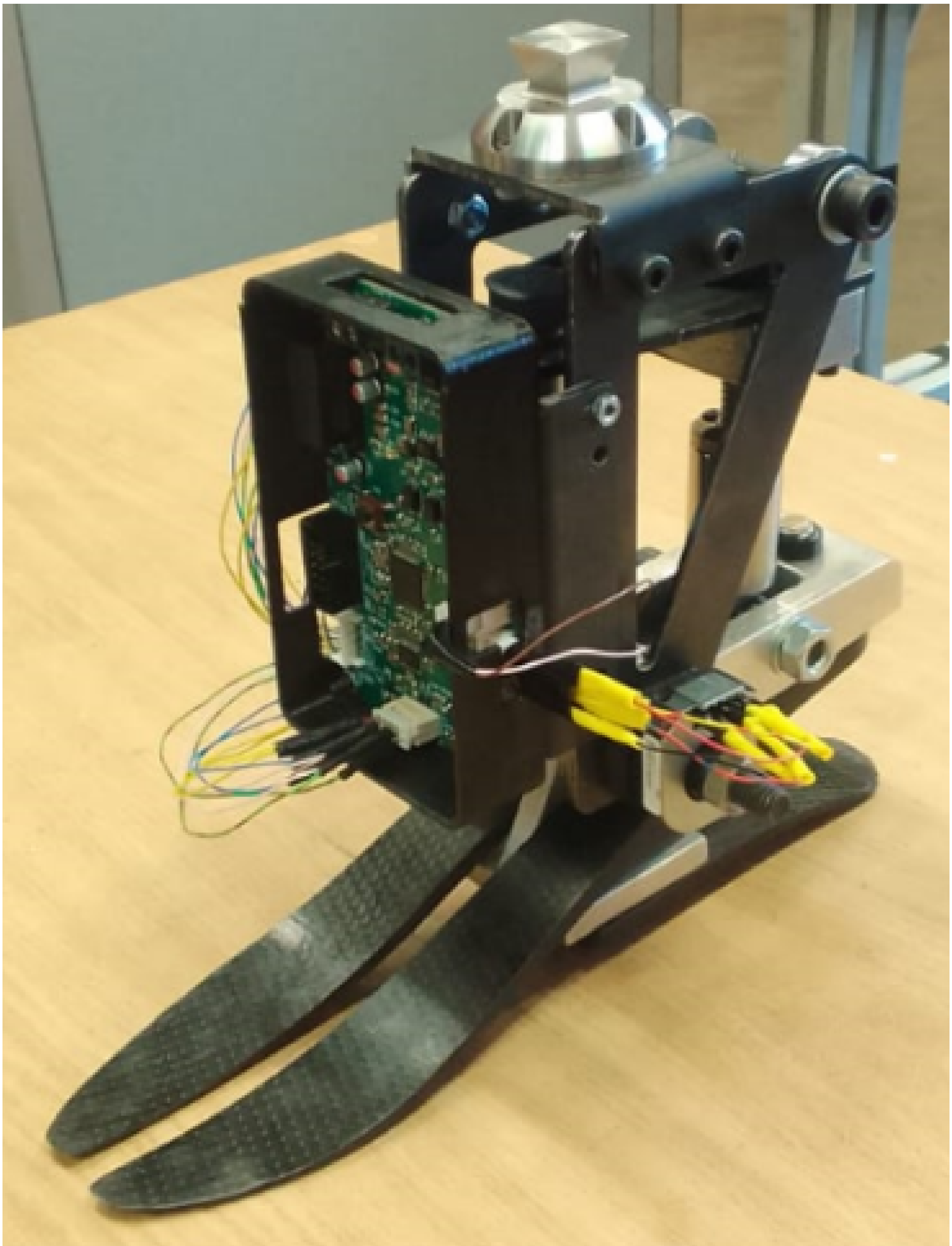

Figure 4.33: Designed prosthetic ankle system

Chapter 5

System verification and validation

5.1 Introduction

This chapter is dedicated to verification and validation of the low-cost terrain-adaptive ankle, by testing the subsystems separately and later the system as a whole. The prosthetic ankle is tested on a test bench to avoid ethical conundrums involving sourcing a human pilot and providing an experimental procedure to be approved by a scientific committee.

This chapter is divided into the following subsections. Testing the sensor implementations in Section 5.2, testing and validating the system model in Section 5.4, verifying the position control of the system in Section 5.5 and verification of the final system.

5.2 Sensor verification

This section will verify the chosen sensors and explain the experimental procedure behind the testing. The sensor systems chosen in Section 3.4.2 were proprioceptive, with an IMU and strain gauges placed on the blades of the foot. In order to use the strain gauges effectively, the sensor readings must first be calibrated.

The strain gauges mounted on the carbon toe blade and heel blade of the prosthetic ankle were calibrated by loading each blade separately in intervals of 1 kg from 0 to 8 kg. The load placed on the ankle was verified using a calibrated digital scale, and the output data was sent to a computer using the STM32 Serial Wire Viewer interface in the STM32 CubeIDE. The raw strain gauge output data is displayed for the strain gauges mounted on the heel blade and the toe blade in Figure 5.1 below.

The linear trend line of the data was then calculated and used to determine the offset

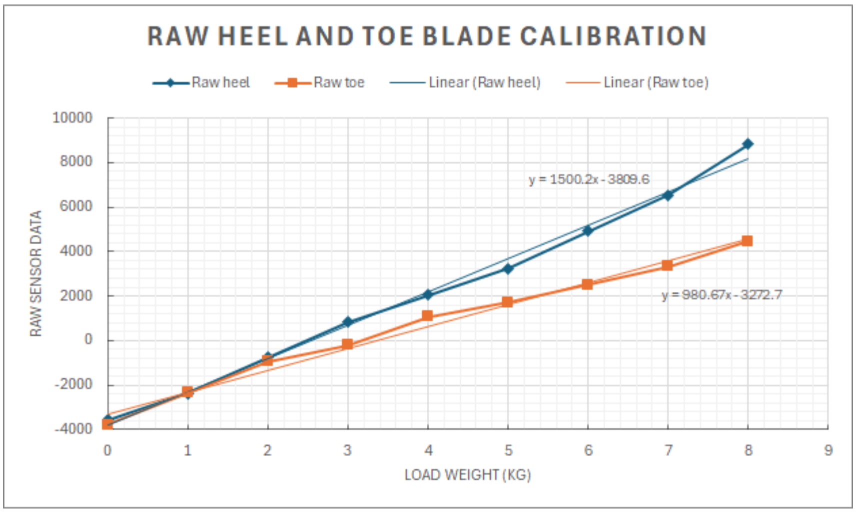

Figure 5.1: Strain gauge calibration

and calibration factor needed to convert the raw sensor data into a useful reading. After the sensors have been calibrated, a step was simulated by placing the prosthetic ankle on a digital scale and creating the stance phase motion of the prosthetic ankle by hand. The data recorded is shown in Figure 5.2 below. Assuming that the blades used in the prosthetic ankle system do not undergo permanent deflection from a stress higher than the yield stress, the calibration factor should remain accurate when the full weight of a user is placed on the prosthetic ankle.

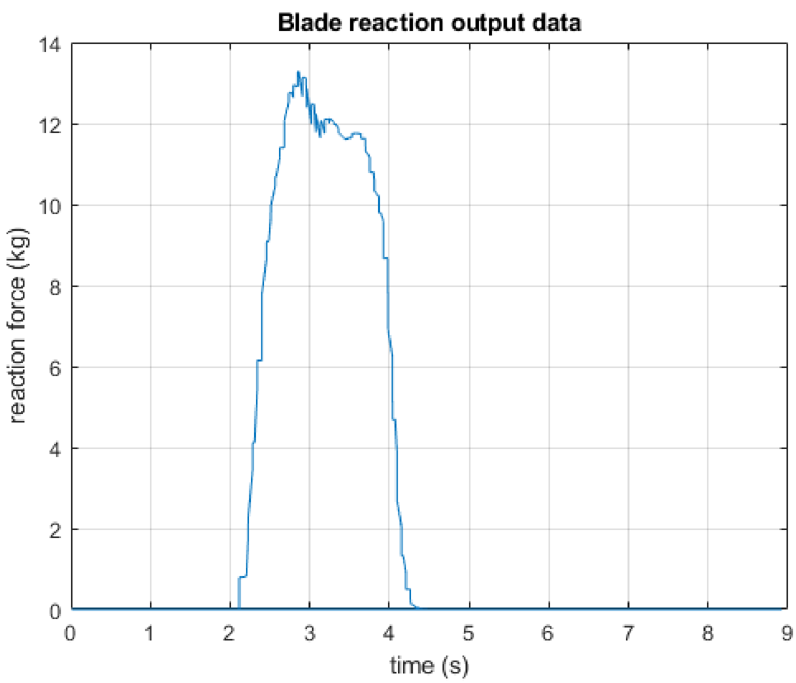

Figure 5.2: Blade reaction force during gait

To calculate the reaction force displayed in Figure 5.2, the heel and toe blade reaction force is summed together. This allows for the reaction force to be read with the added information of which area of the foot was most active during the stance phase. This may be important for future work as it allows this extra information to be captured when the ankle system is used by an amputee, which will allow improvements to the terrain detection system.

However, for the purposes of further implementation, the strain gauges readings are sufficient. As the reaction force given by the strain gauges allows for enough information to be collected to determine three critical events during the stance phase, as shown in Figure 3.2.

Heel strike, when the heel of the foot initially makes contact with the surface, was discussed in Section 2.2. Heel strike can be found either from detecting an increase in the reaction force or directly from detecting an increase in the weight on the heel from zero. Flat foot, or mid-stance, was discussed in Section 2.2. Flat foot occurs at the local minimum of the reaction force [32]. This is found by calculating the derivative of the reaction force to monitor for local minima. Toe-off or pre-swing was discussed in Section 2.2. This event is characterised as the moment before the foot is lifted from the surface, therefore it can be identified by either monitoring the reaction force or the toe blade specifically for the boundary value before the ankle enters swing phase.

In contrast to the force plate data collected by Embry et al. [13], where the force plate data is normalised across a number of participants, the data collected from the blade-mounted strain gauges are accurate enough to detect the gait phases within a simulated gait cycle. However, calibration inaccuracies and sampling time prevent a perfect reading. Despite these shortcomings, the blade-mounted strain gauges provide enough information to determine the important gait events as well as estimate the state of the system by determining if it is being used to support the user. Normalised force plate data is shown in Figure 5.3 as recorded by Embry et al. [13] for comparison to the shape of the data in Figure 5.2.

The IMU was implemented, where the shank angle was measured using both the accelerometer and gyroscope together to measure the shank angle more accurately. Figure 5.4 below displays the shank angle data recorded using only the accelerometer while the ankle system was subjected to an emulated step sequence consisting of three steps. It can be seen from Figure 5.4 that the shank angle is very noisy when the ankle makes contact with the surface and the change in force on the ankle system is high. This creates an acceleration which is measured by the accelerometer, which causes the noise in Figure 5.4.

To reduce the measured noise, the data must be filtered. Therefore, a complementary filtering system is used, by utilising the measured angular velocity of the gyroscope in combination with the acceleration measurements of the accelerometer. The complementary filter used was a simple weighted complementary filter in order to favour the instanta-

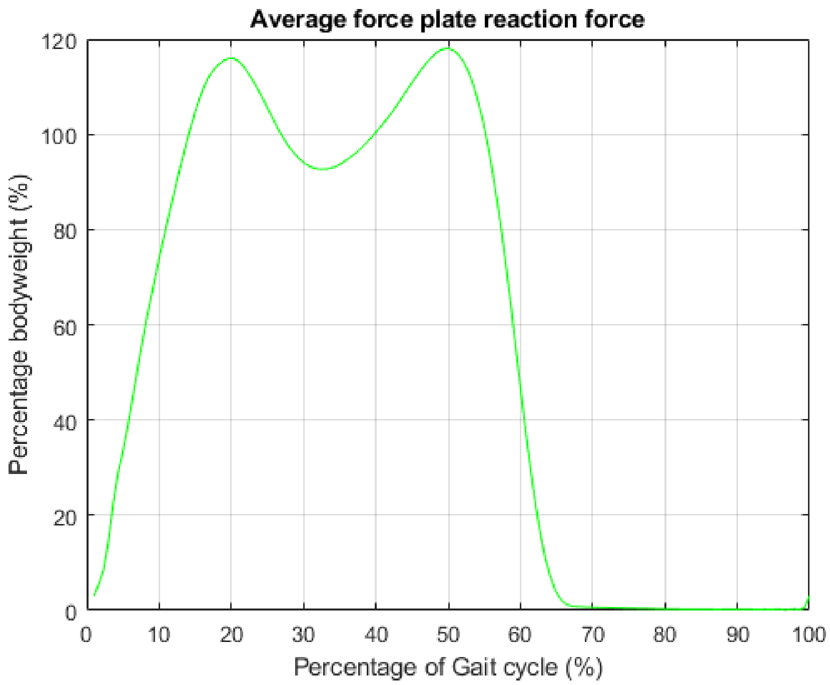

Figure 5.3: Averaged force plate reaction [13]

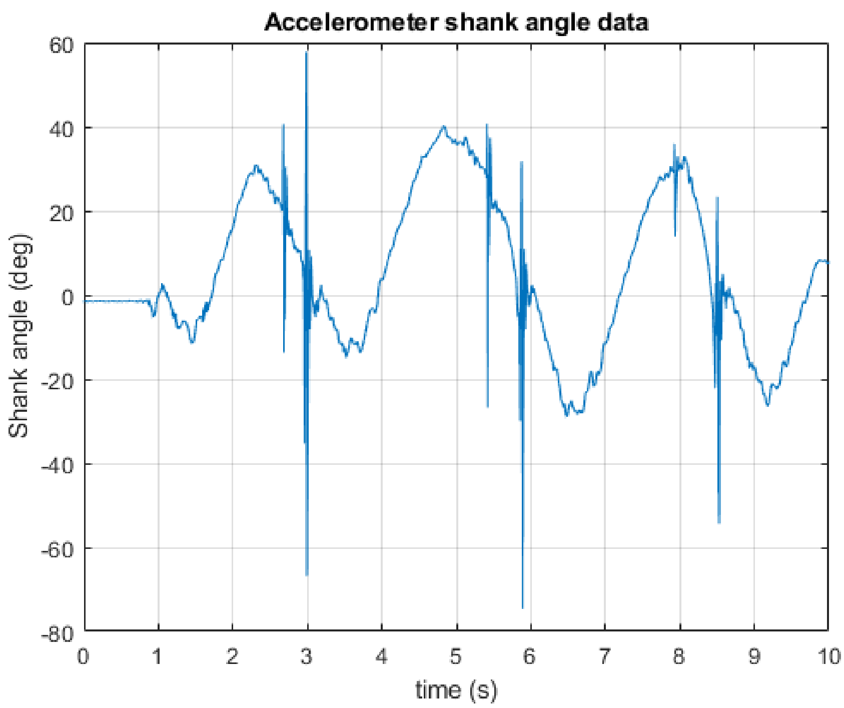

Figure 5.4: Accelerometer shank angle data

neous gyroscope angle measurements over the accelerometer angle measurements. This is because the gyroscopic angle measurements are subject to less high-frequency noise, while the accelerometer angle measurements are not subjected to time-varying drift at steady state, due to measurement inaccuracies being integrated over time when calculating the gyroscope angle measurement. As input this filter takes the accelerometer and gyroscope angles after a numerical low-pass filter is applied to both, with the cut-off frequency chosen to induce minimal system lag, while removing extreme high-frequency noise. These readings are then combined as in Equation 5.1, where G_S and A_S refer to the sagittal gyroscope and accelerometer angles respectively, the weights a and b are adjusted to favour the gyroscope readings.

$$\Theta_S = A_S \times a + G_S \times b \tag{5.1}$$

Since the gyroscope angle data is subject to drift, the gyroscope angle measurement is reset using the accelerometer angle, when the device detects that it is no longer in motion for half a second. This allowed for a simple, computationally light-weight solution that was found to be robust enough to yield accurate results with minimal noise for this application. Implementing this filter on the system and emulating three steps yields the results as displayed in Figure 5.5 below. The same experiment was conducted to display both the raw and filtered step data; however, since the system lag introduced by the filter is an important consideration, a new dataset was recorded with the complementary filter active on the prosthetic ankle system to verify that lag can be considered insignificant.

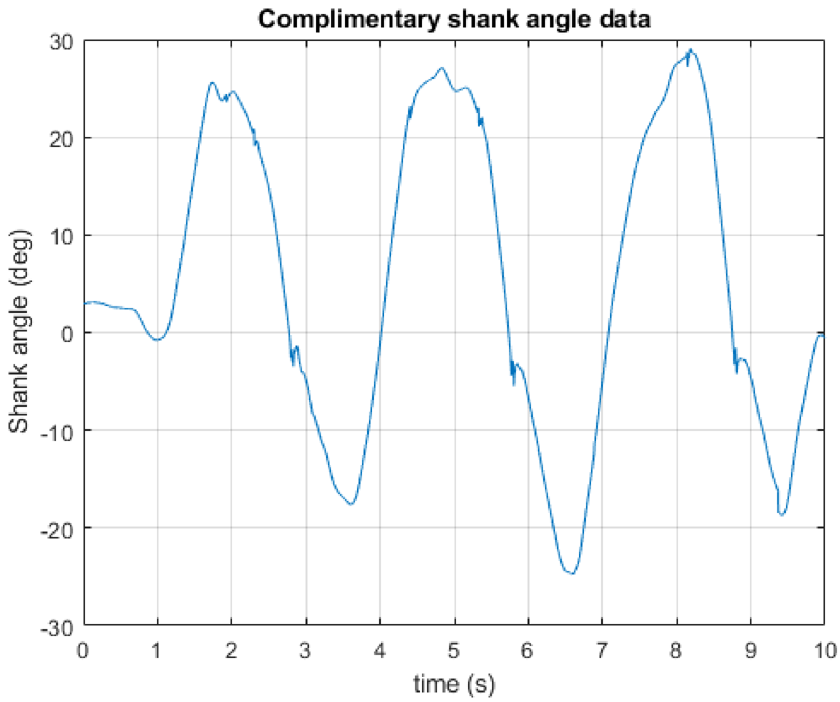

Figure 5.5: Complimentary shank angle data

In summary of the sensor implementation, the strain gauges implemented on the carbon foot blades as well as the shank angle measured by the IMU were implemented effectively, such that the required information can be measured by these sensor systems. The strain gauges are capable of accurately measuring the force on both the heel and toe blades, which allows the system to detect the gait events and estimate the state of the ankle system. The IMU system is implemented such that the shank angle can be accurately measured with minimal noise. This allows the system to measure the flat foot and toe off shank angles to classify the terrain based on the terrain classification system discussed in Section 4.4.

5.3 Power electronics design validation

This section aims to validate that the designed power electronics circuitry, designed in Section 4.3, performs as desired. This validation will be done by driving the motor under load of weight of the foot blade mount system, as well as only connected to the lead screw through the belt drive. When the motor is only connected to the lead screw through the belt drive, the motor will be considered to be under no load. The supply voltage is set at 16.8V from a lab bench power supply, this is to simulate the battery being fully loaded, with the addition of overcurrent protection in the event of a short circuit may occur during testing. An oscilloscope is used to measure the regulated voltage from the power supply, the input voltage, the gate voltage of the high side MOSFET and the voltage across the motor. This is done to measure the time taken to switch the high side MOSFET to verify the design parameters and measure the duty cycle retention, or signal integrity from the input to the MOSFET gate. As well as verify the design of the motor driver design as discussed in Section 4.3.

The voltage waveforms observed under no load during the test are shown in Figure 5.6 below. From Figure 5.6 it can be seen that the voltage on the gate of the high-side MOSFET rises to a voltage above zero while the MOSFET is supposed to be switched off. This is due to the fact that the back EMF of the motor feeds back through the bootstrap driver onto the gate of the high-side MOSFET.

This can be seen in Figure 5.7, where it is evident that when the motor is unloaded, the back EMF waveform of the motor corresponds to the gate voltage measured on the gate of the high-side MOSFET. This was also found in simulation when simulating a high back EMF, as discussed in Section 4.3. This is due to the fact that when the motor is switched off, the energy stored in the motor is not sufficiently discharged and reflects onto the gate voltage of the high-side MOSFET.

However, when the motor is loaded using the foot blade mounting system, the motor waveforms are quite different, as can be seen in Figure 5.8 below. As discussed previously, when the motor is loaded, the energy stored in the motor is more effectively discharged to the load and is therefore not reflected onto the gate voltage of the high-side MOSFET.

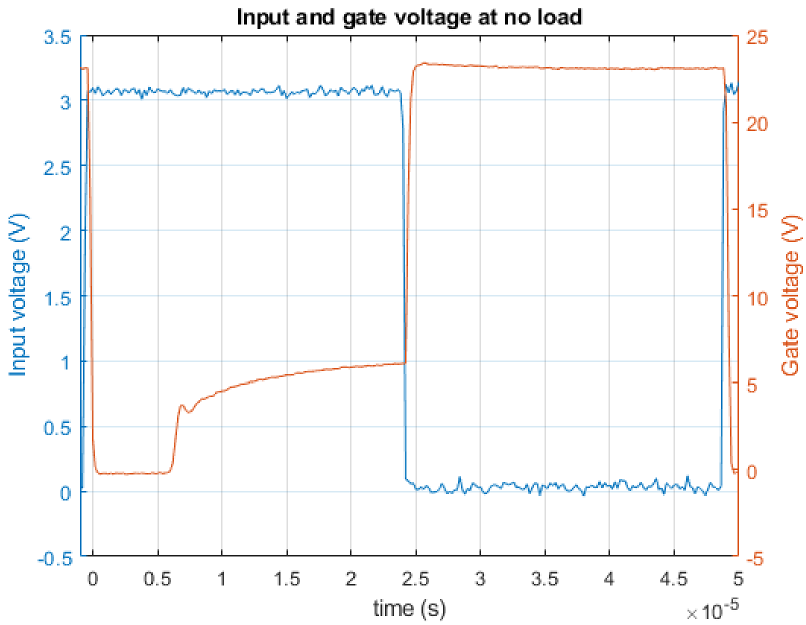

Figure 5.6: Motor driver waveforms unloaded

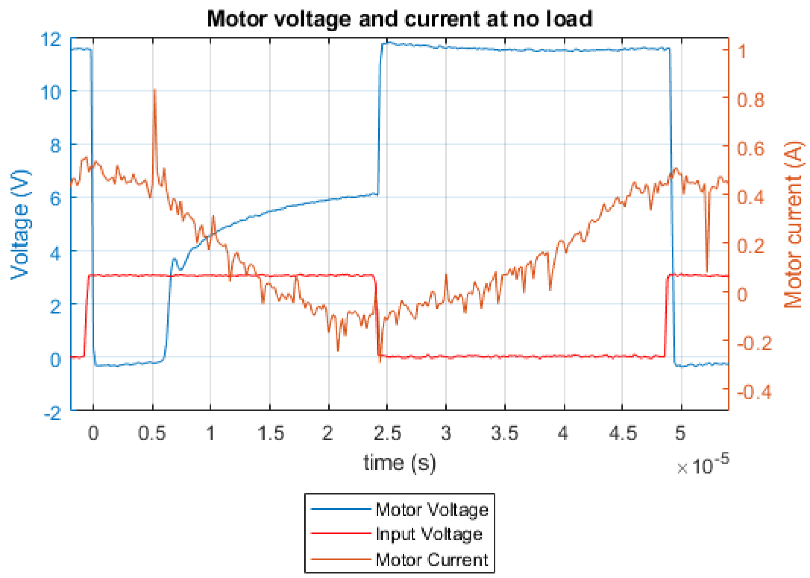

Figure 5.7: Motor waveforms unloaded

The turn-on time during the switching of the high-side MOSFET gate was measured to be 200 ns from Figure 5.8. Thus, the real switched duty cycle can be calculated as $D_{on} = \frac{t_{in} - 2 \times t_{on}}{T}$, where t_{in} refers to the on time of the input signals and t_{on} refers to the turn-on time of the high-side MOSFET. The real switched duty cycle is calculated as 49.2%, with an input duty cycle of 49.8%. This means that the real duty cycle output is 0.6% less than the input duty cycle at a switching frequency of 20 kHz, which is acceptable

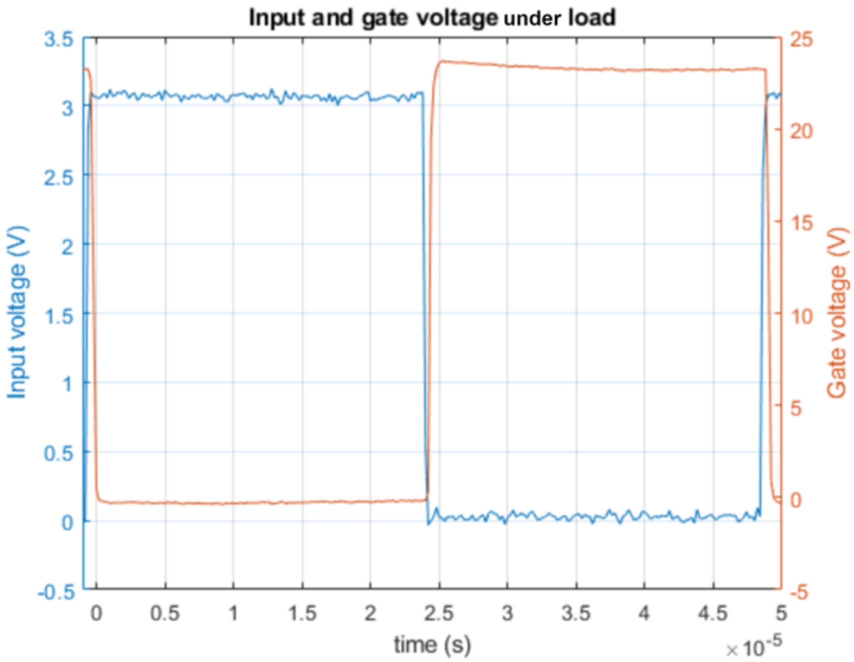

Figure 5.8: Gate driver waveforms under load

as this was found to have little effect on the control of the system.

Figure 5.9 below shows the motor waveforms under load. Two important conclusions can be drawn from Figure 5.9. As the motor current was measured on the input connection from the power supply, it can be seen that the motor current becomes negative, this means that the motor feeds back into the power supply. This means that the return path of the motor driver system is different from the design return path. This can happen is the forward voltage of the reverse biased diode of the high-side MOSFET is low enough and the back EMF is high enough. This is also evident from the fact that the motor voltage is slightly higher than the supply voltage immediately after the high-side MOSFET is turned on.

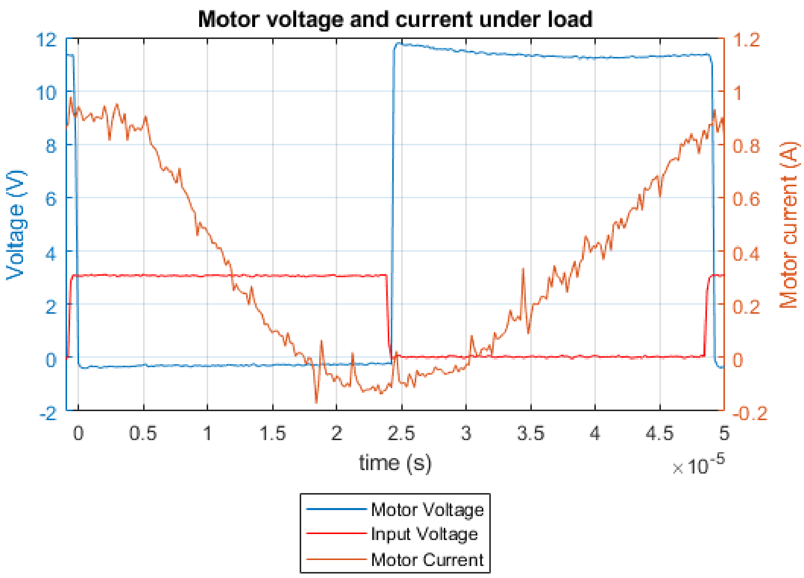

Figure 5.9: Loaded motor waveforms

This was found not to be a problem, as the output capacitance of the voltage regulator was capable of sinking this ripple current. Additionally, the voltage regulator switches at a frequency of 100 kHz, which means the voltage regulator was able to regulate the voltage effectively. Furthermore, the power supply ripple voltage from the voltage regulator, as well as the ripple voltage from the power supply, were both found to be 220 mV peak to peak, as can be seen in Figure 5.10.

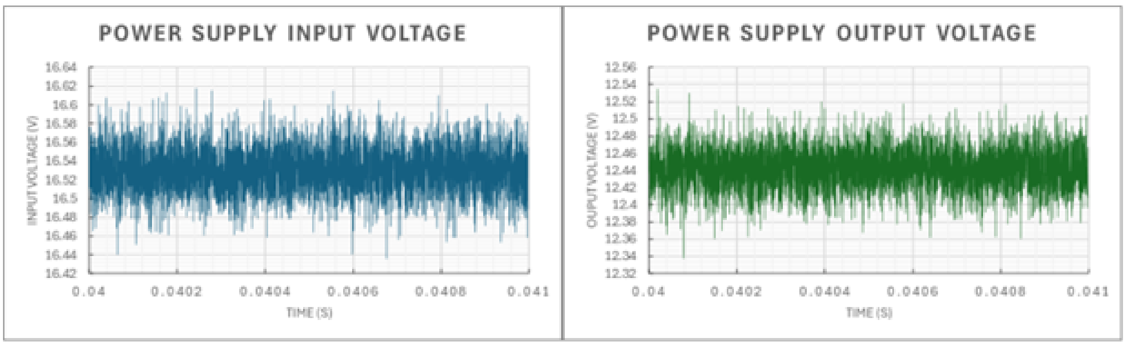

Figure 5.10: Voltage supply ripple

Investigating the frequency spectrum of the voltage regulator in reference to the lab bench power supply when driving the motor as can be seen in Figure 5.11, it can be seen that the frequency components of each are relatively equivalent. This can be due to the oscilloscope sampling frequency or inaccuracy introduced by the length of the probe wires. The input voltage in Figure 5.11 is shown in green, while the supply voltage from the power supply is shown in blue.

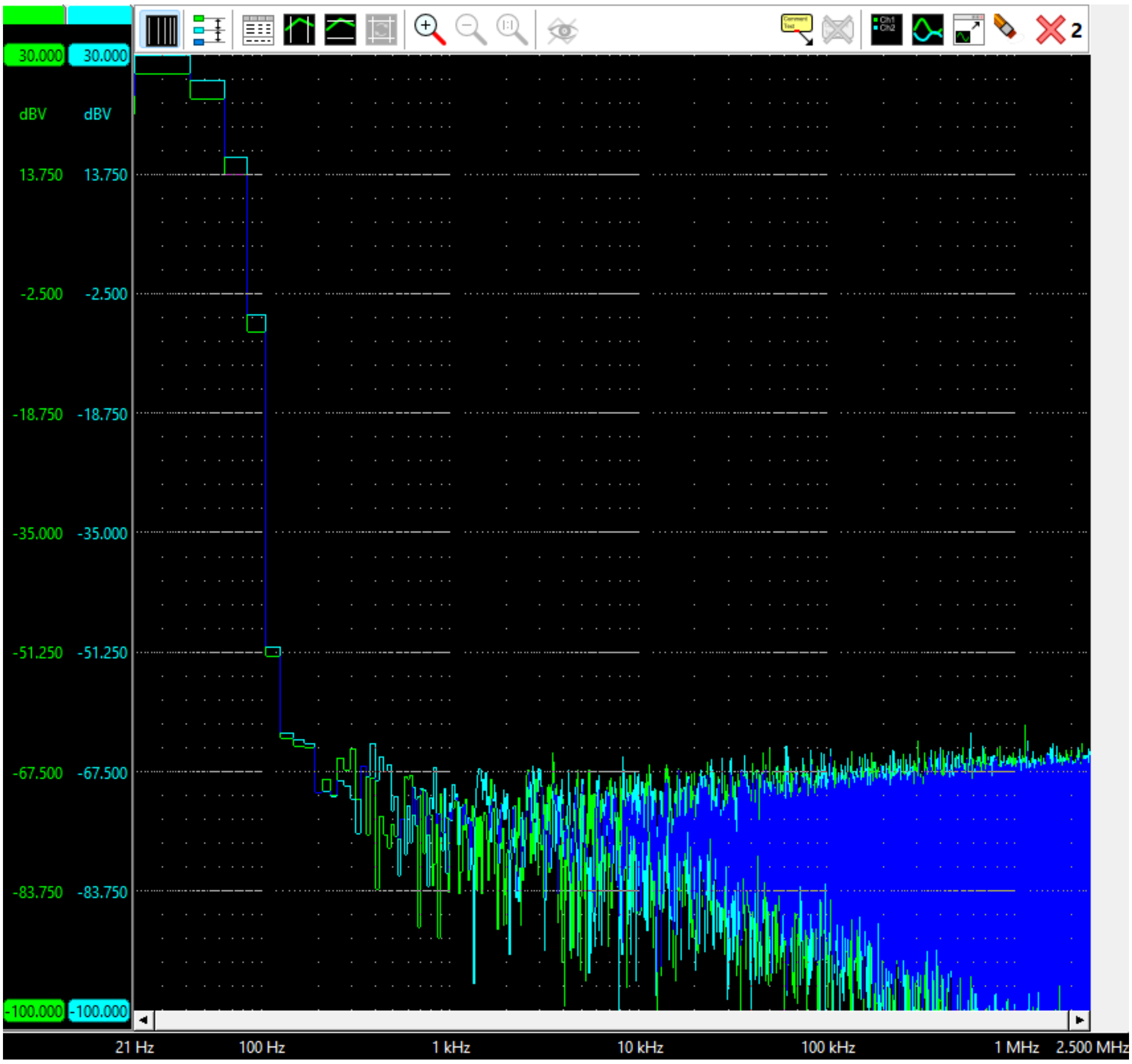

Figure 5.11: Voltage regulator FFT

Therefore, in summary, the motor driver system works well when the motor is loaded, and the loss in duty cycle is minimal at an operating frequency of 20 kHz. Therefore, the motor driver system can be said to be functional for this application. There are, however, unforeseen operating conditions, such as the motor feeding back into the power supply system. This effect is however not dangerous to the components as the output capacitance of the power regulator can handle this ripple current. Additionally, the power regulator system was found to be adequate, as the voltage remains stable under load from the motor, and the ripple voltage is equivalent to the ripple voltage of the power supply, as seen in Figure 5.11.

5.4 System model validation

This section validates the mathematical model derived in Section 4.4. The physical system was subjected to a 12 V step input, as is the rated voltage of the motor, as discussed in Section 4.3. A camera was set up on a test stand to capture the ankle position during each frame, as shown in Figure 5.12 below. A current clamp was also placed on the input to the motor to measure the current draw. Therefore, the mathematical step response can be compared to the experimental step response. Verifying parameters such as the steady-state ankle rotational velocity and the motor inrush current.

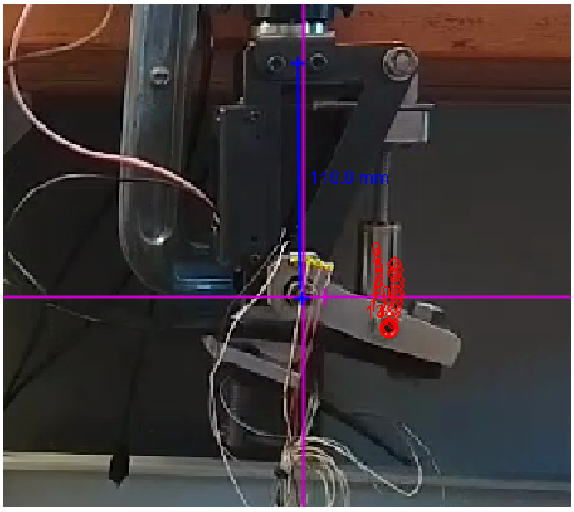

Figure 5.12: Step response of prosthetic ankle

The video file was then added to a visual pixel tracking software called Tracker. From the video, the ankle angle can be calculated by tracking the joint between the lead screw and the foot in every frame. Since the frame rate of the camera is known, the angular velocity can be calculated simply by performing a numerical differentiation of the ankle position. However, as the accuracy of the pixel position in each individual frame is subject to some amount of error, the angular speed is averaged while the ankle has reached steady state.

The mathematical model is derived in Section 4.4, where the constants for the mathematical model are either calculated, read from the motor data sheet or read from the model in Siemens NX version 1980. The results from subjecting the mathematical model to a 12 V step response are shown in Figure 5.13 below. The motor speed in RPM, armature current in amps, ankle speed in rad/s and ankle angle in rad is calculated by the mathematical model.

From the results of the mathematical model as shown in Figure 5.13, The ankle speed was found at steady state to be 2.277 rad/s which translates to 130.46 °/s. The inrush current was found to be 3.517 A in the mathematical model. The steady state current was found to be 185.4 mA in the mathematical model. Now, it is important to compare the

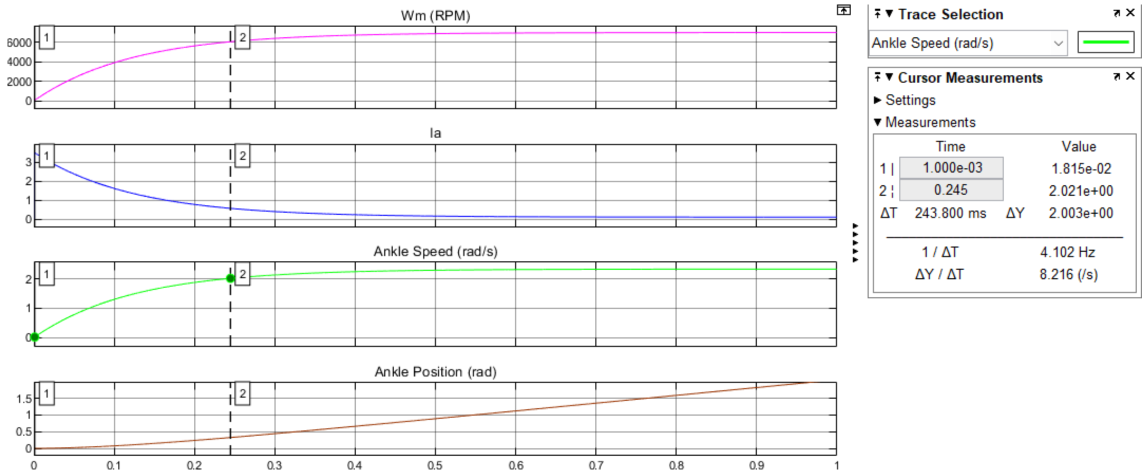

Figure 5.13: Mathematical model results

mathematical model to the response of the physical system. The physical test is conducted as previously described, since the model is not calculated at steady state and the simulation time and practical test times are different, the physical system will be compared to the mathematical model at a specific time. The results of the physical system subjected to a 12 V step input is shown in Figure 5.14 below.

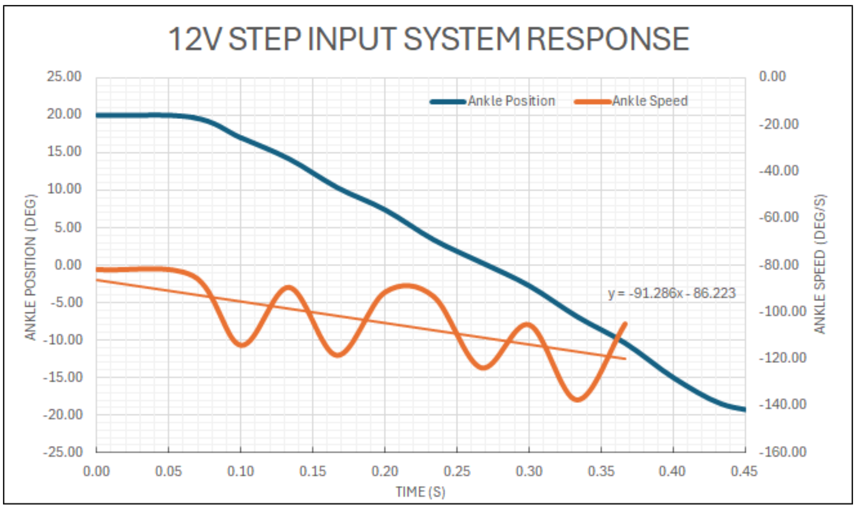

Figure 5.14: Physical system step response results

Due to the frame rate of the camera used for this experiment being suboptimal, the measurement accuracy of the pixel tracking software becomes too low to accurately measure the ankle speed curve. However, the speed at a specific time can still be calculated, by using the trend line of the data. The position of the ankle was captured by tracking the pixel of the moving joint in relation to the ankle joint, as previously discussed. The speed is then found by numerically differentiating the measured position using the known frame rate of the camera, in this case 30 FPS. The input current was also captured, as mentioned previously, by utilizing a current clamp and an oscilloscope. This data was then digitally filtered, and the results are shown in Figure 5.15 below.

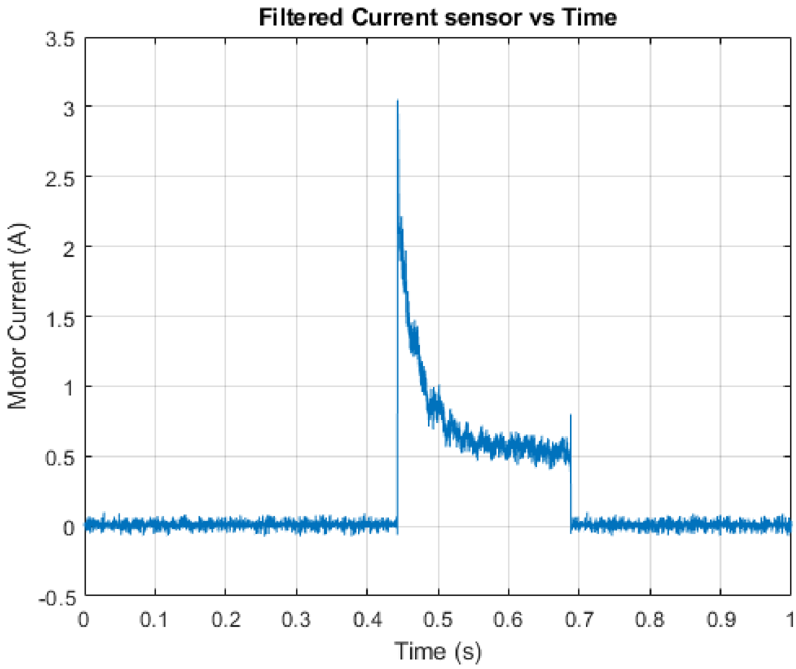

Figure 5.15: Step response motor current

Comparing the mathematical model to the experimental results can be done at specific timestamps to verify the accuracy of the model. The step response duration can be calculated from the motor current, as shown in Figure 5.15 and was found to be 0.245 s. Therefore, the calculated motor current at 0.245 s will be compared to the experimentally determined motor current at 0.245 s. The experimental motor current was found to be 556 mA at 0.245 s, whereas the mathematical model calculated a motor current of 569.1 mA at 0.245 s. The measured ankle speed using the trend line equation from the recorded data is 108.49 °/s at 0.245 s, while the calculated ankle speed at 0.245 s is 115.79 °/s. From the results of this test, it can be safely concluded that the mathematical model is accurate enough for the purposes of control system design.

5.5 Position control validation

This section aims to validate the most essential subsystem of the low-cost terrain-adaptive ankle. A PID position controller was designed in Section 4.4 and will be tested to verify the design and implement a working controller. Two primary tests are conducted to validate the working of the implemented controller. Firstly, the controller will be tested against a step input, such that the overshoot, settling time and steady state error can be used as metrics against which the performance can be measured. Secondly, the controller will be subjected to a ramp motion profile, similar to what it will be subjected to during operation. This is done to measure the dynamic response and validate that the controller will be able to follow such a motion profile in real time to a satisfactory level of accuracy.

5.5.1 Testing step response

The step response is a common benchmark used for evaluating the performance of many different types of control strategies. This is because the steady-state error, overshoot and settling time can be read easily from the sensor data. These metrics can be used to evaluate the performance in comparison to other controllers or tuning parameters.

The PID controller to control the ankle position was designed in Section 4.4, during implementation it was found that the designed controller was capable of controlling the system. However, the implemented designed controller was judged to have an excessive overshoot, therefore the controller was tuned using the Ziegler-Nichols PID controller tuning technique. This tuning technique entails setting the integral and derivative gain to zero, then increasing the proportional gain until the ultimate gain is found. At this point, when subjugated to a step input, the system will oscillate about the set point at the characteristic frequency, as show in Figure 5.16. The ultimate gain, at which the system is unstable, as well as the oscillation frequency is used to determine the tuned proportional, integral and differential constants. The Y-axis of Figure 5.16 is the rotary encoder step value, where there are 2048 steps in one rotation of the ankle about the ankle joint.

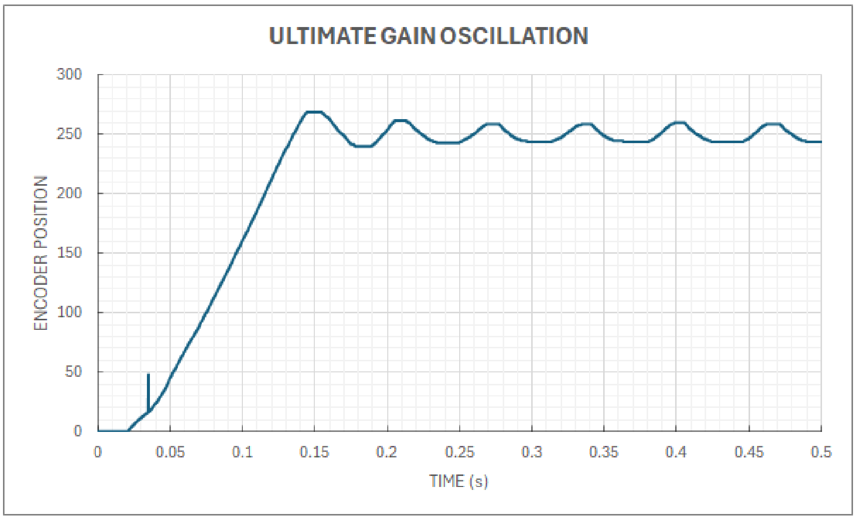

Figure 5.16: Oscillation at ultimate gain

After tuning the controller using the Ziegler-Nichols PID controller tuning method, the controller constants were finalised. The step response was recorded by utilizing the serial wire View functionality in the STM32 CubeIDE, thereby outputting the sensor data to the computer in the debugging environment. A step corresponding to 21 degrees was given to the position controller, Figure 5.17 displays the raw encoder data recorded in the step response.

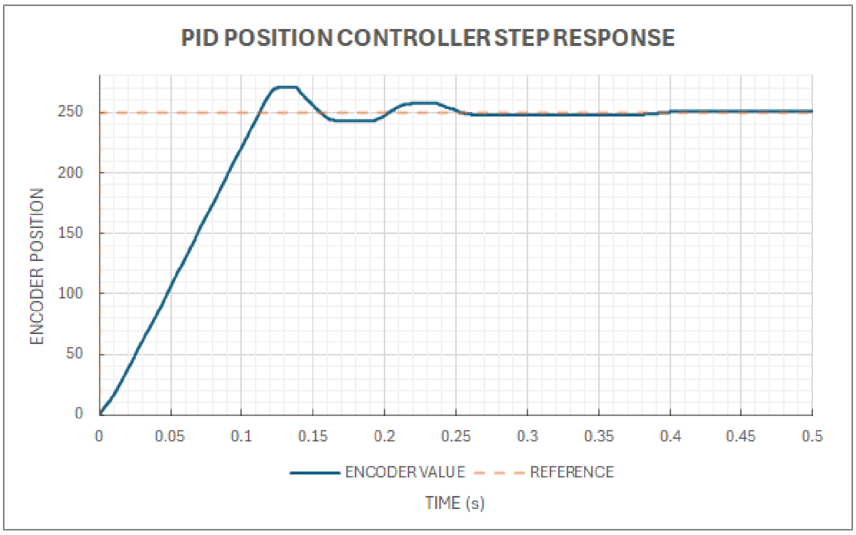

Figure 5.17: Step response for position controller

From the data recorded in the step response test, it was found the system overshoot was 8.4%, while the settling time and steady-state error were 0.254 and 0% respectively. The parameters for the tuned PID position controller were as follows, proportional gain is 0.5882, integral gain is 0.0385 and derivative gain is 0.096.

The mathematically designed PID position controller performed somewhat differently to the implemented PID controller, as can be seen in Figure 4.27. The PID position controller mathematically designed in Section 4.4 assumes a sampling frequency of 10 kHz and linearized friction model. After the implementation of the sensors, consisting of the strain gauges on the blades and the IMU and the digital filtering of the sensor signals, the sampling frequency may have dropped below the assumed 10 kHz. This in combination with the non-linearity of the real friction in the system explains the difference between the designed PID position controller and the implemented controller.

5.5.2 Testing ramp response

Testing the ramp response is important, because the motion profile of the position control system in the swing phase will be set using a ramp response. The step cadence of 1.18 s was found to be the average for healthy individuals walking at 1 m/s from data collected by Embry et al. [13]. Therefore, a step duration of 1 s was chosen for this test. Additionally, because the swing phase is typically around 40% of the stance phase, a duration of 0.4 s was assigned to the swing phase to test the ramp response. The purpose of this test is to validate whether the position controller will be able to accurately follow a determined motion profile such that increased MTC can be reliably achieved.

Similar to the step response test in Section 5.5.1, the rotary encoder position is transmitted via the Serial Wire Viewer in the STM32 CubeIDE. Figure 5.18 below shows the results recorded for the ramp response test of the system.

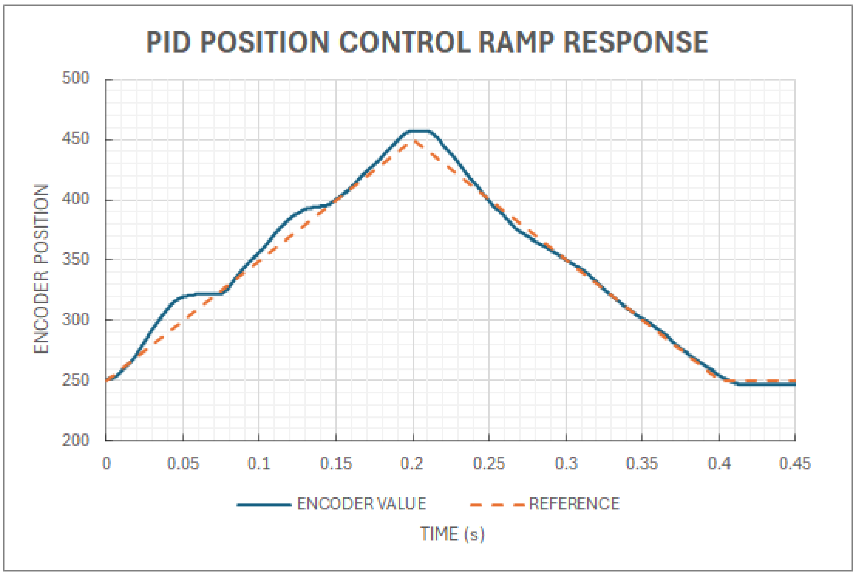

Figure 5.18: Measured ramp response for position controller

An oscillation can be observed when analysing the ramp position response in relation to the given reference signal. This is due to the nonlinear static friction that is neglected during the modelling of the system and it's effects can be seen here since the chosen brushed DC motor does not output maximum torque at a small output signal from the position controller. However, the system is able to follow a motion profile within a reasonable time as seen in Figure 5.18 and is therefore fit to output a motion profile during the swing phase to increase the MTC and increase stance phase stability. Now that the output of the system has been validated, the different aspects of the system, such as the sensor systems and control architecture, must be integrated to validate the design of the complete system.

5.6 Test bench system validation

In this section the designed prosthetic ankle is tested by fastening the prosthetic ankle to the test bench and simulating 5 normal steps at a level incline at 0.5m/s. The same process is repeated for a commercial ESAR foot, for comparison. The aim of this test is therefore to empirically validate whether there is indeed an increase in MTC and stability provided by the prosthetic ankle as opposed to a commercial alternative.

The test bench design is briefly covered in Appendix 6.3. In order to test the ankle on a moving surface simulating a step sequence, the test bench incorporates a moving hip motor to simulate hip torque and movement provided by a human during the gait cycle and is programmed to move with averaged angular position data as collected by Embry et al. [13]. To simulate the reaction forces between a surface and the prosthetic ankle when used by an actual human user, a moving treadmill is incorporated into the test bench. This allows for testing at different walking speeds and was intended to test different inclination settings as well. Therefore, to be able to test the prosthetic ankle in the test bench, a prosthetic knee is required as well, and it is assumed that the test bench setup will function similarly to a human user to validate the design requirements.

The testing methodology is as follows: the toe clearance and stability are tracked using a high-resolution camera mounted to the side to provide a good view of the prosthetic leg's movement during the test. The treadmill speed and inclination were the same for both tests; however, the individual mounting position of the commercial ESAR foot had to be adjusted to allow enough toe clearance over the treadmill during the swing phase. Both prosthetic feet were tested at 0.5 m/s and at an incline of 0 degrees with respect to the horizontal. An Össur 3R80 passive hydraulic knee was used for both prosthetic feet. The custom designed test bench as shown in Appendix 6.3 and used for this test can only approximate the movement of an amputee while walking, as it outputs only the hip movement and not any of the other compensatory movements, such as lifting of the hip to provide toe clearance. This is, because the hip output movement is provided by a motor through a belt speed reduction system, whose vertical position is set at the beginning of the test. This vertical position does not move during the duration of the test.

Using the high resolution camera, the stance phase gait of the prosthetic ankle was able to be properly captured. Figure 5.19 below shows the prosthetic ankle and test bench setup during three key stance phase events. Namely, heel strike, flat foot and toe off as discussed in Section 2.2. From Figure 5.19 it can be seen that during flat-foot, the prosthetic ankle is able to be placed firmly on the treadmill surface with both the heel and toe blades, this allows the friction between the treadmill surface and the prosthetic ankle to be maximized.

In comparison to the designed prosthetic ankle, the commercial ESAR foot has less stance phase stability as shown in Figure 5.20 below. Several differences can be observed and discussed between the commercial ESAR foot and the designed prosthetic ankle. Firstly, it can be seen that the foot does not make complete contact with the surface during Flat-Foot. This is due to the mounting of the foot to be able to clear the surface. To be able to clear the surface, the carbon leaf spring is loaded during what would be part of the swing phase, until the foot can kick forward in the swing phase.

When the commercial ESAR prosthetic foot is mounted to make more contact with the surface during the stance phase, the foot is unable to clear the surface during the swing phase. This is due to the fact that the commercial ESAR foot is unable to actively lift the toe and the test bench does not create compensatory movement to provide sufficient MTC to clear the test bench surface. This can be seen in Figure 5.21, however with the

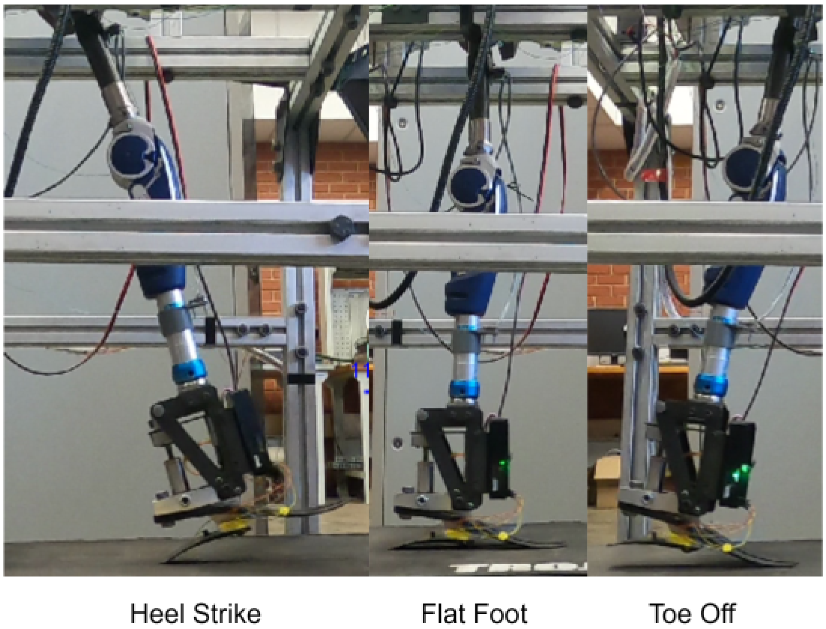

Figure 5.19: Stance phase ankle stability during test

ESAR foot mounted correctly the stance phase can be seen in Figure 5.20.

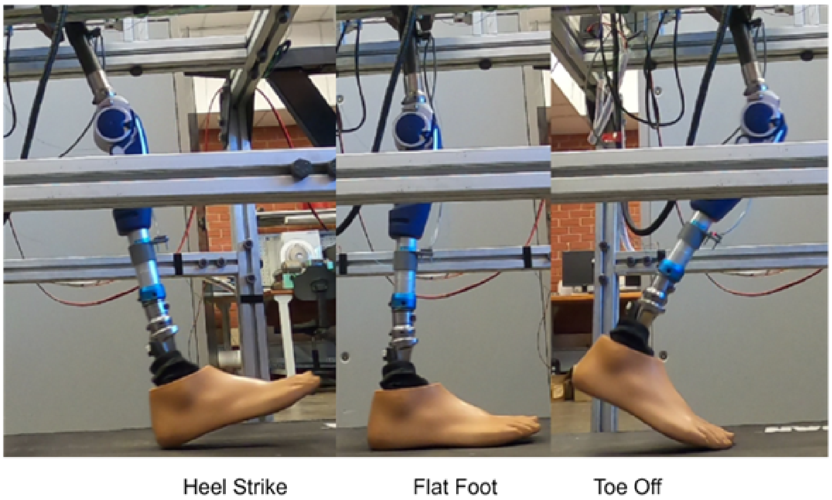

Figure 5.20: ESAR stance phase stability during test

Analysis of the knee angles during the test can be used to analyse the effects of the different prosthetic feet during the gait cycle. As the hip angle inputs are common through each of the prosthetic feet, the knee angles can be used to analyse the effect of the different prosthetic feet on the gait cycle. Figure 5.21 shows the normalised knee angles with different prosthetic feet.

It can be observed from Figure 5.21, that when the commercial ESAR foot is mounted

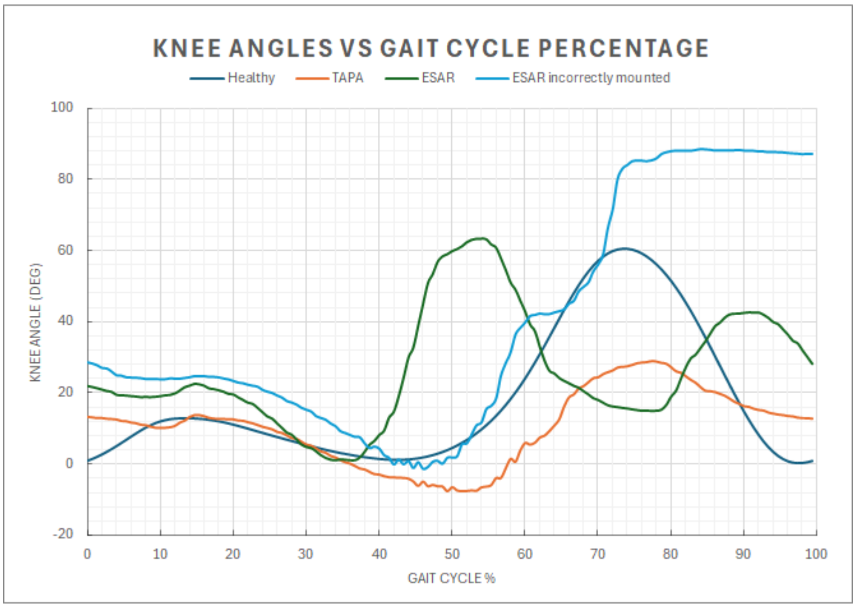

Figure 5.21: Knee angles using different prosthetic feet

incorrectly, the foot is unable to clear the surface and the knee remains bent during the swing phase. Similarly, it can be observed that when the commercial ESAR foot is mounted such that the foot is able to clear the surface, the knee is bent before toe-off, loading the foot. This creates a strange knee angle profile, in comparison to the knee angle observed from a healthy individual as measured by Embry et al. [13], which is provided in Figure 5.21. This also creates a shorter and more energetic swing phase that kicks the prosthetic foot forward due to the stored spring energy being released in the swing phase. In comparison, the designed terrain-adaptive prosthetic ankle, denoted by (TAPA) in Figure 5.21, creates a knee profile more similar to the knee angle profile by a healthy individual.

The surface of the test bench consists of a treadmill, see Appendix 6.3. This means that the ESAR prosthetic foot needs to be mounted with an upward tilt in order for the toe to clear the test bench. However, the length of the ESAR foot is also quite long to allow more energy storage in the foot blade. The ESAR foot also cannot intrinsically provide toe lift to assist the foot in clearing the surface of the test bench during the swing phase. This causes the swing phase to be initiated by the knee only, as the test bench is not designed to mimic amputee compensatory movements, as discussed in Section 2.3. When an amputee wears an ESAR prosthetic, the amputee typically lifts their hip to allow for additional toe clearance during the swing phase. However, since the test bench cannot do this, the swing phase is only initiated once the knee is bent forward to such a degree that the prosthetic foot releases all the stored elastic energy and kicks forward, as can be seen in Figures 5.22 and 5.21.

Additionally, the momentum of the prosthetic foot after being kicked forward causes the knee to bend before making contact with the surface of the test bench. This can be seen in the second local maximum of Figure 5.21 for the ESAR prosthetic foot.

In comparison, the terrain-adaptive prosthetic ankle has a carbon blade with lower stiffness and is capable of initiating the toe clearance. Meaning, the stored energy is less, and the foot can begin the swing phase sooner in the gait cycle. However, the design of the carbon blades was outside the scope of this project. The reason the knee angles of the designed prosthetic ankle correspond closely with that of a natural knee is because the designed prosthetic ankle can provide toe clearance early in the swing phase where the ESAR prosthetic foot cannot. However, during the swing phase, the knee angle is much less bent than a natural knee, as can be seen in Figure 5.21. This is because a natural leg has the functionality of the hamstring muscles to bend the knee into flexion, which the prosthetic knee on the test bench does not have.

For a more intuitive visualisation of the gait cycle differences between the commercial ESAR and designed prosthetic ankle, a series of screen captures are provided below in Figure 5.22. Figure 5.22 can be used as a reference to verify the knee angles in Figure 5.21 and the previous discussions to the reader.

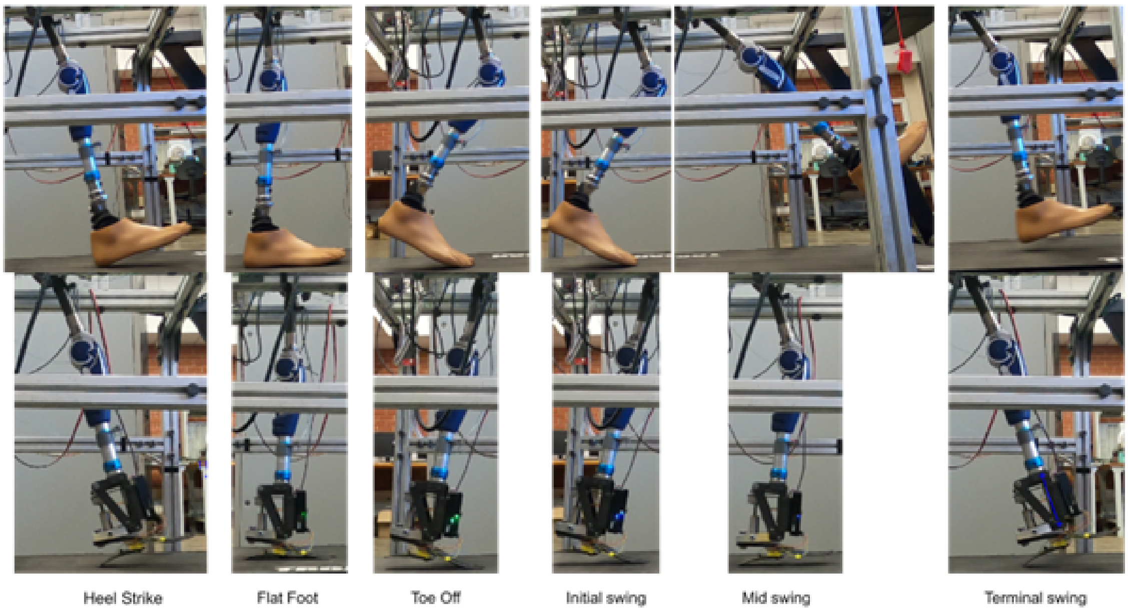

Figure 5.22: Visual gait cycle differences

Next, the toe clearance will be discussed, as improved MTC was one of the design outcomes discussed in Section 3.2. Immediately from Figure 5.22, it is possible to see that the prosthetic ankle does indeed actuate as intended during the swing phase. This along with the increased similarity to a natural knee during the gait cycle when using the designed prosthetic ankle is already promising. Figure 5.23 below shows toe vertical toe clearance for both the designed terrain-adaptive prosthetic ankle (TAPA) and the commercial ESAR foot.

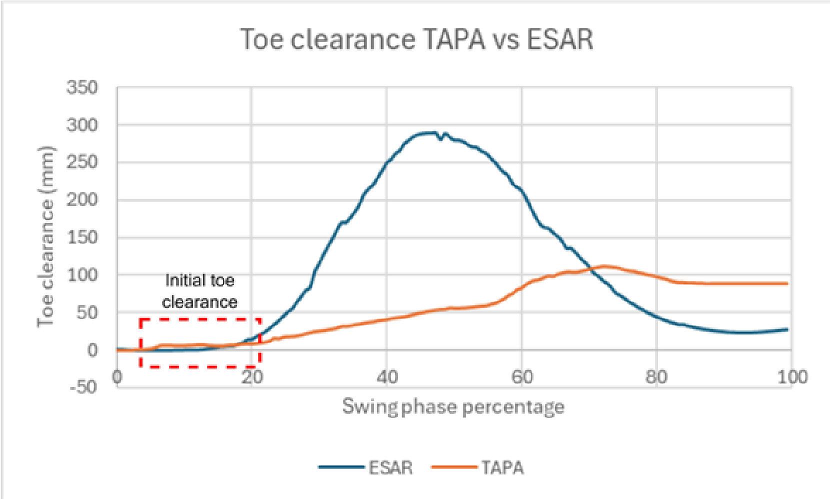

Figure 5.23: Toe clearance during swing phase

It can be seen that initially, during the first 4-20% of the swing phase, the designed prosthetic ankle is able to increase the toe clearance to >6 mm above the surface. This is significant in comparison to the commercial ESAR ankle which barely clears the surface with a toe clearance of less than 1 mm during this time. This was calculated using pixel tracking software, and the initial clearance of the toe allows for a higher probability of the toe to clear the surface of the test bench.

The effects of the actuation of the prosthetic ankle are further discussed in Chapter 6. However, from the measurements conducted while the prosthetic ankle system was traversing the test bench, it can be said that the prosthetic ankle functions as designed. The effects of an active dorsiflexion prosthetic ankle have been researched by Rosenblatt et al. [35], as discussed in Section 2.3. Proving that the designed prosthetic ankle can indeed function as an active dorsiflexion prosthetic ankle means that it should be beneficial for amputees in theory; however, this would have to be studied to prove definitively, as will be discussed in Chapter 6.

5.7 Cost evaluation of the system

The prosthetic ankle system manufacturing cost is shown in Figure 5.24, where the pie chart displays the estimated cost associated with the development of the prosthetic ankle. The total cost of the ankle can be calculated at R8340,00. This means the ankle system can be constructed very cost effectively, where the commercial prosthetic ankles of this type of functionality can be expected to be in the range of R100 000,00-R300 000,00.

Therefore, the prosthetic ankle achieves the goal of being cost-effective in comparison to the commercially available prosthetic ankle. Therefore, if this project were to be further

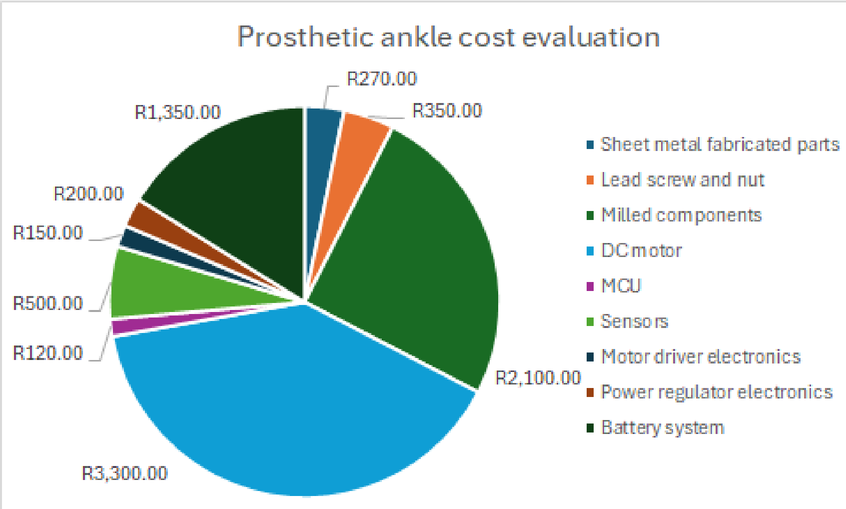

Figure 5.24: Prosthetic ankle cost evaluation

developed to decrease the weaknesses of the design that will be further discussed in the coming section, a low-cost alternative can be delivered to amputees in poverty-stricken areas and lower income regions.

5.8 Summary of system verification and validation

In summary of the system implementation, from mechanical design implementation to control of the ankle on a level surface, the ankle system works as it was designed. However, the ankle system could not be tested on inclines, due to time constraints and the intricacies of making the test bench emulate incline walking. As will be discussed in the following chapter, the system can still be said to be terrain adaptable, as the classification system is designed, and the control system is capable of this implementation. The cost involved with the manufacturing of the prototype was also discussed and, it was found that the prototype vastly more cost-effective than the commercial alternative with a similar functionality.

In the following chapter, the system that was designed and implemented throughout this paper will be critically evaluated. Based on the cost of construction and the performance when tested at a subsystem level and when testing the system as a whole.

Chapter 6

Conclusions and recommendations

6.1 Introduction

This chapter will focus on summarising the experimental results as discussed in Chapter 5 and will focus on successes and failures of the project, including discussing the validity of some of the key design decisions made throughout the design process. The future work discussion will aim to provide a basis from which the project can be improved as well as providing recommendations for others who wish to design similar systems.

As the system designed has high-level design outcomes, the system must be evaluated based on high-level functionality. However, since the system was designed in detail, the evaluation will include reasoning based on the characteristic functionality of the subsystems that make up the prosthetic ankle system.

6.2 Conclusions drawn from experimental results

As seen in Section 5.6, the prosthetic ankle system was tested on a level terrain incline at a walking speed of 0.5 m/s, which is within the typical walking speed range for an amputee. The prosthetic ankle system functioned as designed, with the prosthetic ankle system being capable of providing toe lift and mechanical stability when it was required. The prosthetic ankle system was also capable of accurately detecting the gait events, allowing the prosthetic ankle system to properly actuate when needed.

Additionally, based on the results seen in Figure 5.21, it can be observed that the prosthetic knee angles using the designed prosthetic ankle are similar to those of a healthy knee, rather than the prosthetic knee angles when using a passive prosthetic foot. This echoes the sentiment recorded by Rosenblatt et al [35]. However, to definitively say that the prosthetic ankle designed in this study will decrease the likelihood of tripping and slipping, a study on a human pilot is needed.

The terrain classification system could not be tested, due to the time it would require to make the test bench approximate the human gait at inclined surfaces. This would then require additional time to iteratively collect data of the prosthetic ankle system walking on the inclines to recalculate and retrain the classification system. However, the prosthetic ankle system can still be said to be terrain-adaptive, as the system is mechanically capable of adapting to terrain and the electrical and electronic system is capable of processing and actuating the system to adapt to the terrain and a terrain classification system was designed. However, the terrain classification system was designed using data recorded from healthy humans and as such will not transfer to an amputee using the system.

Therefore, considering the discussion above and assuming the test bench accurately represents a human user, the prosthetic ankle system is capable of both increasing the MTC during the swing phase and increasing the stability during the stance phase by applying a larger contact area to the surface in comparison to a ESAR prosthetic foot. However, the prosthetic ankle system is currently incapable of adapting to terrain and therefore, to achieve this functionality, data must be recorded from the sensors. This can be done using a bluetooth module capable of serial communication, since the electronics are designed to be capable of connecting to such a module for the purposes of data logging.

The lower level systems, such as the mechanical subsystem, was found to function as desired and is capable of providing stance phase stability. However, the fact that the lead screw system was used to keep the overall system cost low, the lead screw and nut interface is the main source of backlash of the system. This backlash creates an area of involuntary control where the ankle angle is defined by the external forces and can not be controlled by the prosthetic ankle. This effect is negligible since this area is very small; however, this may also cause larger shock loads that could lead to mechanical failure of the lead screw or nut due to fatigue.

Additionally, as seen in Figure 5.18, the friction of the system is too much to be overcome by the motor at small control output signals, which can cause an uneven response. This effect is again negligible as the amount of deviation measured is minimal, however this could be decreased by using a different motor topology. The microcontroller used and the power regulator systems can be optimised to have an overall smaller footprint on the PCB. This can cause the overall system to be less complex, as these components were chosen to optimise for cost and hand solderability.

A belt transmission system to transfer the rotational mechanical power to the lead screw would not be necessary if the lead screw system forms part of the rotor of the motor. With such a configuration, the system size can be shrunk and thus the overall weight of the system can be decreased. Such a system can be beneficial from the users' perspective, however this would increase the cost of the system.

From the motor driver system results discussed in Section 5.3, it can be seen that the motor driver system performs well under load; however, when the motor is unloaded, the motor driver system performs worse than desired. This effect can be mitigated by choosing a motor driver system that does not feed the motor voltage back onto the high-side MOSFET gate. This can be achieved by using a P-channel high-side MOSFET or a transformer-coupled MOSFET gate driver.

The sensor systems are found to be sufficient, as a robust integrated solution can be constructed using the chosen proprioceptive sensors. This sensor system can be said to be robust, as the sensor system is unimpeded by clothing and surface reflectiveness, as exteroceptive sensor systems are. The shank angle was found to be robust against the shock loads induced by walking on a surface, as can be seen in Figure 5.5. Additionally, the sensor systems can be said to provide enough data for terrain classification and state estimation, as seen by the accuracy of the terrain classifiers in Section 4.4.

The system was also found to be extremely low-cost in comparison to commercial alternatives. This may be due to the business model of these prosthetic companies, since there may be too few prosthetics being sold to allow for a low price point. However, if this is the case, the prosthetic ankle designed in this dissertation may still be refined and distributed to amputees, as the price for one unit is in the range of a passive ESAR prosthetic ankle.

6.3 Recommendations for future work

For the system to be a viable commercial product, a few flaws should be addressed, either by re-evaluating certain design choices or by finalising the prototype into a robust, fully functioning product.

Firstly, from a system-level function point of view, the classification system should be updated to make the system terrain-adaptive. It can also be updated to detect a wider range of terrains; inclines create a significant challenge for amputees; however, stairs create similar issues. The optimal actuation technique for assisting the amputee during stair ascent and descent was not covered in this dissertation. However, since the electromechanical system is already constructed and the actuation profile can be easily changed in code, the ankle system can be used to gather shank angle data of an amputee when traversing an obstacle.

This data can then be used to build an LDA classifier using the shank angle at toe-off and the shank angle at flat foot, as discussed in Section 4.4. This classifier will need to be different for each user, as the ranges of these values will vary between amputees, due to differences in preferred walking speeds and individual limb lengths, as can be seen in

Figure 4.28. Then, the actuation profile can be adapted to find the optimal actuation profile for each different scenario.

Once the different actuation profiles and types of terrains have been decided upon, the classification system should be implemented for one user creating a specific case. Then, when another user wants to use the system, the system should be adapted to this user, this can be done either automatically, or it can be done in a lab to optimise for a new pilot. If it becomes desirable to automate the adaptability from user to user, it may be prudent to invest in an embedded machine learning algorithm. This may mean that the chosen MCU may be insufficient to run the machine learning algorithm to optimise the classification system and run the ankle system concurrently. However, it may be possible to run the machine learning optimisation of the terrain classification only during the adaptation of the prosthetic ankle to a new user.

However, recording shank angle data for a new user to create a terrain classification system is not as simple as it may seem. This is because, the output of the ankle system will have an effect on the walking mode of the user. The user can be seen as a very complex multiple input, multiple output feedback system, while the prosthetic ankle system is also a feedback system that should not negatively impact the walking gait of the amputee. This can happen if the output of the prosthetic ankle does not create the appropriate base of support for the amputee, or impedes the swing phase of the gait cycle. Therefore, when recording data of the amputee, the ankle system must perform the same for each trial initially, then a first iteration of the terrain classification must be constructed. The amputee should then become familiar with the dynamics of the ankle on the first iteration terrain classifier, before the data can be rerecorded and another iteration can be constructed. This should be done until no further changes in the shank angle variables at different terrains are observed. This can be done with machine learning to optimise the adaptation of the classification system to the amputee.

Evaluating the mechanical subsystem, the mechanical subsystem was found to be sufficient to support the user during the stance phase and was cost-effective to manufacture. However, the mechanical subsystem is rather heavy, as the entire system was found to be around 1.8 kg. This is within the range of other prosthetic ankles with similar functionality, however the mechanical subsystem can be constructed using high strength composites to reduce the overall system weight. A large portion of the weight of the system comes from the chassis being made out of laser cut 3 mm thick sheet metal. This can be made out of a carbon composite as opposed to sheet metal to reduce the overall system weight. However, this may increase the overall system cost, as cost-effectiveness is a key design requirement of this system. Therefore, the weight of the system should be weighed against the increased cost of the system.

Additionally, the lead screw system was found to introduce backlash in the system. This is to be expected, as there exists a machining tolerance between the nut and the screw, such that the lead screw is not in contact to both faces of the lead nut. This effect is negated in ball screw systems, because the ball screws use ball bearings in the nut housing, such that both faces of the ball nut are in contact with the screw. However, such systems are much more expensive than lead screw systems, this is due to the mechanical manufacturing tolerances required. Therefore, if this were to be implemented, the better performance needs to be weighed against the increase in overall system cost.

Some of the other mechanical components, such as the placements of the bearings in the bearing housing, can be revised and optimised. To better constrain the lead screw around a point, the lead screw nut was constrained using bearings in the bearing housing, as seen in Figure 4.8. The lead screw then also is used as a shaft to seat a pulley, however in order to seat the pulley, a slot is cut into the lead screw and a key is inserted. However, this system must seat a pulley, must be constrained with bearings and interact with a nut. To achieve a better mechanical construction, a custom shaft can be cut on a lathe with higher tolerances to seat the bearings and pulley. The lead screw profile should then be cut into the same shaft. However, once again, this will increase the overall system cost and should be weighed against the increased performance.

Or, alternatively, if a ball screw system is preferred, the ball screw itself should be altered to seat the bearings and pulleys. This can be done by turning down the ball threads on the screw to a specific tolerance to properly seat the bearings. The same can be done to seat the pulleys. However, a shaft collar or similar system can then be used to constrain the shaft in the vertical direction.

Therefore, as discussed above, the mechanical system can definitely be improved to achieve a lower backlash and lower overall system weight. However, this will come at an increased cost as the higher quality components and alterations made to components will require additional machining time. Additionally, the lead and ball screws may be made of a hardened steel, meaning cutting a profile onto the screw may prove to be an expensive task.

Finally, the blades of the mechanical system must be discussed, as the blades used were taken from another commercial prosthetic ankle and are not necessarily optimal for this application. Therefore, dedicated carbon blades should be designed to provide close to natural stiffness to the prosthetic ankle system. This will ensure that when the prosthetic ankle system is used by a user, the prosthetic ankle system will provide the correct amount of reaction force propelling the user forward. Additionally, if the user reports an uncomfortable roll-over characteristic, a rubber compliant element can be added in series such that the system can approximate a natural ankle more closely.

The sensor systems used are rather well-designed, as the information that could be received covers the needs of the system. However, some functionality was not used in the IMU, such as a wake-up signal and step detection. This could however be utilised to take the MCU out of sleep mode to save battery power. The rotary encoder is also a relative rotary encoder and means that the ankle system must find a reference position upon startup. Using an absolute encoder, the position will be remembered even when power is removed. However, once again, this comes at the cost of a higher overall system cost.

The motor topology creates an interesting problem where a small control signal does not allow the motor to have enough torque to move smoothly, as can be seen in Figure 5.18. Using a stepper motor or brushless DC motor, allows the motor to have full load torque at a small control signal. This is due to the difference in driving methodology of driving a brushed DC motor and a brushless DC motor or stepper motor, as a bushed DC motor driver changes the average voltage over the motor, while the other motor driver systems control the frequency of the voltage waveforms to the motor. This allows the motor to have full load torque at all control signals and will, therefore, improve the PID ramp response seen in Figure 5.18. However, stepper motors are quite heavy and typically slower than brushless DC motors. Brushless DC motors are made in a similar weight and form factor as the chosen motor, which means it can be mechanically substituted quite easily. However, using a brushless DC motor does require a more involved motor driver system that will need to be designed if the overall system size should be kept small.

The motor driver system does perform as expected under load and allows for fine control of the motor, meaning the motor driver system is adequate for this solution. However, if a different motor topology were chosen a different motor driver system would be required to drive the motor. Additionally, the minimum battery capacity required for the ankle system can be assuming the ankle system to be a constant load of 10 W, with an on time duty cycle of 0.4, as the motor is only active during the swing phase and multiplying by 8 hours. Which provides an estimate of 24 Wh, which will be sufficient to drive the motor system for 8 hours of continuous walking. A battery pack can be constructed using smaller form factor battery cells and arranging them around the chassis to decrease the form factor of the overall system, using an integrated battery management system to allow for ease of use.

The strain gauges that were mounted on the carbon blades may need to be moved to a more rigid load-bearing mounting position. This is due to the fact that the carbon blades will need to be upgraded, and the wiring may become damaged if the carbon blades are fitted into a silicone covering. If the strain gauges were moved to a more rigid mounting position, an analogue amplification stage will be needed before the strain gauges are measured with the 24-bit ADC. The strain gauge readings are summed together to give the reaction force on the prosthetic foot. If a single Wheatstone bridge were used to measure the strain on a rigid mounting position, the system complexity would be reduced. However, the system was found to function sufficiently well to meet the deliverables. Therefore, further development of the reaction force measurement would only serve to increase the practicality and simplicity of the system.

Bibliography

[1] B. Tech, "Salaries in South Africa – half of all workers earn less than you think."

[2] K. Devinuwara, A. Dworak-Kula, and R. J. O'Connor, "Rehabilitation and prosthetics post-amputation," *Orthopaedics and Trauma*, vol. 32, pp. 234–240, Aug. 2018.

[3] L. Ennion and S. Manig, "Experiences of lower limb prosthetic users in a rural setting in the Mpumalanga Province, South Africa," *Prosthetics and Orthotics International*, vol. 43, pp. 170–179, Apr. 2019.

[4] E. M. Balk, A. Gazula, G. Markozannes, H. J. Kimmel, I. J. Saldanha, L. J. Resnik, and T. A. Trikalinos, "Table 1, Lower limb extremity prosthesis Medicare Functional Classification Levels (K levels)." https://www.ncbi.nlm.nih.gov/books/NBK531517/table/ch2.tab1/, Sept. 2018.

[5] S. Farrokhi, B. Mazzone, S. Eskridge, K. Shannon, and O. T. Hill, "Incidence of Overuse Musculoskeletal Injuries in Military Service Members With Traumatic Lower Limb Amputation," *Archives of Physical Medicine and Rehabilitation*, vol. 99, pp. 348–354.e1, Feb. 2018.

[6] V. J. Harandi, D. C. Ackland, R. Haddara, L. E. C. Lizama, M. Graf, M. P. Galea, and P. V. S. Lee, "Gait compensatory mechanisms in unilateral transfemoral amputees," *Medical Engineering & Physics*, vol. 77, pp. 95–106, Mar. 2020.

[7] A. H. Al-dabbagh and R. Ronsse, "A review of terrain detection systems for applications in locomotion assistance," *Robotics and Autonomous Systems*, vol. 133, p. 103628, Nov. 2020.

[8] J. Kim, M. J. Major, B. Hafner, and A. Sawers, "Frequency and Circumstances of Falls Reported by Ambulatory Unilateral Lower Limb Prosthesis Users: A Secondary Analysis," *PM&R*, vol. 11, no. 4, pp. 344–353, 2019.

[9] O. Chiriac and D. Bucur, "From Conventional Prosthetic Feet to Bionic Feet. A Review," pp. 130–138, July 2020.

[10] R. Di Gregorio and L. Vocenas, "Identification of Gait-Cycle Phases for Prosthesis Control," *Biomimetics*, vol. 6, p. 22, Mar. 2021.

[11] T. Stöckel, R. Jacksteit, M. Behrens, R. Skripitz, R. Bader, and A. Mau-Moeller, "The mental representation of the human gait in young and older adults," *Frontiers in Psychology*, vol. 6, July 2015.

[12] C. L. Brockett and G. J. Chapman, "Biomechanics of the ankle," *Orthopaedics and Trauma*, vol. 30, pp. 232–238, June 2016.

[13] K. Embry, "The Effect of Walking Incline and Speed on Human Leg Kinematics, Kinetics, and EMG," Oct. 2018.

[14] H. Lee, E. J. Rouse, and H. I. Krebs, "Summary of Human Ankle Mechanical Impedance During Walking," *IEEE Journal of Translational Engineering in Health and Medicine*, vol. 4, pp. 1–7, 2016.

[15] H.-C. Chen, J. A. Ashton-Miller, N. B. Alexander, and A. B. Schultz, "Stepping Over Obstacles: Gait Patterns of Healthy Young and Old Adults," *Journal of Gerontology*, vol. 46, pp. M196–M203, Nov. 1991.

[16] M. Riveras, E. Ravera, D. Ewins, A. F. Shaheen, and P. Catalfamo-Formento, "Minimum toe clearance and tripping probability in people with unilateral transtibial amputation walking on ramps with different prosthetic designs," *Gait & Posture*, vol. 81, pp. 41–48, Sept. 2020.

[17] R. C. Sheehan and J. S. Gottschall, "At similar angles, slope walking has a greater fall risk than stair walking," *Applied Ergonomics*, vol. 43, pp. 473–478, May 2012.

[18] D. H. Gates, J. B. Dingwell, S. J. Scott, E. H. Sinitski, and J. M. Wilken, "Gait characteristics of individuals with transtibial amputations walking on a destabilizing rock surface," *Gait & Posture*, vol. 36, pp. 33–39, May 2012.

[19] A. K. Silverman, N. P. Fey, A. Portillo, J. G. Walden, G. Bosker, and R. R. Neptune, "Compensatory mechanisms in below-knee amputee gait in response to increasing steady-state walking speeds," *Gait & Posture*, vol. 28, pp. 602–609, Nov. 2008.

[20] D. C. De Coeyer, Dylan and A. Legrand, *Adaptive Control of an Active Ankle Prosthesis*. PhD thesis, Université catholique de Louvain, 2020.

[21] M. Windrich, M. Grimmer, O. Christ, S. Rinderknecht, and P. Beckerle, "Active lower limb prosthetics: A systematic review of design issues and solutions," *BioMedical Engineering OnLine*, vol. 15, p. 140, Dec. 2016.

[22] J. F. Lehmann, R. Price, S. Boswell-Bessette, A. Dralle, K. Questad, and B. J. deLateur, "Comprehensive analysis of energy storing prosthetic feet: Flex Foot and Seattle Foot Versus Standard SACH foot," *Archives of Physical Medicine and Rehabilitation*, vol. 74, pp. 1225–1231, Nov. 1993.

[23] A. Naseri, M. Mohammadi Moghaddam, M. Gharini, and M. Ahmad Sharbafi, “A Novel Adjustable Damper Design for a Hybrid Passive Ankle Prosthesis,” *Actuators*, vol. 9, p. 74, Sept. 2020.

[24] A. K. Lapre, “Semi-Active Damping for an Intelligent Adaptive Ankle Prosthesis,” 2012.

[25] E. M. Glanzer and P. G. Adamczyk, “Design and Validation of a Semi-Active Variable Stiffness Foot Prosthesis,” *IEEE Transactions on Neural Systems and Rehabilitation Engineering*, vol. 26, pp. 2351–2359, Dec. 2018.

[26] G. A. Caprini, C. M. Cunha, A. G. L. Junior, and R. M. Andrade, “Designing an Active Ankle-Foot Prosthesis: Digital Prototype, Modeling and Control,” in *2022 IEEE International Conference on Automation/XXV Congress of the Chilean Association of Automatic Control (ICA-ACCA)*, pp. 1–4, Oct. 2022.

[27] C. Everarts, B. Dehez, and R. Ronsse, “Variable Stiffness Actuator applied to an active ankle prosthesis: Principle, energy-efficiency, and control,” in *2012 IEEE/RSJ International Conference on Intelligent Robots and Systems*, (Vilamoura-Algarve, Portugal), pp. 323–328, IEEE, Oct. 2012.

[28] B. Convens, D. Dong, R. Furnemont, T. Verstraten, P. Cherelle, D. Lefeber, and B. Vanderborght, “Modeling, Design and Test-Bench Validation of a Semi-Active Propulsive Ankle Prosthesis With a Clutched Series Elastic Actuator,” *IEEE Robotics and Automation Letters*, vol. 4, pp. 1823–1830, Apr. 2019.

[29] D. Dong, W. Ge, B. Convens, Y. Sun, T. Verstraten, and B. Vanderborght, “Design, Optimization and Energetic Evaluation of an Efficient Fully Powered Ankle-Foot Prosthesis With a Series Elastic Actuator,” *IEEE Access*, vol. 8, pp. 61491–61503, 2020.

[30] S. Au, P. Dilworth, and H. Herr, “An ankle-foot emulation system for the study of human walking biomechanics,” in *Proceedings 2006 IEEE International Conference on Robotics and Automation, 2006. ICRA 2006.*, pp. 2939–2945, May 2006.

[31] S. Au, M. Berniker, and H. Herr, “Powered ankle-foot prosthesis to assist level-ground and stair-descent gaits.” https://reader.elsevier.com/reader/sd/pii/S0893608008000683?token=B7E12118858D0B53D03D944964B91EE4F995750679B94D4C611DFCB3B8512196573D28D266BFA55E77B35378ABD0F473&originRegion=eu-west-1&originCreation=20230227060424.

[32] M. Chang, K. Kim, and D. Jeon, “Research on Terrain Identification of the Smart Prosthetic Ankle by Fuzzy Logic,” *IEEE Transactions on Neural Systems and Rehabilitation Engineering*, vol. 27, pp. 1801–1809, Sept. 2019.

[33] T. Lenzi, M. Cempini, L. J. Hargrove, and T. A. Kuiken, "Design, Development, and Validation of a Lightweight Nonbackdrivable Robotic Ankle Prosthesis," *IEEE/ASME Transactions on Mechatronics*, vol. 24, pp. 471–482, Apr. 2019.

[34] T. Lenzi, M. Cempini, J. Newkirk, L. J. Hargrove, and T. A. Kuiken, "A lightweight robotic ankle prosthesis with non-backdrivable cam-based transmission," in *2017 International Conference on Rehabilitation Robotics (ICORR)*, pp. 1142–1147, July 2017.

[35] N. J. Rosenblatt, A. Bauer, CPO, D. Rotter, CPO, and M. D. Grabiner, "Active dorsiflexing prostheses may reduce trip-related fall risk in people with transtibial amputation," *Journal of Rehabilitation Research and Development*, vol. 51, no. 8, pp. 1229–1242, 2014.

[36] L. Fradet, M. Alimusaj, F. Braatz, and S. I. Wolf, "Biomechanical analysis of ramp ambulation of transtibial amputees with an adaptive ankle foot system," *Gait & Posture*, vol. 32, pp. 191–198, June 2010.

[37] S. I. Wolf, M. Alimusaj, L. Fradet, J. Siegel, and F. Braatz, "Pressure characteristics at the stump/socket interface in transtibial amputees using an adaptive prosthetic foot," *Clinical Biomechanics*, vol. 24, pp. 860–865, Dec. 2009.

[38] W. Williams, "Bionic Foot Price List," Oct. 2020.

[39] Össur, "All Products | Prosthetic Products | Össur South Africa." https://www.ossur.com/en-za/prosthetics/products.

[40] D. Jin, J. Yang, R. Zhang, R. Wang, and J. Zhang, "Terrain identification for prosthetic knees based on electromyographic signal features," *Tsinghua Science and Technology*, vol. 11, pp. 74–79, Feb. 2006.

[41] B. Chen, E. Zheng, X. Fan, T. Liang, Q. Wang, K. Wei, and L. Wang, "Locomotion Mode Classification Using a Wearable Capacitive Sensing System," *IEEE Transactions on Neural Systems and Rehabilitation Engineering*, vol. 21, pp. 744–755, Sept. 2013.

[42] R. Kala, "Chapter 1 - An introduction to robotics," in *Autonomous Mobile Robots* (R. Kala, ed.), Emerging Methodologies and Applications in Modelling, pp. 1–48, Academic Press, Jan. 2024.

[43] K. Yuan, Q. Wang, and L. Wang, "Fuzzy-Logic-Based Terrain Identification with Multisensor Fusion for Transtibial Amputees," *IEEE/ASME Transactions on Mechatronics*, vol. 20, pp. 618–630, Apr. 2015.

[44] M. Hebert, "Active and passive range sensing for robotics," in *Proceedings 2000 ICRA. Millennium Conference. IEEE International Conference on Robotics and Au-*

tomation. Symposia Proceedings (Cat. No.00CH37065), vol. 1, (San Francisco, CA, USA), pp. 102–110, IEEE, 2000.

[45] B. Langmann, K. Hartmann, and O. Loffeld, "DEPTH CAMERA TECHNOLOGY COMPARISON AND PERFORMANCE EVALUATION:," in *Proceedings of the 1st International Conference on Pattern Recognition Applications and Methods*, (Vilamoura, Algarve, Portugal), pp. 438–444, SciTePress - Science and and Technology Publications, 2012.

[46] M. R. Tucker, J. Olivier, A. Pagel, H. Bleuler, M. Bouri, O. Lambercy, J. d. R. Millán, R. Riener, H. Vallery, and R. Gassert, "Control strategies for active lower extremity prosthetics and orthotics: A review," *Journal of NeuroEngineering and Rehabilitation*, vol. 12, p. 1, Jan. 2015.

[47] L. Gabert, S. Hood, M. Tran, M. Cempini, and T. Lenzi, "A Compact, Lightweight Robotic Ankle-Foot Prosthesis: Featuring a Powered Polycentric Design," *IEEE Robotics & Automation Magazine*, vol. 27, pp. 87–102, Mar. 2020.

[48] R. G. Budynas and J. K. Nisbett, *Shigley's Mechanical Engineering Design*. McGraw-Hill Series in Mechanical Engineering, New York, NY: McGraw-Hill, 9. ed ed., 2011.

[49] M. H. Rashid, *Power Electronics Devices, Circuits, and Applications*. Peason Education, 2014.

Appendix A

The prosthetic ankle was tested using a custom designed test bench that emulates human walking biomechanics. This is achieved using a stepper motor to emulate the human hip and a treadmill to simulate a surface being traversed. The height of the hip motor can be adjusted using a linear actuator, however, the hip motor is kept at a specific height during the duration of the test.

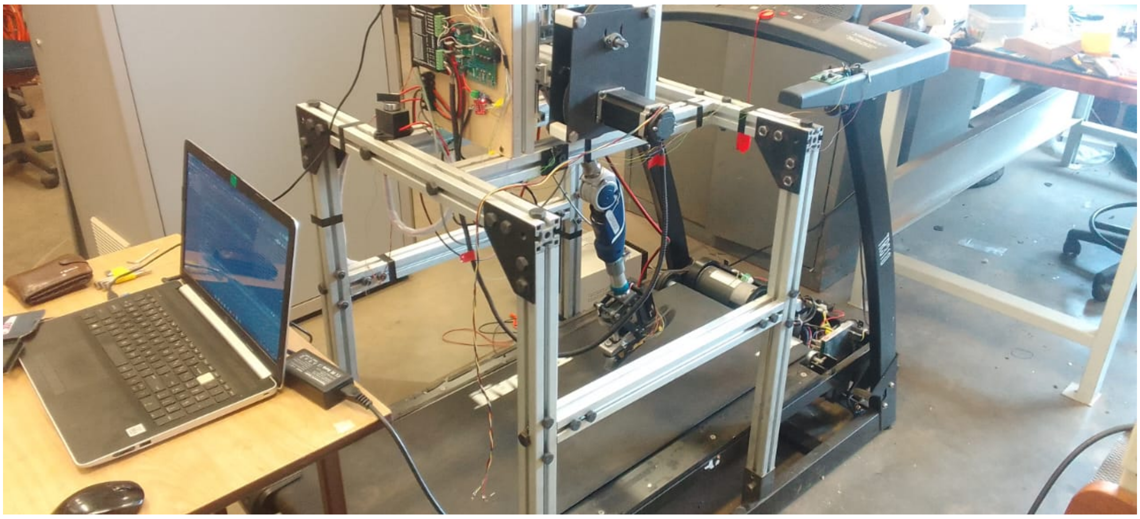

Figure 1: Test bench with prosthetic ankle

The test bench is operated by sending data from a computer to the test bench through a serial communication. Then the test bench sets up internal parameters, such as the hip height and treadmill speed. Once a start command is received, the test bench can begin simulating the human gait cycle for a specified number of steps. The test bench was designed in collaboration with Mr. JS Malan in order to avoid ethical conundrums with testing the prosthetics on a human amputee.